

Hybrid Light-Emitting Diode Enhanced With Emissive Nanocrystals

A dissertation

Submitted to the Department of Photonics Engineering
at the Technical University of Denmark in partial fulfillment
for the degree of Doctor of Philosophy

Oleksii Kopylov

August 2013

0. <Contents

Contents

Contents	3
Acknowledgments.....	7
Publications.....	9
Abstract.....	11
Resumé.....	13
1. Introduction	15
2. Theoretical background.....	19
2.1 Types of lighting. History of LEDs.....	19
2.2 White LEDs based on InGaN/GaN blue LEDs.....	23
2.3 Hybrid white LEDs	27
2.4 Non-radiative resonant energy transfer	29
2.4. Colloidal semiconductor quantum dots	32
2.5. Quality of the white light, CRI index and CCT.....	35
3. Processing in the clean room.....	39
3.1 Process overview.....	39
3.2 GaN/InGaN etching.....	46
3.2.1 Reactive Ion Etching (RIE).....	47
3.2.2 Inductively coupled plasma (ICP) RIE	59
3.2.3 Ion Beam Etching (IBE)	63

0. <Contents

3.2.4	Post-etching treatment	64
3.2.5	Conclusions.....	66
3.3	Contacts to GaN	67
3.3.1	n-type contact.....	67
3.3.2	p-type contact.....	70
3.3.3	Transmission line measurements	72
3.3.4	Conclusions.....	77
3.4	Conclusions	77
4.	Characterization techniques	79
4.1	Photoluminescence measurements.....	79
4.1.1	PL measurements in the lab	79
4.1.2	PL-mapper.....	82
4.1.3	Micro-PL.....	83
4.2	Time-resolved PL	85
4.2.1	TRPL data analysis	88
4.3	Current-voltage measurements.....	90
4.4	Electroluminescence measurements.....	93
4.5	Conclusions	96
5.	Thin cap LEDs	97
5.1	Device structure.....	98
5.2	Effect of the capping layer thickness	103

5.2.1	Emission wavelength dependence on the cap thickness	104
5.2.2	Effect of the cap thickness on the carrier localization	109
5.2.3	Change of carrier dynamics with decrease of the cap thickness	114
5.3	Effect of nanocrystals and influence of ligands	121
5.4	Electrical characterization of the diodes	124
5.5	Conclusions	126
6.	Patterned LEDs.	129
6.1	Device structure and fabrication	130
6.2	White LED characterization.....	135
6.3	Non-radiative energy transfer in patterned devices....	140
6.3.1	Influence of RET on dynamics of carriers in the QW	141
6.3.2	Influence of RET on the dynamics of carriers in the nanocrystals	147
6.4	Conclusions	154
7.	Conclusions and outlook	156
	Appendix A. Patterned LED fabrication procedure.....	160
	Appendix B. Etching recipes for RIE Plassys and III-V ICP placed in the Danchip clean room for III-Nitrides etch.....	167

0. <Contents

Appendix C. Simulations of the effect of GaN capping thickness on recombination of electron-hole pairs in high indium-content InGaN quantum wells.	169
Abbreviations	174
Bibliography.....	176

Acknowledgments

This PhD work was supported by the project grant from Danish Research Council for Technology and Production Sciences.

I would like to first of all thank my supervisors, Beata Kardynal and Kresten Yvind. Beata for giving me opportunity to start PhD in her group and for a great help and support during my PhD at DTU Fotonik. She is a great motivator and it is so pleasant to work with her. Beata has shared her wide and deep knowledge with me, I appreciate that. Kresten for a taking me as his PhD student after Beata Kardynal had to move to another Institute and for always being very helpful especially regarding my questions and problems in the clean room (even before becoming my main supervisor).

I would like to thank Olli Svensk and Markku Sopanen from Aalto University, Finland for supplying a thin cap InGaN/GaN single quantum well samples used in the experiments.

Morten Willatzen and Benny Lassen for the simulations of the thin cap samples.

Alex Huck for a great help with micro-PL measurements performed on his setup and fruitful discussions of obtained results.

Shima Kadkhodazadeh for TEM analysis of the sample.

Henri Nielsen for sharing his expertise about an optical setup.

Sergei Zhukovsky for fruitful discussions and help with proof reading of the thesis.

Roza Shirazi and Claudia Gritti for support.

Thor Ansbaek for being great officemate and for his advices and suggestions regarding the clean room processing.

0. Acknowledgments

Irina Kulkova, Nadezda Kuznetsova, Elizaveta Semenova, Luisa Ottaviano, Anton Dogadaev, Maksim Zalkovskij, Radu Malureanu, Andrei Lavrinenko, and Andrei Andrievski for making DTU Fotonik friendly place of work.

Rest of the Nanodevices group members that I didn't mention so far: Minhao, Aleksandra, Lars, Asger, Yunhong.

Other people at DTU Fotonik that I forgot to mention for making a great working atmosphere at Fotonik.

To my family, who supported me during the PhD. Especially to my wife Olena and daughter Aleksandra for their patience and understanding when they had to spend evenings and nights without their husband and father. I hope that when Aleksandra grows up, she will read this thesis and understand why her father spent so much time at work rather than with her.

Publications

During my PhD following publications with me as author or co-author were prepared:

Journal publications:

1. Kopylov O.; Shirazi R.; Svensk, O.; Suihkonen, S.; Sintonen, S.; Sopanen, M.; Kardynal B.: **Effect of GaN cap thickness on carrier dynamics in InGaN quantum wells.** *Phys. Stat. Solidi. C* 2012, **9**: 727-729.
2. Svensk, O.; Suihkonen, S.; Sintonen, S. ; Kopylov, Oleksii; Shirazi, Roza; Lipsanen, H.; Sopanen, M.; Kardynal, Beata: **MOCVD growth and characterization of near-surface InGaN/GaN single quantum wells for non-radiative coupling of optical excitations.** *Phys. Stat. Solidi. C* 2012, **9**: 1667-1669.
3. R. Shirazi, O. Kopylov, A. Kovács, B. Kardynal: **Temperature dependent recombination dynamics in InP/ZnS colloidal nanocrystals.** *Appl. Phys. Lett.* 2012, **9**: 091910.
4. Daisuke Iida, Yuntian Chen, Yiyu Ou, Ahmed Fadil, Oleksii Kopylov, Motoaki Iwaya, Tetsuya Takeuchi, Satoshi Kamiyama, Isamu Akasaki, and Haiyan Ou: **Enhanced internal quantum efficiency of surface plasmon-based green emission GaInN/GaN multiple quantum wells.** Submitted to *Optics Express*.
5. Oleksii Kopylov, Benny Lassen, Morten Willatzen, Kresten Yvind, and Beata Kardynal: **Interplay of localization and surface states in near-surface InGaN quantum wells.** Submitted to *Nanoscale Research Letters*.
6. Oleksii Kopylov, Alexander Huck, Shima Kadkhodazadeh, Kresten Yvind, and Beata Kardynal: **Resonant energy transfer in hybrid devices in the presence of surface recombination.** To be submitted.

0. Publications

Conference proceedings:

1. Kopylov, Oleksii; Huck, Alexander; Shirazi, Roza; Yvind, Kresten; Kardynal, Beata: **Design and geometry of hybrid white light-emitted diodes for efficient energy transfer from the quantum well to the nanocrystals.** *Progress in Biomedical Optics and Imaging* 2013, **8625**: 862524. Presented at: SPIE Photonics West: Green Photonics, San Francisco, CA, February 2013.
2. O. Kopylov, R. Shirazi, K. Yvind, and B. E. Kardynal: **Exciton dynamics in near-surface InGaN quantum wells coupled to colloidal nanocrystals.** Accepted for the IEEE Photonics Conference 2013 to be held on 8-12 September, in Hyatt Regency Bellevue, Bellevue Washington, USA.

Journal publications obtained within PhD term but not corresponding to this PhD thesis:

1. Kopylov, Oleksii; Lee, Jungil; Han, Ilki; Choi, Won Jun; Song, Jin Dong; Yeo, Ina: **Temperature Dependence of the Excitonic Energy Band-gap in In(Ga)As Nanostructures.** *Korean Phys. Soc. Journal* 2012, **10**: 1828-1832.
2. Abdellatif, M. H.; Kopylov, Oleksii; Song, Jin Dong; Choi, Won Jun; Cho, Nam Ki; Lee, Jungil: **Applicability of Steady State Model to Carrier Thermodynamics in InAs Quantum Dot.** *Journal of Nanoscience and Nanotechnology* 2011, **11**: 606-609.

Abstract

This thesis investigates a new type of white light emitting hybrid diode, composed of a light emitting GaN/InGaN LED and a layer of semiconductor nanocrystals for color conversion. Unlike standard white LEDs, the device is configured to achieve high color conversion efficiency via non-radiative energy transfer from the primary LED to the nanocrystals.

LED structures with sub-10 nm separation the between quantum well and the surface and patterned standard bright LEDs are considered for the hybrid devices, which require close proximity of the nanocrystals to the quantum well. The development of the hybrid diode fabrication including process techniques for GaN LED and incorporation of the nanocrystals are presented with the emphasis on the differences with standard LED processing.

Results and analysis of optical and electrical characterization including photoluminescence (PL), micro-PL, time-resolved PL and electroluminescence (EL) together with current-voltage characteristics are presented to evaluate the device performance. A clear evidence of non-radiative energy transfer was seen in the carrier dynamics of both the LED and the nanocrystals when the quantum well – nanocrystals separation was less than 10nm. Analysis of the results shows that in order to achieve sufficient for the white LED color conversion, better surface passivation and nanocrystals with shorter exciton lifetimes and weaker Auger recombination and needed.

0.

Resumé

Denne afhandling præsenterer undersøgelser af en ny type hvid lys emitterende diode (LED), bestående af en GaN/InGaN LED og et lag med halvleder nanokrystaller til farvekonvertering. Modsat normale hvide LED er komponenterne lavet til at opnå en effektiv farvekonvertering ved hjælp af ikke-radiativ energioverførsel mellem den primære LED lyskilde og nanokrystallerne.

LED strukturer med sub-10nm afstand mellem kvantebrønde og overfladen og ”hullede” standard LEDer er undersøgt for anvendelse i hybride komponenter, som kræver kort afstand mellem nanokrystallerne og kvantebrønden. Udviklingen af fabrikationsprocedurer for de undersøgte hybride komponenter, herunder processtrin for GaN og indlejring af nanokrystaller præsenteres i afhandlingen, med fokus på forskellene fra standard LED fremstilling.

Resultater og analyse af optisk og elektrisk karakterisering herunder fotoluminescens (PL), mikro-PL, tidsopløst PL og elektroluminescens (EL) sammen med strøm-spændings karakteristikker er udført for at undersøge komponentegenskaberne. Stærkt bevis for ikke-radiativ energioverførsel blev fundet i ladningsbærer-dynamikken af både LED og nanokrystaller når afstanden mellem kvantebrønd og nanokrystallerne var mindre end 10nm. Analyse af resultaterne viser, at for at opnå tilstrækkelig effektivitet for farvekonvertering til at opnå hvidt lys, skal en bedre overfladepassivering og nanokrystaller med kortere eksitonlevetid og svagere Auger rekombination anvendes.

0. Résumé

1. Introduction

A striking progress within the field of light-emitting diodes (LEDs) has been achieved during the past several decades. LEDs became powerful and at the same time energy efficient, with a variety of different emission wavelengths from UV and violet [1], [2] (AlGaIn and InGaIn based) to deep red [3], [4], [5] (based on GaP and its ternaries) single wavelength diodes, as well as multicolor and white LEDs [6], [7]. This technology has developed into solid-state lighting (SSL), displacing other light sources over time and therefore attracting huge attention from the customers and producers. The producers were willing to improve quality of white LEDs and cut its fabrication costs using new technologies, in order to make LEDs more attractive for the customers.

Even though white LEDs are widely used now, both their high price and slightly worse color rendering compared to the conventional bulbs push technology to invent and fabricate better and cheaper devices by discovering new ways, solutions and materials. Most of currently available white LEDs are built on InGaIn/GaIn with adding color conversion materials such as phosphors [7], [8], allowing to mix violet-blue color from InGaIn and yellow color from phosphor. InGaIn is very important for such applications; it is indeed the only material available today for short wavelength emission in the visible light spectrum, but phosphor as the color conversion material can and should be optimized. White LEDs built on a stack of epitaxially grown InGaIn quantum wells (QWs) of different indium concentration covering blue, green and yellow parts of the light spectrum [9], and hybrid devices with

1. Introduction

nanocrystals (NCs) [10] or polymers [11] as color conversion material have been reported.

This thesis has been accomplished within the project “Hybrid Light-emitting Diode Enhanced with Emissive Nanocrystals”. The main idea of the project is to investigate a new type of white hybrid LED, which relies on the incorporation of non-radiative energy transfer from the emissive layer of a semiconductor LED to a layer of highly emissive nanocrystals in order to obtain broad-spectrum emission and high emission efficiency, to compare such devices with existing technologies, and to identify key issues for further development. The first (theoretical) proposal for hybrid devices was put forward by Agranovich et al. [12], who calculated the probability of non-radiative resonant energy transfer (RET) from excitons (or electron-hole pairs) in inorganic quantum wells (the emissive layers of LEDs) to excitons in organic materials. The results suggested that this process should be very efficient, provided that the distance between the two emissive layers was of the order of 10 nm or less. New technological advances have confirmed Agranovich's predictions in hybrid devices, where the exciton transfer takes place from quantum wells of gallium nitride (GaN) based heterostructures either to organic materials [13] or to inorganic nanocrystals [14], [15]. Most previous experimental work used laser illumination to create excitons in the quantum well [13], [14] because of the challenge of establishing electrical contacts to devices with a thin doped layer between the quantum well and the surface which is necessary for RET [10]. All of these experiments agreed that RET is much more efficient than emission–absorption process. However, it is hard to measure the actual efficiency of RET due to the use of optical pumping of the device.

1. Introduction

Therefore, the main task of the project is to fabricate white LED, starting from the blue InGaN LED, establishing a full processing in the clean room. Next task is to choose the NCs and set up their correct deposition on top of the wafer followed by full device fabrication and characterization. Hence, the project was mainly experimental, involving both fabrication of the devices in the clean room and optical and electrical characterizations of fabricated devices. Additional modeling and calculations were also needed to be carried out. A lot of effort was required in order to achieve good results in device fabrication and processes optimization since fabrication of III-V nitrides had not been established in the Danchip clean room before.

The thesis is split into 7 chapters including introduction and conclusions but excluding appendices. Chapter 2 contains background information, covering theoretical details regarding LEDs, their types and principles of operation. The processing flow and development is explained in chapter 3, including a detailed look into some processes such as etching of InGaN material, or forming ohmic contacts to the device. Chapter 4 is focused on measurement techniques used in this work. Chapter 5 summarizes the work on the thin cap devices, their possible applications, advantages and drawbacks. The discussion is focused on thin cap devices as a platform for white LEDs with nanocrystals deposited on the surface as a color conversion layer. Chapter 6 describes the second type of hybrid white LED structure – a patterned device. A clear evidence of RET is observed, disadvantages of such design are also discussed. In the Chapter 7 final results are concluded and an outlook for further work is enclosed. The Appendices contain information about details of processing. Full fabrication process is presented in Appendix A and recipes for dry etching are shown in Appendix B. Theoretical simulations of an effect of thin GaN cap layer

1. Introduction

samples on recombination of electron-hole pairs in high indium content QW are presented in Appendix C.

A list of used abbreviations and the bibliography can be found after the appendices.

2. Theoretical background

This chapter introduces the concept of the solid state lighting (SSL) and a current status of a white LED (WLED) development, explaining why SSL should be further developed. Presented is a short history of LEDs, their current performance and materials used for their fabrication. Sections describing hybrid LED based on a non-radiative resonant energy transfer (RET) from the QWs to the colloidal quantum dots (QDs), also called nanocrystals (NCs), as well as their characteristics are included. The last section is devoted to the white light, its quality and color temperature.

2.1 Types of lighting. History of LEDs.

The mankind has always needed lighting. Incandescence, fluorescence and solid-state lighting (SSL) based on light-emitting diodes (LEDs) (Figure 2.1) are the three main electrically driven lighting devices being used in our life.

2. Theoretical background




Incandescent	Fluorescent	LED
		
1.500-2.000 hours	10.000-20.000 hours	100.000 hours (up to 300.000 hours was informed)

Figure 2.1. Main electrically driven lighting options.

Incandescent lamp was invented in XIX century and with time it became the most popular light source. Here electricity was acting as a fuel to heat a metal wire with further emission of broadband blackbody light. Incandescent bulbs are not very efficient due to their very broadband emission: about 95% of energy supplied to the lamp is wasted for heating. However, the incandescent light is the closest to the sun light spectrum among all artificial lights so far, as the highest temperature of the light is of the order of 2000 K. Another technology, fluorescence light sources, uses the electricity as a fuel to excite (but not heat) a low-pressure gas with further narrowband atomic-line emission. Light can be emitted either directly from the electrical injection or indirectly, by absorption in fluorescent materials and re-emitted at longer wavelengths. Due to its narrowband emission concentrated in the visible part of the spectrum, the efficiency of such lamps is much higher than for usual incandescent bulbs. The drawbacks of this technology are: visual flickering, long startup time, and use of mercury and other ecologically unfriendly materials. Moreover, the color rendering is quite

2. Theoretical background

limited because of the narrowband emission, which also restricts application areas.

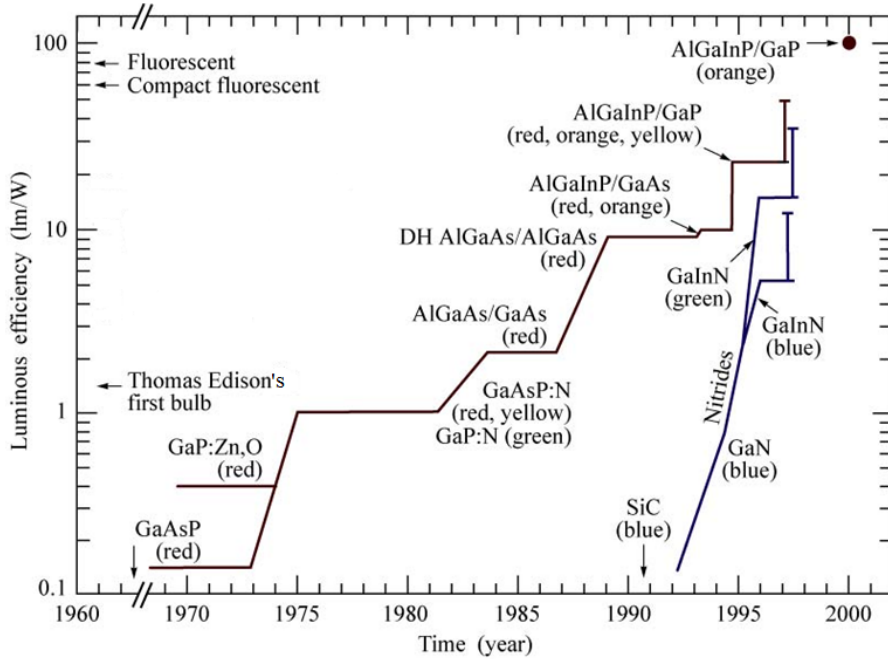


Figure 2.2. Timeline of development of luminous efficiency of visible-spectrum LEDs and other light sources (from [17])

The last and the newest technology is SSL based on inorganic or organic LEDs (OLEDs). In LEDs, electricity is used to inject electrons and holes into the active semiconductor material. Due to radiative recombination, light is emitted in a narrow band, allowing higher efficiencies compared to conventional bulbs. However, narrow-band emission does not lead to a good color rendering of the light source. The history of diodes starts from 1907, when the very first device was accidentally fabricated from SiC by Henry Round and immediately reported to the journal “Electrical World” [16]. Not much work has been done until 1960th, but since then the LED technology arose with full power. Research efforts started to bring good results and involved more

2. Theoretical background

and more materials, starting from GaAsP, GaP, GaAs, AlGaAs, and then moving to InGaN, GaInP based LEDs (Figure 2.2).

The light industry has rapidly developed after this huge jump occurred about half a century ago. LED technology came to the market but is still being developed to improve quality of devices. LED devices are very small, bright and efficient, environmentally friendly, and are becoming cheaper and cheaper. A lot of effort is still directed into improving the light quality and efficiency as well as lowering the price of diodes. Wide band-gap III-N semiconductors such as GaN, InN, AlN, as well as their ternary and quaternary alloys, have proven to be of the best choice for optoelectronic devices working in UV and blue range and have a potential to reach IR range. The main feature of III-V nitrides is their use as blue LEDs, and it explains why they became such interesting and desirable materials. Good quality WLEDs are impossible without blue part of spectrum. Moreover, III-V nitrides differ from other semiconductors by their stronger bonding energies and higher chemical and electrical stability, which allows longer lifetime and higher operating temperatures. Nitrides gave rise to highly efficient LEDs of different colors, including white LEDs [6], [7], [8], [18], [19], [20] as well as UV to green lasers [21], [22], [23], [24]. They are now commonly used in various applications - not only in the architecture or as a light source in premises but also as backlights for flat-screen televisions and monitors, and even as Christmas lights. Modern smartphones and tablet computers employ LEDs as back lights, as indicator lights, and as flash lights for cameras. Arrays of LEDs are used in high-power lighting applications such as in car headlights and indicator lights, and many others.

2.2 White LEDs based on InGaN/GaN blue LEDs

Currently about ~30% of all primary energy is used for generation of electricity, and ~20% of all electricity is used for lighting, mostly white lighting. Hence, around one-fifteenth of all energy is used for lighting [25]. If efficiency of lighting was at least doubled compared to the current level, for example by replacing conventional incandescent bulbs with LEDs, it would lead to a 10% decrease of the total energy consumption. It is predicted to be about 1.8 TW-hr/year, or \$120 B/year, by the year 2025. Over 250 GW of electric generating capacity can be applied towards other uses, saving about \$100 B in construction costs. It will also reduce global carbon emissions predicted by year 2025 by about 300 Mtons/year [25]. Therefore, this topic is very important.

Recognition of these figures has triggered the European Union to request the phasing out of inefficient incandescent lamps beginning from September 1st 2009 [26]. The market for energy-efficient lighting is dominated by fluorescent lamps due to their relatively low prices, despite their two primary drawbacks: their use of toxic materials and their physiologically unnatural color spectrum (in comparison with that of black body radiation such as sunlight). In contrast, SSL based on LEDs can approximate almost any desired color spectrum, making it a powerful lighting paradigm [27]. There is also less of a problem when it comes to the energy-efficient lighting disposal because expected their lifetime is very long (targeting 300.000 h) and they do not contain toxic materials. Although SSL is the main reason behind LED research and development, it is only one out of many important applications that would benefit from the availability of cheap, bright LEDs. Other

2. Theoretical background

examples include application in medical and sensing instrumentation, water sanitation for developing countries [27], etc.

The performance of currently available LEDs depends strongly on their emission wavelength [28], which is related to the material that is used to make them. There is a lack of materials with efficient emission in the green color range, where the sensitivity of the eye is the highest (Figure 2.3), limiting the available choices of practical SSL to systems that incorporate phosphor-based color conversion [28]. In such systems the LED light is absorbed by the phosphors which reemit the light in a broad range of wavelengths. While the search for materials that emit in the missing color range continues, new hybrid LEDs are being studied to find ways to provide efficient color conversion.

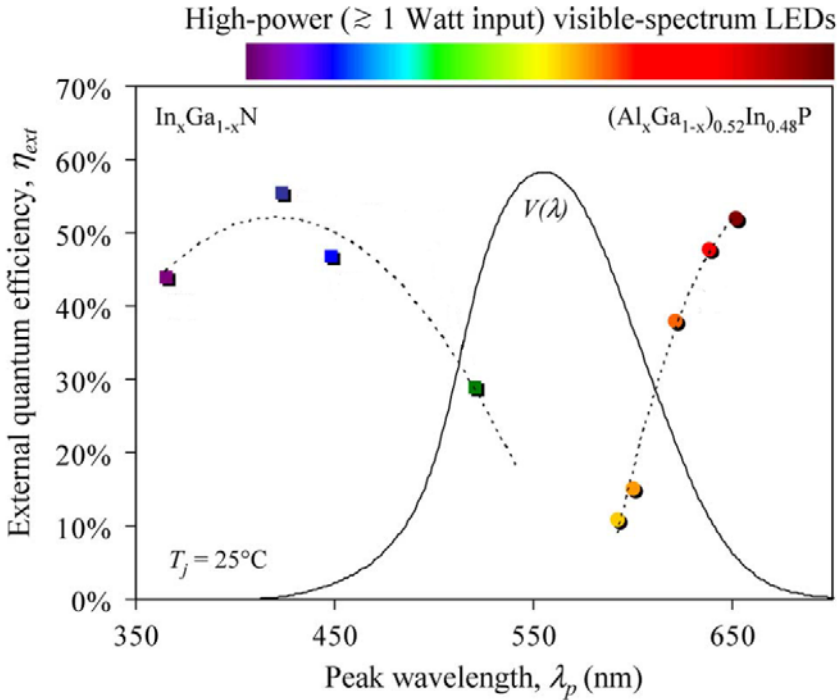


Figure 2.3. External quantum efficiencies for high-power visible-spectrum LEDs, operating at room temperature, assembled in 2007. $V(\lambda)$ is the luminous eye response curve from CIE. Dashed lines are guides to the eye (from [29]).

2. Theoretical background

Two more types of white LEDs currently available on the market are: three individual red-green-blue (RGB) diodes, and stacked QWs. RGB diodes are packed in the same enclosure to produce white light by mixing three colors. Stacked QW WLEDs are based on epitaxially grown QWs emitting at different wavelengths such that due to the mixing of these colors white light is produced.

Each of these above mentioned structures has its own advantages and disadvantages. Devices based on phosphor light-conversion material are the most available and cheapest, therefore most applicable for home use. Commercial white LEDs are mostly constructed from QW diodes with the layer of phosphors as a color converting material on top [7], [8], [30]. Main issues known for phosphor-based white LEDs can be described as follows. There are only a limited number of phosphor materials absorbing light at the blue LED emission wavelength and emitting in full wavelength range, however, we are witnessing a huge development of new phosphor materials with improved efficiency, and discovery of new materials emitting in all green-to-red spectrum range in order to achieve the best possible color rendering of the white LED. The goal is to achieve the emission spectrum composed of the emission of blue LED and phosphors that would lead to a pure white light emission with a specific color rendering and color temperature.

The main advantages of phosphor-based white LEDs are as follows:

- The excitation spectrum of phosphor materials shows rather good overlap with the primary LED and large absorption strength, resulting in good energy efficiency of WLED, however having better absorption in UV spectrum.

2. Theoretical background

- Emission spectrum, excitation spectrum and quantum efficiency that remain unchanged at elevated temperatures (using proper phosphor material).

- The quantum efficiency of the yellow phosphors is approaching unity, thus maximizing the overall electrical-to-optical conversion efficiency of the entire LED-phosphor package, however, conversion efficiencies of other color-emitting phosphors especially the one, responsible for red light generation, are not high enough [31].

- Absence of emission saturation at high fluxes for the phosphor, thus for the WLED.

The efficiency of phosphor converted LEDs expressed in units of lumens per Watt, is better than of the RGB diodes. Color temperature can be tuned with a phosphor composition. Additionally, the blue diode in phosphor-based LEDs is so stable that while the temperature of the die increases the diode doesn't lose much efficiency. In contrast, RGB mixed white LEDs show light color dependence on temperature. The color point is not stable because the red diode used in the chip is very temperature dependent [32]. When the temperature of the die rises, the color point of the whole LED will shift towards cyan and the overall efficacy drops. Another drawback of RGB diodes is a lack of good quality deep-green LED due to the difficulties with growths of high-indium content QWs as well as its low efficiencies.

Stacked LEDs face the same problem. High-quality high efficiency QWs, emitting at different violet-blue, green, and red wavelengths are very difficult to be grown epitaxially due to the high lattice mismatch of the component materials (In,Al,Ga)N (Figure 2.4).

2. Theoretical background

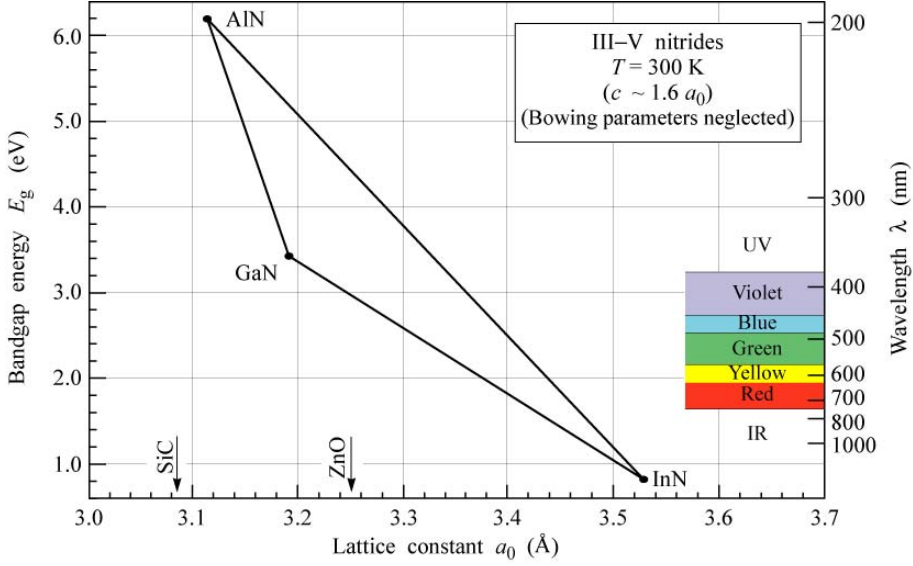


Figure 2.4. Band-gap energy versus lattice constant of III-V nitride semiconductors at room temperature [17].

The final choice for WLEDs fabrication technology has not been made yet, as all three described above WLED (phosphor-based, or stacked, or RGB) have advantages and disadvantages.

Another technology, which is the subject of this thesis, is a hybrid white LED based on InGaN QWs and cheap colloidal NCs deposited in the close proximity to them, where NCs are pumped via non-radiative RET from the QWs. This technology is potentially promising from the point of view of price and efficiency, but needs to be tested and developed.

2.3 Hybrid white LEDs

Hybrid WLEDs are based on both inorganic QWs and organic electronic materials, which are easy and cheap to produce. Organic material emitters such as polymers [33] or colloidal nanocrystals (NCs)

2. Theoretical background

[15], [34] were considered for hybrid LEDs. The white color is achieved by mixing blue emission from InGaN QWs and yellow-orange-red broadband emission from organic materials or semiconductor NCs. Example of the spectrum looks similar to the one from WLED with phosphor and is presented in Figure 2.5. By depositing polymers or NCs emitting in a wide spectrum range good quality of the white light can be obtained.

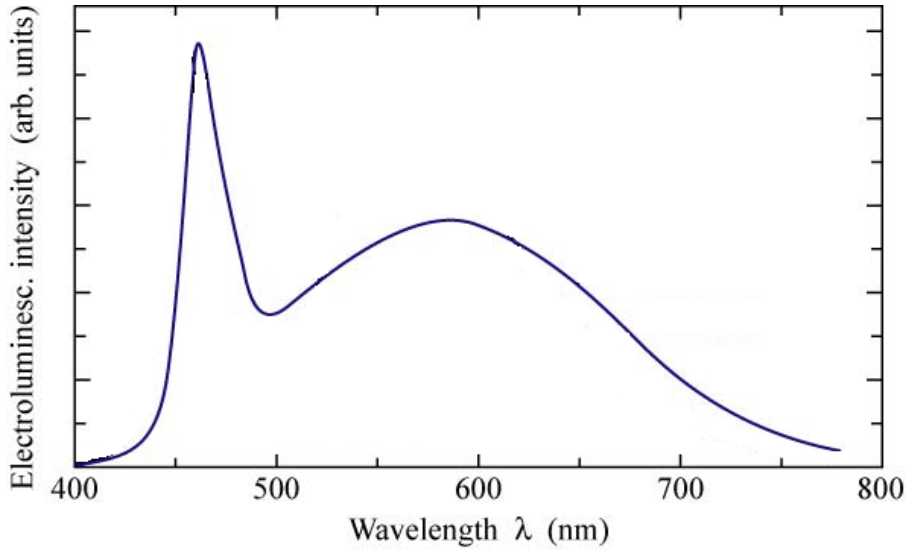


Figure 2.5. Spectrum of the hybrid WLED composed of GaN LED and NCs for color conversion.

The sketch of a hybrid WLED with NCs as an emissive layer is presented in Figure 2.6. The phosphor-based WLEDs employ optical absorption of the blue light from the QW with further re-emission by the phosphor in yellow-red spectrum range, thus the colors of the total light are mixed and white light can be achieved. In contrast to phosphor-based WLEDs in hybrid structures non-radiative resonant energy transfer (RET) is used, as shown in Figure 2.6.

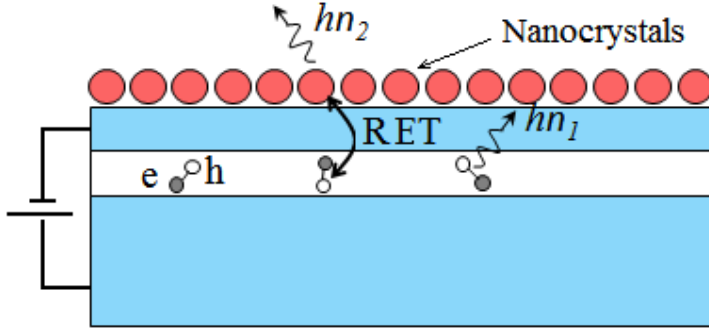


Figure 2.6. A sketch of the hybrid WLED with nanocrystals as emissive layer.

2.4 Non-radiative resonant energy transfer

Fluorescence resonant energy transfer (FRET) or simply resonant energy transfer (RET) is a distance dependent non-radiative energy transfer between two materials which occurs between two dipoles separated by distances from 1 nm and up to 10 nm. This process was first established theoretically in 1948 by Förster [35]. This non-radiative energy transfer appears due to the Coulomb interaction between the donor and acceptor materials. The effect can be understood as an emission and absorption of a virtual photon. High efficiency of the non-radiative energy transfer and was later proven [15], [34], and models of the process have been developed.

In this work we are going to use InGaN QWs and CdSe/ZnS or InP/ZnS NCs as the donor and the acceptor, respectively. This process does not require charge transport. Exciton energy flows from a large band-gap material (donor) to a nanocrystal with a smaller band-gap (acceptor), and therefore, energy transfer occurs without emission of a photon.

2. Theoretical background

A spectral overlap of a donor emission and an acceptor absorption spectra for RET to occur is needed. Additionally, the distance between the donor and acceptor should be small [36], as schematically shown in Figure 2.7.

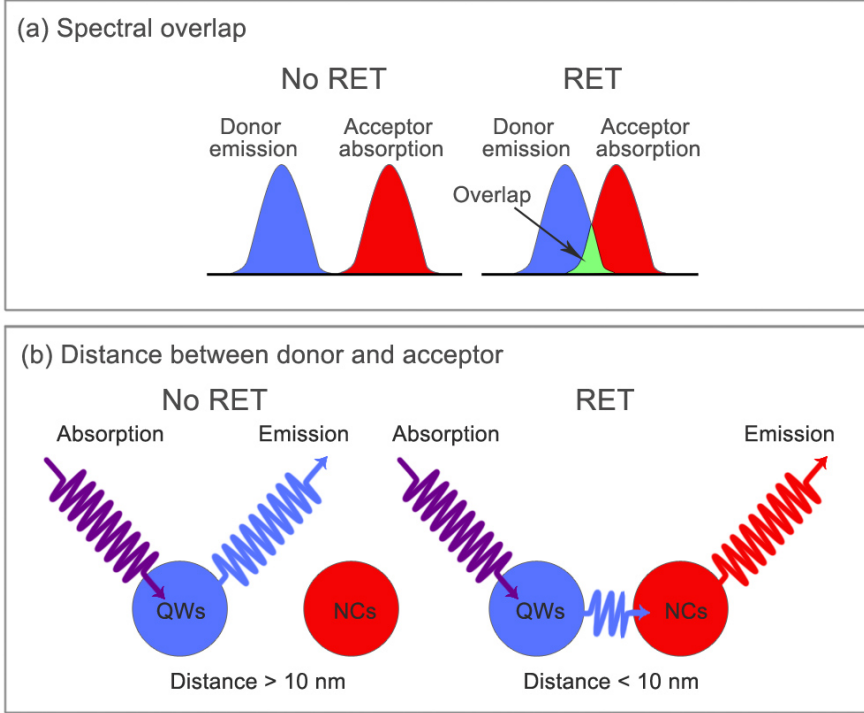


Figure 2.7. Main conditions required for RET to occur: (a) spectral overlap between donor emission and acceptor absorption wavelengths and (b) small distance between the donor and the acceptor.

As mentioned before, the probability of the RET drastically depends on the distance between the QWs and the NCs (Figure 2.8) and is described by the equation (2.1):

$$E_{RET} = \frac{R_0^C}{R_0^C + R^C} \quad (2.1)$$

where E_{RET} is the efficiency of the RET process, R_0 is the so-called Förster radius or critical distance, which is the distance between the donor and the acceptor at which RET efficiency is 50%. R is the actual

2. Theoretical background

separation between the donor and the acceptor and C is the constant, which varies depending on the dimensionality of the dipoles involved in RET. $1/R^6$ dependence describes point dipole-to-dipole energy transfer [36], [37], while layer-to-layer energy transfer depends on the distance as $1/R^2$ [38], [39]; and transfer between a point dipole and a layer is described by $1/R^4$ ratio, which was shown to be the case for RET between InGaN QW and NCs [14], [40], [41].

The critical distance R_0 is determined by the following equation:

$$R_0 = [8.79 \times 10^{-5} \cdot k^2 \cdot n^{-4} \cdot Q_D \cdot J(\lambda)]^{1/C} \quad (2.2)$$

where k is the orientation factor, which depends on an angle between the donor and the acceptor and ranges from 0 to 4 ($k^2 = 2/3$ for randomly oriented donors and acceptors [42]); n is the refractive index of the medium; Q_D is the quantum efficiency of the donor in the absence of the acceptor. Finally $J(\lambda)$ is the spectral overlap integral (see Figure 2.7 (a)), described by the following equation:

$$J(\lambda) = \frac{\int F_D(\lambda) \epsilon_A(\lambda) \lambda^4 d\lambda}{\int F_D(\lambda) d\lambda} \quad (2.3)$$

where F_D is the normalized donor emission spectrum, ϵ_A is the absorption probability of the acceptor, and λ is the wavelength.

Typical values of R_0 for the acceptor materials lie in the range from 3 to 6 nm [42], [43], [44]. Therefore we should expect efficient RET for <10 nm distances. Figure 2.8 presents a dependence of RET efficiency versus distance R . Critical distances from 3 to 6 nm are used as an example.

2. Theoretical background

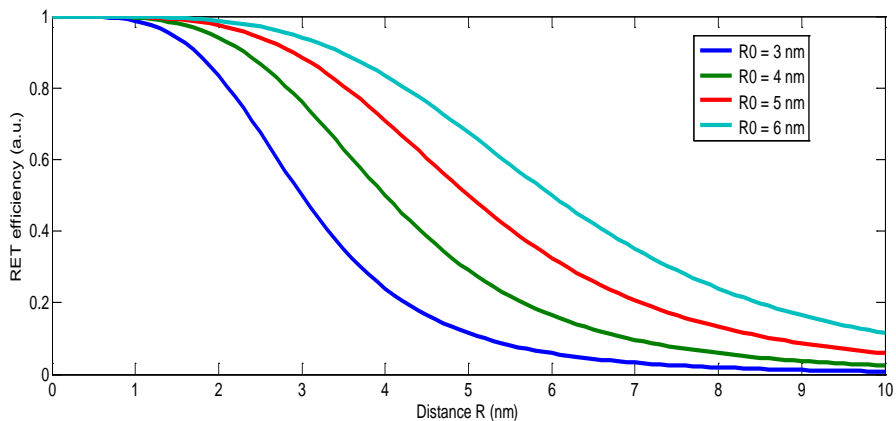


Figure 2.8. Efficiency of RET versus distance between the QW and the NCs. R_0 varies from 3 to 6 nm. Constant n equals to 4.

To summarize, the primary conditions for RET to occur are:

- Close proximity of donor (QWs) and acceptor (NCs), preferably below 5 nm;
- Good overlap of the emission spectrum of the donor and the absorption spectrum of the acceptor, which can be controlled in the system considered in this thesis by choosing NCs with correct absorption wavelength.

2.5 Colloidal semiconductor quantum dots

The information about nanocrystals as a possible color conversion medium for RET is presented in this section. The decision to use colloidal semiconductor quantum dots (QDs) or nanocrystals (NCs) as acceptor layer for hybrid white LEDs comes from their properties. Colloidal nanocrystals have been proposed before as a color conversion medium for white light emitting diodes due to their good quantum yield, combined with tunability of photoemission covering the green-to-red

2. Theoretical background

region (520-700nm), and absorption in the blue region of the visible light spectrum. It has also been proposed that non-radiative exciton energy transfer between a quantum well (QW) of inorganic semiconductors and thin layers of highly emissive colloidal nanocrystals [45] can be promising, as RET should overcome the low absorption probability of the nanocrystals. Moreover, NCs are favorable due to their price and non-toxicity.

Colloidal nanocrystals are nanometer sized semiconductor QDs that are synthesized using colloidal chemistry and processed in a solution [46]. More information regarding their synthesis can be found elsewhere [46], [47]. Due to the small size they exhibit a mixture of solid-state and atomic properties. Optical properties such as wavefunctions overlap, energy levels, and in turn, emission and absorption wavelengths (which also means emission color) can be tuned by changing the size of the NCs in a similar way to the epitaxially grown QDs [48]. NCs are covered with organic surfactants called ligands (Figure 2.9). Ligands play a key role in determining the size and a shape of NCs during the growth and stabilize NCs after the synthesis. Presence of ligands makes it possible to avoid clustering of NCs [47]. In general, the fact that NCs are fabricated using simple chemistry, precise control of the NC size can be achieved, and their low fabrication price makes NCs very competitive and attractive on the market for different applications.

Commercial NCs from the NN-labs were used for the experiments performed during this PhD work [49]. Detailed description of the fabrication methods can be found in the publications from NN-labs [50], [51].

Both NCs InP/ZnS and CdSe/ZnS can be used in white light-emitting diodes as color conversion materials employing RET from the QWs as an energy source. While CdSe and PbSe based NCs show good

2. Theoretical background

carrier dynamics properties and high efficiencies [52], [53], fabrication of InP NCs is not fully established. On the other hand, toxicity of CdSe NCs limits their application areas, so there is a huge interest of less toxic and more “green” InP colloidal QDs.

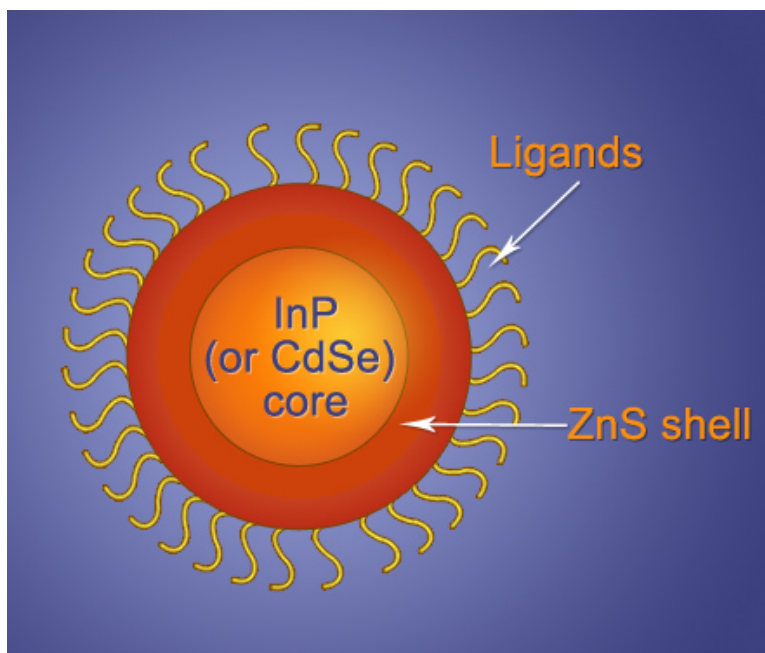


Figure 2.9. A schematic picture of a InP/ZnS (CdSe/ZnS) core-shell colloidal QD with ligands.

Both InP/ZnS and CdSe/ZnS NCs were used in the experiments described in this thesis. Several different sized NCs in a solution (Figure 2.10) were measured in order to vary emitter colors and to select the best option for high quality white LED fabrication.



Figure 2.10. Example of different emission wavelengths CdSe/ZnS colloidal QDs in solution.

2.6 Quality of the white light, CRI index and CCT

There are number of different white light LEDs on the market with different parameters such as color quality and lifetime. The term *lifetime* is self-explanatory: it refers to the work time of the device when it still emits light with the declared parameters. The term "color quality" needs to be explained further. Main two parameters of light are: color correlated temperature and color rendering index.

Color correlated temperature (CCT) is a characteristic of a visible light that has important applications in lighting, photography, videography, publishing, manufacturing, astrophysics and other fields. The color temperature of a light source is the temperature of an ideal black-body radiator that radiates light of comparable hue to that of the

2. Theoretical background

considered light source. Color temperature is conventionally stated in the unit of absolute temperature. Color temperatures over 5,000 K are called cold colors (bluish white), while lower color temperatures (2,700-3,000 K) are called warm colors (yellowish white through red) [54]. Figure 2.11 shows examples of warm, cold and neutral white light.

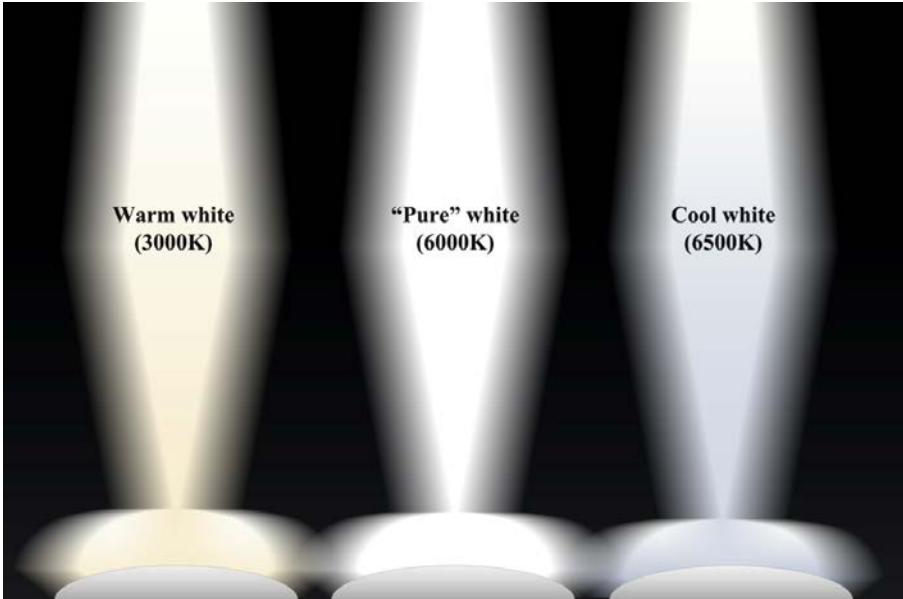


Figure 2.11. Example of white color temperature.

CCT doesn't define how the light source renders colors, and lights with the same CCT may have different CRI. Color temperature refers only to the points on the Planckian locus, while color correlated temperature refers to any light source and the lines that cross Planckian locus show there light sources of given CCT. Different CTs on a Planckian locus line on the chromaticity diagram are shown in Figure 2.12. Planckian locus line defines different color temperatures of the black body radiator, changing from deep red to blue for low and high CCTs, respectively.

2. Theoretical background

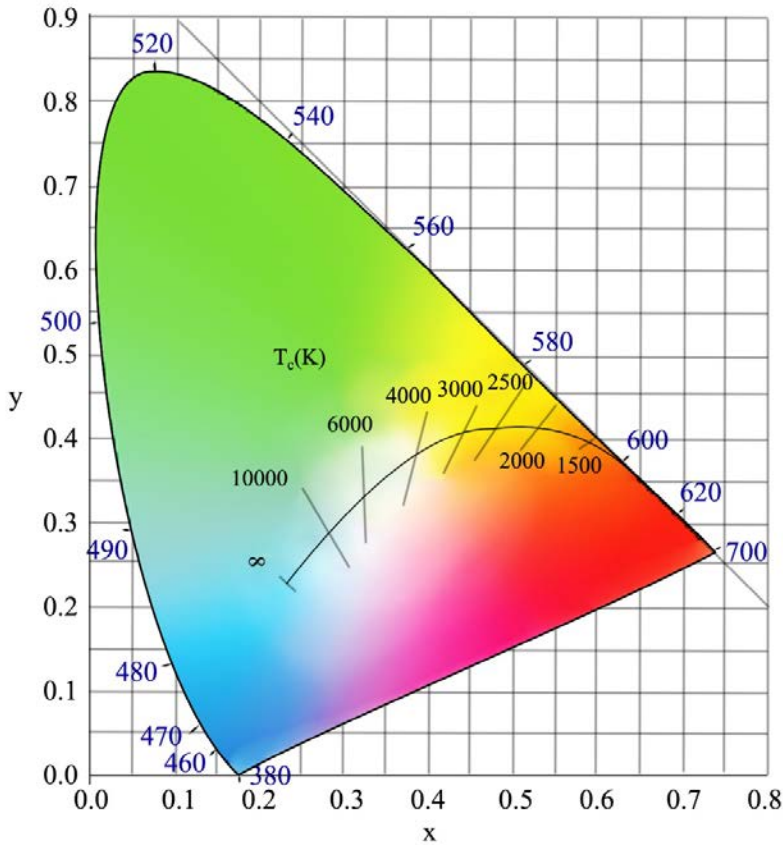


Figure 2.12. Chromaticity diagram presenting Planckian locus with color temperatures. X and Y are chromaticity coordinates.

Color rendering index (CRI) has a value in the range from 0 to 100. It measures how well the colors of objects under illumination are reproduced with the tested light source compared with an ideal light source. Sun light is an ideal light source; incandescent lamps are used sometimes as ideal light source having their CRI rating of 100.

For establishing the CRI of the light source 8 main colors and 6 additional are used. These are not saturated colors (Figure 2.13). They are placed under the illumination with the tested light and the difference between their real colors and perceived ones is calculated. This value called R_a . The best result is 100 and it is achieved when there is no

2. Theoretical background

difference between perceived and real colors, the smaller R_a value (the bigger difference) leads to the worse color rendering. For precise CRI index evaluation both tested and reference light should be of the same color correlated temperature.



Figure 2.13. Test colors used for CRI calculations.

However, CRI is not the best system to define quality of light; if CRI is below 90 it is possible to get the same CRI from two sources which render colors differently. In contrast, two sources with slightly different CRI (by up to 5 points) may render colors almost identically.

However, it is not the best system for WLEDs color rendering either. Although it works rather well for phosphor-based white LEDs, measuring CRI of around 70 – 90, it becomes a problem for RGB or stacked LEDs. Because of their sharp emission peaks they get only CRI of 25-30, at the same time showing good performance and rendering colors close to phosphor containing LEDs according to the human eye.

Despite its numerous drawbacks and a clear lack of sense for some WLED characterization, the CRI system is the only one officially used.

3. Processing in the clean room

Processing of the white LEDs used for the experiments is presented in this chapter. Fabrication process overview is given in section 3.1. More detailed description of the process flow and processes development is further discussed in sections 3.2 and 3.3. Section 3.4 concludes this chapter.

Standard bright LED wafers were obtained from the Prof. N. Wang from University of Bath, UK. Device fabrication was held in Danchip clean room facilities at Technical University of Denmark (DTU) in Lyngby. As fabrication of III-nitrides was not developed in the Danchip before the start of this project, most of the processes described here had to be established as a part of this work.

3.1 Process overview

The process starts from the design of the wafer structure and the device layout, the latter being then translated into a mask. Detailed description of the structure of devices used in the thesis will be shown in the corresponding chapters for the thin cap and patterned LEDs, in sections 5.1 and 6.1, respectively. It flows for both types of devices are identical except for the absence of the patterning step for thin cap LEDs. Short description of the processing flow for fabrication of patterned LEDs is presented in this section, while the detailed step-by-step recipe is described in Appendix A.

3. Processing in the clean room

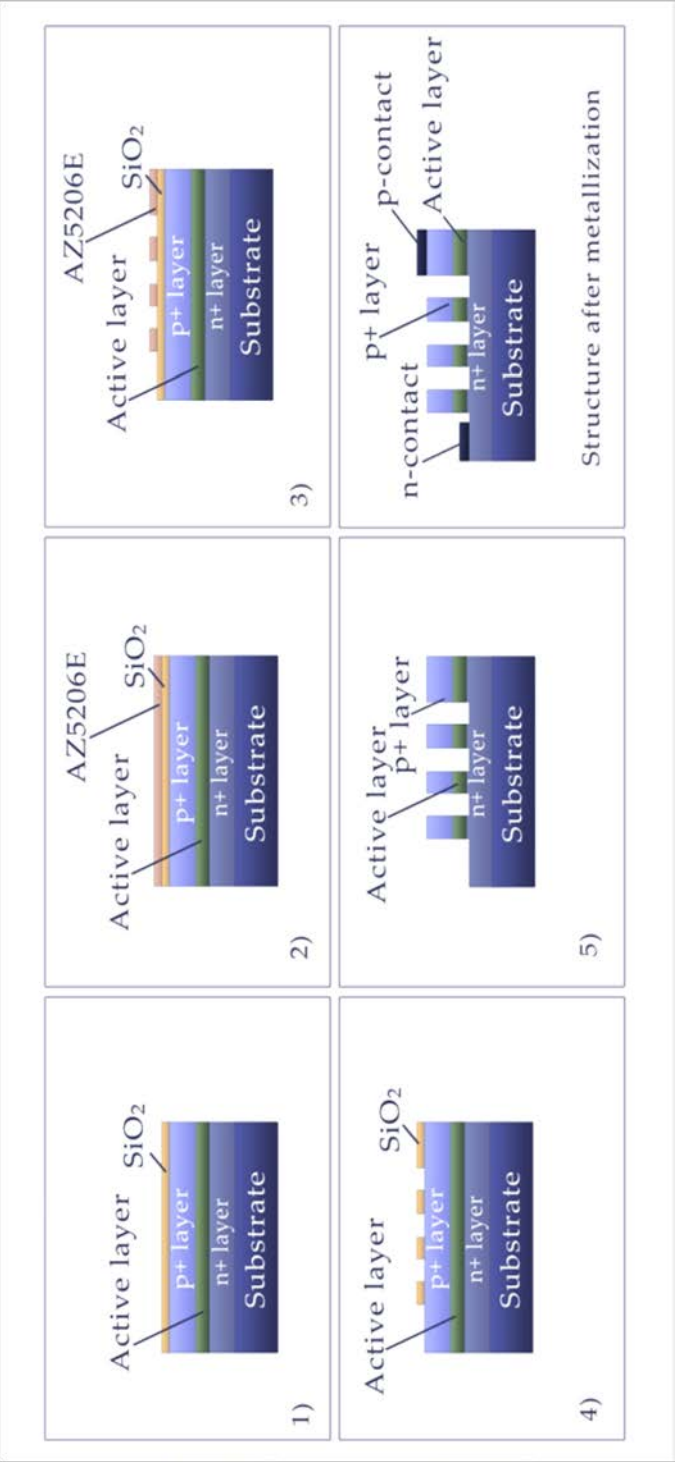


Figure 3.1. Sketch of the fabrication process

3. Processing in the clean room

Figure 3.2 shows a sketch (not up to scale) of the final LED after the clean room fabrication, with the top view on the left hand side and a side view on the right one. The holes in different patterns were of different sizes: with diameters from 800 nm to 2 μm . The chip after processing was cut into smaller pieces, containing 8 diodes each as shown in Figure 3.3. Each cell of 8 LEDs had its own hole size.

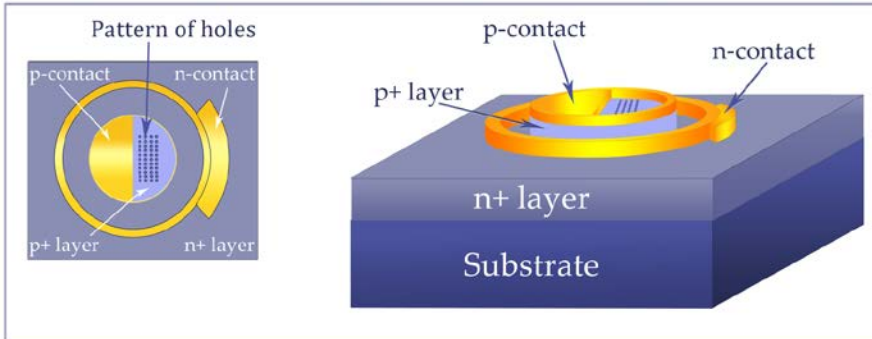


Figure 3.2. Top (left hand side) and 3D view of the device.

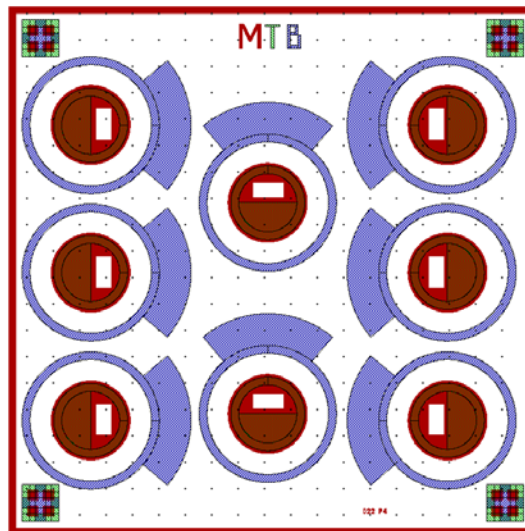


Figure 3.3. Cell, containing 8 LEDs with the same diameter of holes in the pattern; n-type bottom contact is shown in blue, red is used for mesas, and dark green is used for p-type top contact.

3. Processing in the clean room

A fabrication of a hybrid LED consists of 4 main steps: (i) mesa etching and mesa patterning with holes, (ii) p-type metallization with annealing, (iii) n-type metallization and (iv) spin-coating of the NCs. It is performed as follows:

Step 1 – mesa etching and patterning (or just mesa etch for the thin cap samples). Optical lithography is used and the following processes are required within this step.

- 1) Deposition of hard mask (silicon dioxide SiO_2) with total thickness of 300 nm in a plasma enhanced vapor deposition (PECVD).
- 2) Spin-coating of photoresist AZ5206E on top of the glass mask, with thickness of 600 nm.
- 3) Photolithography exposure and development, the pattern is transferred to the resist.
- 4) Etch of the glass (mask transfer) through the openings in the resist, using reactive ion etching (RIE) in CHF_3/O_2 plasma. When the etch is completed, the remaining resist is removed by placing in an acetone for 10-20 minutes with further rinsing in running de-ionized (DI) water. This process is critical before InGaN/GaN etching because any remaining resist on the sample may cause problems in etching. The sample was placed to the O_2 plasma asher to make sure that all the resist was removed.
- 5) InGaN/GaN dry etch using conventional RIE or inductively coupled plasma (ICP) RIE in order to transfer pattern from the glass hard mask to the sample. This is further discussed with the etch details and process development in section 3.2.
- 6) SiO_2 wet etch with BHF chemistry to remove the hard mask.
- 7) Post-etching treatment of the InGaN/GaN in HCl for an hour. This is further discussed in the section 3.2.4

3. Processing in the clean room

The mesa patterning with the holes was performed first using electron-beam lithography (EBL), while in the final processing patterning of the mesa, more expensive but very precise EBL was substituted with conventional photolithography, and features of 800 nm in diameter were fabricated. Alternatively, when EBL technique was used for the patterning, a few extra steps were required between steps 4 and 5 (just after the mesa is defined is a hard mask, but before dry etching step) to reduce etching damage and perform dry etching when both mesa and a hole pattern are defined in a SiO₂ mask.

4.1) Spinning of around 500 nm of ZEP 520A e-beam resist.

4.2) Deposition of thin Al film (20 nm thick) in Wordentec QCL800 metal evaporator (using thermal evaporation technique). One cannot use the e-beam evaporated Al as a charge dissipation layer because the X-ray produced by the 8kV or 10kV electron beam will expose the E-beam resist. This thin metal layer is needed for the reduction of electrostatic charging of the substrate surface (non-conductive resist and glass) in the EBL system during alignment.

4.3) Pattern writing using a 100 kV e-beam lithography system JEOL JBX-9300FS or JEOL FS9500.

4.4) Removal of the Al film by dipping a sample in MF-322 for around 50 seconds with further rinsing it in a DI water bath and drying with nitrogen (N₂).

4.5) Development in ZED N50 developer by dipping for 2 minutes with further rinsing with isopropanol (IPA) and N₂ drying.

4.6) The rest of the E-beam ZEP resist should be removed by placing the sample for 1-2 hours in 60° C Microposit 1165 Remover. Low level of ultrasound in the ultrasonic bath makes removal faster. Higher levels may remove all resist (including exposed).

3. Processing in the clean room

4.7) The etch of the glass (mask transfer) through the openings in resist, in reactive ion etcher (RIE) Plassys using freon/oxygen (CHF_3/O_2) plasma. The resist has to be removed after the etch is finished.

Step 2 – p-type contact metallization.

- 1) 700 nm thick LOR5B lift-off resist spin-coating, followed by 600 nm AZ5406E resist spin-coating.
- 2) Photolithography exposure and development, the pattern is transferred to the resist.
- 3) Metal deposition. For p-type contact 15 nm thick Ni and 200 nm thick Au layer $\text{Ni}_{15}\text{Au}_{200}$ metal combination was deposited by e-beam evaporation.
- 4) Lift-off by immersing samples in a warm (60° C) Microposit 1165 Remover in the ultrasonic bath with low level ultrasound.
- 5) Thermal annealing of contacts in a rapid thermal annealer (RTA) at 610° C for 30 minutes. Development of good-quality p-type contacts process is discussed in sub-section 3.3.2

Step 3 – n-type contact metallization.

This step requires the same operations as step 2, except that different metallization and different process parameters have to be used. $\text{Ti}_{20}\text{Al}_{50}\text{Ti}_{20}\text{Au}_{200}$ metal combination was deposited by e-beam evaporation and annealing was not used.

Step 4 – Deposition of NCs by spin-coating. This allowed uniform deposition of NCs with layer thickness of 10-12 nm.

There are steps in the presented fabrication flow that are standard for all III-V semiconductors in the Danchip clean room. These steps are not discussed here in details as they were not developed within this project. However, some procedures in III-Nitrides fabrication need to be mentioned in more detail.

3. Processing in the clean room

The surfaces and interfaces between the layers are key components in semiconductor devices. With decrease of the size of the device and increase of scale of integration as well as operating powers, the quality and cleanliness of interfaces and surfaces became a very important factor [55], [56], [57]. Samples have to be cleaned by removing grease, particles, metal atom contaminations (if any) as well as surfaces oxides. A sample may be immersed in acetone for 5 minutes for simple cleaning that removes dirt from the surface. Then it is placed in ethanol for 1 minute to remove the acetone traces, rinsed under running deionised (DI) water for 1 minute and dried with N_2 gas. Ultrasonic bath can be used to enhance cleaning. HCl and HF acids and piranha can be employed [58] for more advanced cleaning. A sample has to be immersed in to the piranha solution for 10 minutes, then rinsed under running DI water for one minute and dried with N_2 gas. HCl acid is also effective in cleaning of metallic contaminations of the surface. HCl can also be used for removing surface damaged GaN material. All of these methods can be easily applied to InGaN/AlGaIn/GaN-based wafers in contrast to many other material systems.

The choice of the hard mask for the device patterning also needs to be mentioned. SiO_2 , Si_3N_4 , hydrogen silsesquioxane (HSQ) and some other materials can be used as a hard mask. We have chosen SiO_2 mask because it is easier to deposit and cheaper than Si_3N_4 , while performs well as others. HSQ showed very good results, but it was not selected because this is a negative resist while our structures are easier to fabricate using positive resist.

Deposition processes of glass and metals, performed in PECVD and metal evaporators, respectively, do not differ from other materials. Recipes previously developed in Danchip were successfully used.

3. Processing in the clean room

Some of the samples were wire-bonded to the heat-sink carrier as shown in Figure 3.4. This makes it possible to solder wires (not shown in figure) to the carrier rather than to the InGaN chip for the electrical measurements.

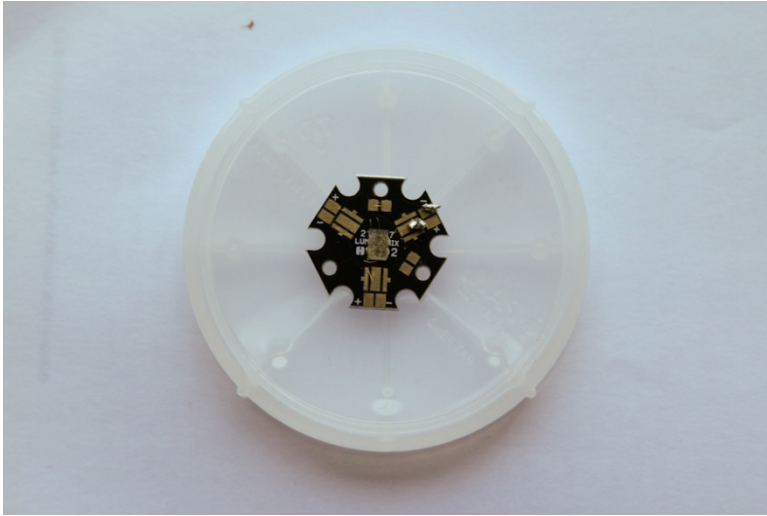


Figure 3.4. Wire-bonding of the InGaN LED chip to the carrier.

3.2 GaN/InGaN etching

Dry and wet etch have some advantages and disadvantages when used for the GaN-related materials. Wet etching is potentially very selective, causes isotropic etching without sub-surface damage and surface roughness. It is cheap, but at the same time its hazardous waste must be handled. GaN and InGaN materials are very resistant to etching by wet chemistries due to their high bond strengths and excellent chemical stability. Therefore a significant amount of work has been applied to establish dry etching [54-56] in Danchip as a patterning technique for GaN and related materials.

3. Processing in the clean room

Dry etching gives good dimension and profile control, and high etching rates for III-Nitrides. Unfortunately, during the dry etch (for ion energies > 60 eV) the surface is ion damaged. There is high possibility of implantation of for example hydrogen. Hazardous gases have to be used, therefore it is a dangerous and very expensive technique. Dry etching has lower selectivity, may cause resist erosion, and mask undercut.

Dry etching is a powerful tool for mesas definition, but control of surface morphology as well as reducing plasma-induced damage is a challenge. High bond energies of GaN related materials compared to other semiconductors make this task even harder. GaN has a bond energy of 8.92 eV/atom, InN 7.72 eV/atom, AlN 11.52 eV/atom, compared for example to the bond energy for GaAs of 6.52 eV/atom. As dry etching causes damage to the sample due to the ions bombarding its surface, post-etching treatment is needed.

3.2.1 Reactive Ion Etching (RIE)

Standard reactive ion etching (RIE) technique was used for SiO_2 as well as initially for InGaN/GaN etching. A schematic diagram showing a RIE chamber and basic principles of etching is shown in Figure 3.5 and 3.6. Both chemical and physical etching mechanisms are utilized in RIE to accomplish good anisotropic profiles without any undercut, with fast etch rates, and dimensional control.

The physical mechanism, sputtering, arises due to the acceleration of ions in the plasma which strike the sample surface with energies of about a few hundred eV. High ion concentration and energy is needed for an efficient process. The fact that etching takes place at low pressures makes it possible to achieve anisotropic etch profile due to the

3. Processing in the clean room

vertical ion fluxes as the mean free path of ions is increased and their scattering caused by collisions is reduced. However, pure sputtering may cause trenching at bottoms of sidewalls, redeposition of photoresist and other materials, charging and ion path distortion. One should also remember that using a high ion energy for improving the etch rate will result in significant surface damage degrading both optical and electrical properties of device.

The chemical part of the etching process takes place due to the formation of reactive species (radicals). They react with atoms on the surface, whose bonds are broken by ions. Volatile products are created and desorbed from the surface. In this case, the etching is governed by the radical diffusion, and the etch rates in vertical and lateral directions become similar. This leads to an isotropic etch. At the same time, use of the low-energy ions helps to avoid surface damage. Therefore, it is very important to combine physical and chemical etch mechanisms in order to get minimal surface damage, good surface morphology at reasonable etch rates.

3. Processing in the clean room

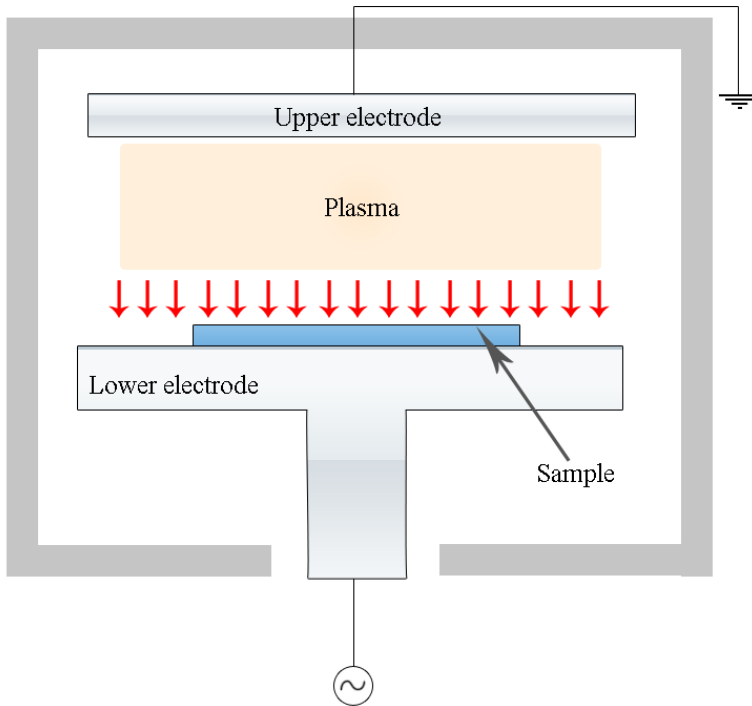


Figure 3.5. A schematic of simple RIE. Plasma is created in the chamber between electrodes by applying a strong RF field.

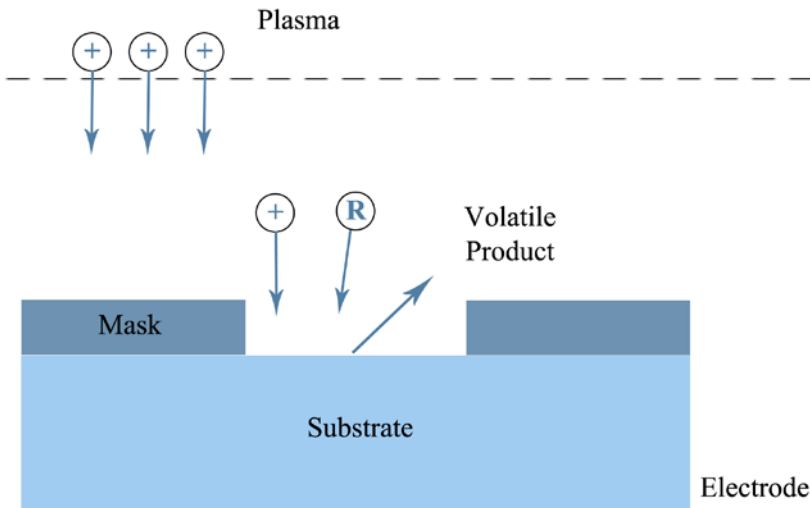


Figure 3.6. Processes during etch in RIE. The plasma provides accelerated ions that bombard the surface and destroy atom bonds, as well as radicals that react with byproducts. Ions are shown as "+" and radicals as "R" in the figure.

3. Processing in the clean room

The RIE used in this work is produced by Plassys. Its reactor is made of aluminum, the chamber volume equals 8550 cm^3 . The sample is placed on the fused silica substrate on top of the bottom (lower) electrode. The radio-frequency (RF) power with frequency of 13.56 MHz is applied between two parallel electrodes (upper and lower one). Plasma is formed between two parallel plates with bottom electrode powered and top one grounded. The maximum power of this RIE is limited to 100W. Ions are accelerated perpendicular to the chamber surface and strike the sample vertically. The absence of a vacuum load lock prohibits the use of toxic chlorine-containing gases, which are the most efficient for III-nitrides etch. This machine has a laser reflectometer installed, which allows monitoring the etch depth by the user in real time, thus it is precise.

Glass etch procedures are well-established in the Danchip clean room. Therefore, we will concentrate on nitrides dry etch as it had never been introduced in this clean room before. Table 3.1 presents boiling points of possible etch products of InGaN and possible gasses used for etching [62]. It is expected that GaN and related alloys can be etched in chlorinated chemistries (with ion assistance for In-containing alloys), I_2 , Br_2 chemistries (with ion assistance to remove InBr_3), or CH_4/H_2 . A CH_4/H_2 combination was used to etch InGaN/GaN samples because chlorinated chemistries [63] were not available in RIE Plassys. Despite the lower etch rate in CH_4/H_2 chemistry, good surface morphology can be achieved as well as more precise control of the etch rate for shallow etched structures. Most of the work for the process development and optimization has been done by Maxim Cremel, a Master student specifically appointed for this project under my supervision.

Because of the carbonated polymer creation on all surfaces when using CH_4/H_2 chemistry [64], [65], one has to use a cyclic etch program

3. Processing in the clean room

in RIE: consisting of CH_4/H_2 sample etch, followed by O_2 step to remove the polymer layer. During the CH_4/H_2 etch cycle the polymer creation competes with the actual sample etch, slowing it down. Pattern transfer issues can also be caused by polymer creation. However, deposition of a polymer layer on the sidewalls is beneficial because it contributes to highly anisotropic etching in CH_4/H_2 based discharges [65], [66]. Duration times of these processes should be optimized in order to make the etching process as efficient as possible. By making the etch cycle too long one may in fact reduce the etch rate and then finally stop it when too much polymer will block etching process. Too little time for etch and too long O_2 cycle also makes RIE etch slower. Therefore, the optimum balance had to be determined. 2 min CH_4/H_2 step length and 1.5 min O_2 step were found to be the optimum. Note that the etch rate also depends on a CH_4/H_2 ratio.

Table 3.1. Boiling points of some possible III-V etch products.

Species	Boiling point (°C)	Species	Boiling point (°C)
GaCl_3	201	NCl_3	<71
GaBr_3	279	NF_3	-129
GaI_3	sub-345	NH_3	-33
$(\text{CH}_3)_3\text{Ga}$	55.7	N_2	-196
		$(\text{CH}_3)_3\text{N}$	2.9
InCl_3	600		
InBr_3	>600	PCl_3	76
InI_3	210	PBr_3	106
$(\text{CH}_3)_3\text{In}$	134	PH_3	-88
AlCl_3	183	AsCl_3	130
AlBr_3	263	AsBr_3	221
AlI_3	191	AsH_3	-55
$(\text{CH}_3)_3\text{Al}$	126	AsF_3	-63

3. Processing in the clean room

To make etching process reproducible even for low etch depths (i.e. for low number of etching cycles) the chamber has to be in the same conditions, including the coating of its walls before each etching procedure. However, a polymer layer is created on a sample as well as on chamber walls during the CH_4/H_2 based etch. Hence, GaN etch rate is going to be different during first and last cycles unless the chamber is preconditioned before the etching starts. Without the preconditioning the polymer layer needs some time to cover the walls of the chamber, thus etch rate will not be stable. This can be avoided by chamber preconditioning must be performed before etching. It has been found experimentally that 10 minutes preconditioning is enough for the process (recipes can be found in Appendix B).

By placing an InP carrier wafer underneath the sample, a higher etch rate with lower surface damage is achieved. This is due to the fact that the InP can decrease the amount of radicals, while leaving an amount of ions at the same level, thus reducing polymer formation.

The control of the etch is a difficult procedure mostly because one does not have direct influence on some critical parameters of the process such as energy and directionality of ions striking the sample (which depends on DC bias voltage), density of etchant on the surface, and velocity of desorption of volatile products from the sample's surface.

RIE Plassys allows control of several parameters such as: (i) composition of gasses and their flows, (ii) chamber pressure and (iii) RF power. In what follows we describe the influence of these controllable parameters on etch characteristics. Note that these controlling parameters of RIE Plassys may influence several critical process parameters simultaneously and in the opposite manner.

We started by varying the composition of gasses. Flows of gasses were chosen such that the total flow of CH_4 and H_2 is equal to 40 sccm

3. Processing in the clean room (standard cubic centimeter per minute). Additionally, the CH_4 flow in this machine is limited to 10 sccm. As a start point, pressure and RF power values of 80 mTorr and 90 W, respectively, were taken because etching with these parameters showed previously good results [67]. DC bias value during the process was around 525 V. GaN etch rates versus CH_4/H_2 ratio are presented in Figure 3.7. It is seen that etch rate increases with increase of the ratio until it saturates around 0.2-0.25, and then it decreases. Further increase of the CH_4 percentage in the chemistry increases the polymer deposition which quenches etch rate. However, low ratios cause larger wafer roughness.

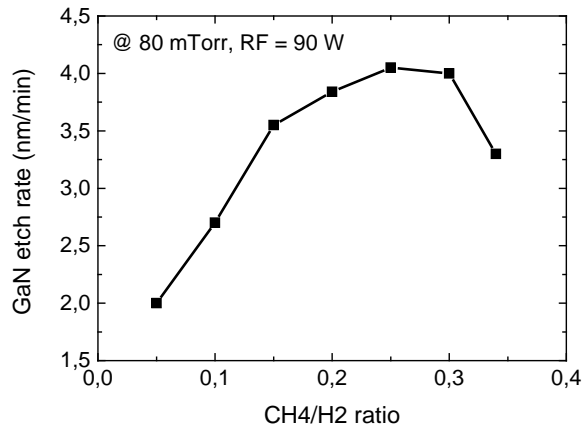


Figure 3.7. Etch rate versus CH_4/H_2 ratio

3. Processing in the clean room

AFM scans representing surface roughness for 0.2 and 0.05 ratios are shown in Figure 3.8. As expected at low amounts of CH_4 the surface is more rough and damaged.

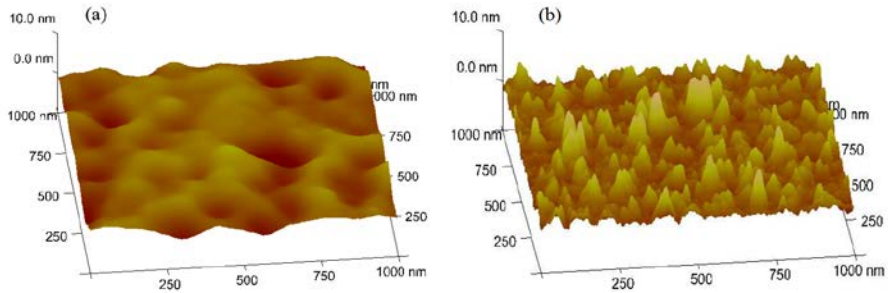


Figure 3.8. AFM scans of GaN surfaces etched with 0.2 (a) and 0.05 (b) CH_4/H_2 ratios.

Etch rate versus RF power is shown in Figure 3.9. The same pressure value of 80 mTorr was used and CH_4/H_2 ratio was chosen to be 0.2. Higher RF power increases the density of the plasma, i.e. density of ions and reactive species (radicals). The energy of the ions as well as their directionality is also getting enhanced at larger RF powers [68]. Thus more physical etch takes place at high powers. Removal of unwanted byproducts can be enhanced by the ions sputtering them away [69]. However, larger RF power, i.e. larger ion energies are going to lead to higher surface damage of the wafer.

3. Processing in the clean room

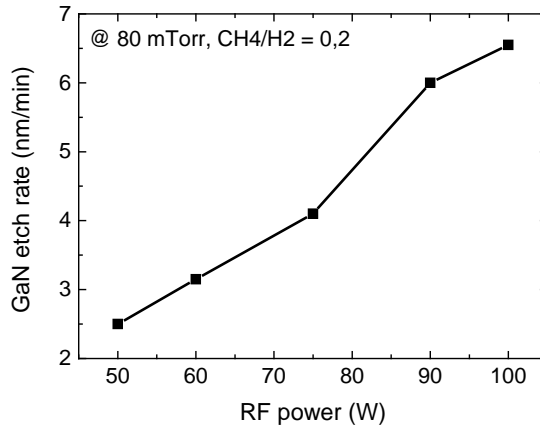


Figure 3.9. Etch rate versus RF power

AFM scans representing surface roughness for RF powers of 60 and 90 W are shown in Figure 3.10. Lower power gives perfect surface morphology after the etch process, although, results from higher power of 90 W are also acceptable. As one can see the increase of RF power does not cause that much surface damage and morphology as the poor choice of CH₄/H₂ ratio does. This can be explained by the fact that increase of RF power increases amount of both ions and etchants, i.e. physical and chemical etch components, keeping the required balance between them for GaN etching.

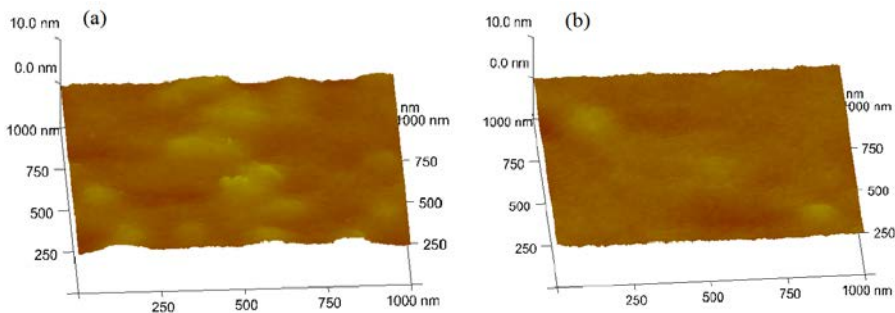


Figure 3.10. AFM scans of GaN surfaces etched with RF power of 90 W (a) and 60 W (b) at CH₄/H₂ ratio of 0.2

3. Processing in the clean room

A dependence of the DC bias on RF power is shown in Figure 3.11. The plasma is more charged at higher RF power. Due to the lower electrode (cathode) auto-polarization to a higher potential in order to equalize charges, DC bias increases. As DC bias voltage affects energy of ions and depends not only on a RF power, it needs to be controlled for a good etch results.

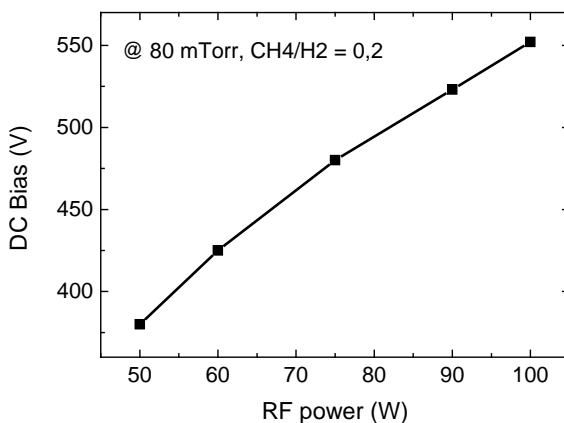


Figure 3.11. DC bias voltage versus RF power. Pressure is 80 mTorr, CH_4/H_2 ratio - 0.2.

DC bias voltage does not only depend on RF power. It mainly depends on the reactor dimensions, i.e. areas of electrodes, which is a characteristic of the machine and does not change from run to run. Gasses and their flows also affect the DC bias but we want to control these values independently due to their high importance for good etching and strong relation to the surface damage. Finally, RF power and pressure affect the DC bias voltage, too. DC bias versus pressure using different powers is presented in Figure 3.12. The pressure was varied between 30 and 80 mTorr, with constant CH_4/H_2 ratio of 0.2, at three different powers: 50, 70 and 90 W.

3. Processing in the clean room

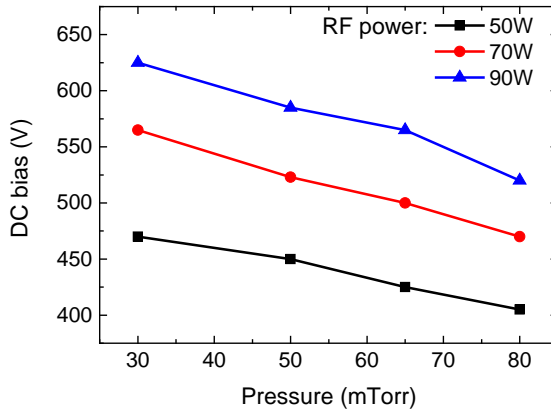


Figure 3.12. DC bias voltage versus pressure at powers of 50, 70 and 90 W shown as black, red and blue lines, respectively.

The pressure of the plasma can influence the composition of gases in the chamber (because gasses have different pumping efficiencies) and the density of reactive species. The directionality and the power of ions is definitely affected by pressure [68]. There are more possibilities for collision of ions with other molecules at higher pressures, therefore the energy and directionality of ions is getting lower. After such collisions new free electrons and positive ions are generated, thus higher pressure will lead to the increase of the number of free electrons, hence DC bias voltage gets more negative. On the other hand, higher power increases the density of reactive species, thus decreasing the mean free path of ions before they hit the surface, and promoting chemical etch rather than physical. This will decrease the electron energy, which inhibits the formation of new electron-positive ion pairs and decreases the number of free electrons and ions. These two effects counteract each other. But at higher pressures as electrons have more collisions and lose their energy which will also affect DC bias voltage. As a result, the DC bias decreases almost linearly, while pressure rises at all shown powers (Figure 3.12).

3. Processing in the clean room

It was also demonstrated that at low pressures (tens of mTorr) energies of ions incident at large angles decrease rapidly with the angle, while for high pressures (hundreds of mTorr) such energies are angle independent [68]. Therefore, etch anisotropy depends on the chamber pressure, which should be kept in the range of tens of mTorr to prevent isotropy processes.

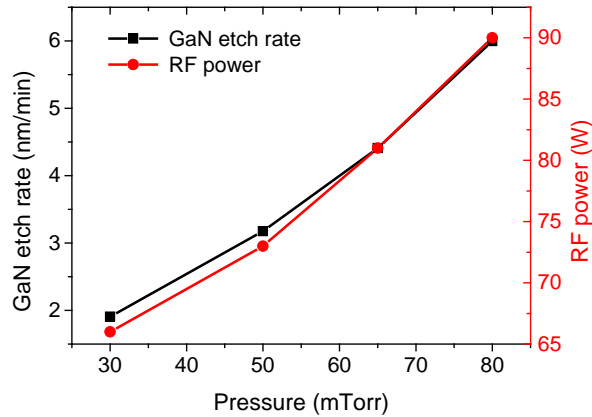


Figure 3.13. GaN etch rate (black line with squares) and RF power (red line with circles) needed to keep DC bias at ~520 V versus pressure.

Figure 3.13 shows GaN etch rate and RF power versus pressure. Reason for this RF power dependence is due to our aim to keep the DC bias voltage constant at around 520 V. As the figure shows, increase of the pressure leads to higher etch rates. It is mostly due to higher amount of reactive species at higher pressures which promotes chemical etch. Ion flux also gets higher with the increase of RF power and increased pressure, when DC bias stays constant (when power increases, voltage is constant, current also increases $P=UI$).

An etching procedure was developed that would provide good surface morphology and low surface damage, but, with a very low etch rate of 6-7 nm/min. The main reason of such low rates is a limited RF power (to 100 W) in this machine in contrast to other RIE machines

3. Processing in the clean room

where good etch results with fast etch rate of 90 nm/min at 300 W were reported [67]. Nevertheless, a low etch rate is outweighed by good surface morphology that has been achieved. The best results can be obtained using CH_4/H_2 ratio of 0.2-0.25, flow rates of CH_4 of 8-10 sccm (where 10 is the maximum, limited by the machine). The power of 90 W rather than 100 W was considered to be used in future, because machine manufacturers do not recommend to use RIE at the highest power. Lowering of the power leads to better surface morphology (which is though acceptable at 90 W, see Figure 3.10) but worse anisotropy. Working pressure is suggested to be 80 mTorr in order to enhance chemical etching and to be sure that the amount of radicals is enough to remove volatile products from the surface and to increase the etch rate. However, this such pressure value gives good results together with high RF powers. In case of using lower RF powers pressure has to be reduced to get decent anisotropy and etch rates. The final recipe for this process is shown in Appendix B.

3.2.2 Inductively coupled plasma (ICP) RIE

In contrast to the conventional RIE, inductively coupled plasma RIE (ICP RIE) is a high-density plasma system. Having a plasma density few orders of magnitude higher than in RIE results in lowering the surface damage because ion energies can be lower for the same etch rate due to the increase of their density. Figure 3.14 presents a simple sketch of an ICP RIE. ICP in contrast to conventional RIE systems has two independent RF sources. The first one is coupled inductively to the coil, then the magnetic field produced by coils in the horizontal plane produces a high-density plasma. The second source is connected to the lower electrode, where the sample is placed, and is used to create a bias

3. Processing in the clean room

needed for acceleration of ionic species from the plasma. The presence of two independent power sources allows independent control of the plasma density, i.e. ion and radical densities, and the ion energy, which allows high etch rates and low surface damage at the same time (not possible in RIE). The temperature of the chuck can be controlled. Moreover, due to the low pressures good etch anisotropy can be obtained despite high plasma density.

A III-V ICP from the STPS company was used for etch. The machine consists of a load lock and a chamber for the actual etching. A carousel is used for sample transportation between the load lock and the etch chamber. RF powers are limited to 1500 W and 600 W for coil and platen, respectively. Cl_2 was used as the main etching gas and Ar as an additive gas. Both Cl_2 and Ar gasses were supplied to the chamber using independent electronic mass flow controllers (MFCs), providing precise control of flows.

3. Processing in the clean room

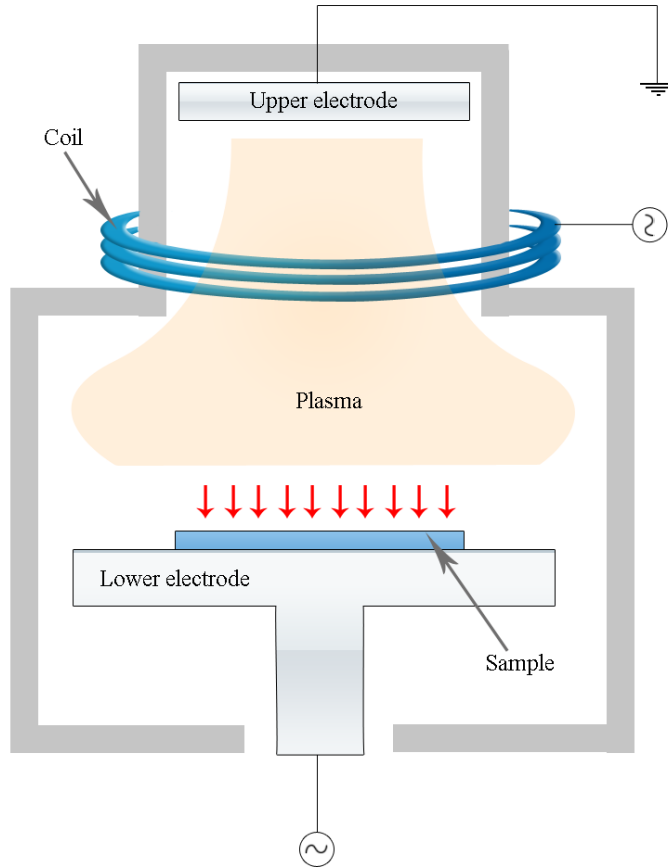


Figure 3.14. A simple schematic of an ICP-RIE

When an ICP RIE was installed and was ready to be used in the Danchip clean room, it was decided to step out from conventional RIE for GaN etching. Chlorine-based chemistry (Cl_2 or BCl_3) is being used instead for etch of GaN-related materials in ICP-RIE. According to literature [70], [71], [72], [73] it should improve etch morphology and speed to improve the quality of the etched device and save the time needed for device fabrication.

In the ICP we first need to precondition the chamber to have a stable etch rate, for the same reasons as for RIE etch. If we do not do it,

3. Processing in the clean room

the etch rate at the beginning will be smaller than after some time. For this purpose a Si carrier wafer with thick layer of SiO₂ on top was placed underneath the samples during the etching as well as during the preconditioning of the chamber. GaN chips were glued with the crystal bond 555 to the carrier wafer. This allows good temperature control of the wafer and, thus, reproducible etch rate from run to run.

The recipe for GaN etching was suggested by the STPS engineers, and after several etches of real samples and slight development it became the main process. The SEM picture of the result of the 75 second etch is presented in Figure 3.15. The top layer with a thickness of 221 nm is the SiO₂ hard mask before it was removed by the HF wet etch. The details of the gases, their flows and etch rate can be found in the Appendix B.

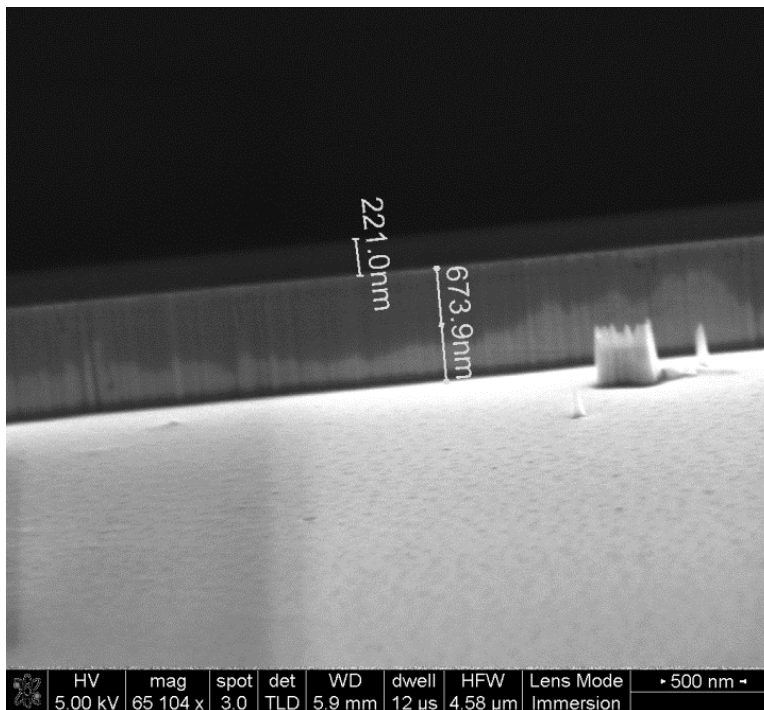


Figure 3.15. SEM image after ICP etch of GaN using SiO₂ as a hard mask.

3. Processing in the clean room

In Figure 3.15 small un-etched islands are visible. This is due to the "micro-masking" effects of the hard mask, when dielectric is spread over the semiconductor. This can be avoided by adding H_2 gas to the etchant gas [65].

3.2.3 Ion Beam Etching (IBE)

The ion beam etching (IBE) is mostly a pure physical dry etch (sputtering) process. In this process Ar ions are directed onto the surface as an ion beam with high acceleration voltage of about 1 to 3 keV. Ions strike out the material from the sample with this huge energy. As the wafer is perpendicular to the ions, etch is anisotropic. It should be noted, that pure sputtering may cause trenching at bottoms of sidewalls, redeposition of photoresist and other materials, charging and ion path distortion. The drawbacks of this type of etching are low selectivity between materials and high damage of the surface.

Although LED processing was performed in the clean room, one has to be careful that surface inside holes is clean and nothing else than NCs is there. In order to achieve this, the processing procedure had one more alternative - to make etch of the holes as a last step after contacts deposition to avoid several lithography steps and metal depositions on a device with the pattern on it. Neither RIE nor ICP available in the Danchip can be used for the etching of structures with metals on top in order to keep these machines clean. Therefore it was decided to try etching in the IBE, where etching of metal-containing structures is allowed. After several tests etching in IBE didn't produce any better results compared to the ICP and we decided to change fabrication process flow and stick to the process that is described in Appendix A, with use of RIE and ICP for hard mask and InAlGaN etch, respectively

3. Processing in the clean room

3.2.4 Post-etching treatment

Post-etching treatment was done on patterned LED structures. Description of the sample is shown in section "Device structure and fabrication" 6.1. In previous sections of this chapter it was already mentioned that dry etching techniques cause damage to the surface of the sample, leading to an increase of defect states, resulting in the non-radiative recombination current leakage, i.e. degrading the optical and electrical properties of the devices [69], [74]. Electrical measurements of completed devices verified that LEDs exhibited current leakage which may have been caused by the plasma-induced surface damage. It is noticed especially while device operates in the low-current regimes. As an example IVs of two diodes without any treatment after ICP RIE etching and an IV of ideal diode are shown in Figure 3.16.

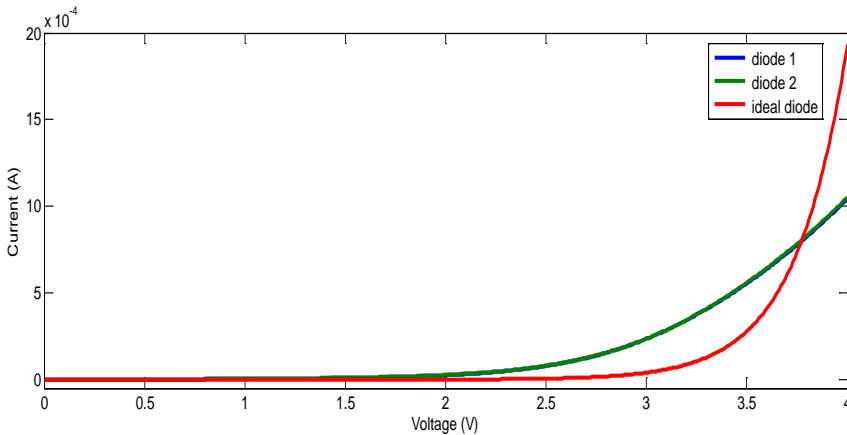


Figure 3.16. Current leakage in diodes before treatment.

Several ways of removing this plasma-induced damage has been demonstrated: Cl_2 plasma treatment [75], [76] or annealing [77], [78]. It was shown that surface damage produced by chemically assisted ion beam etching can be cured by a gentle wet etching and chemical passivation as well. It's interesting that the wet etching depth is only 5-

3. Processing in the clean room

10 nm, which indicates that the damage introduced by the dry etching is very shallow, allowing it to be effectively removed [74], [79].

We have chosen to try three methods: treatment in HF for 60 minutes, in boiling KOH for 60 minutes and in HCl for 60 minutes. This wet etch is completely safe for non-damaged GaN materials, because it removes only damaged surface and can't break the strong GaN bonds.

Results after HF, KOH and HCl post-ICP treatment are presented in Figure 3.17:

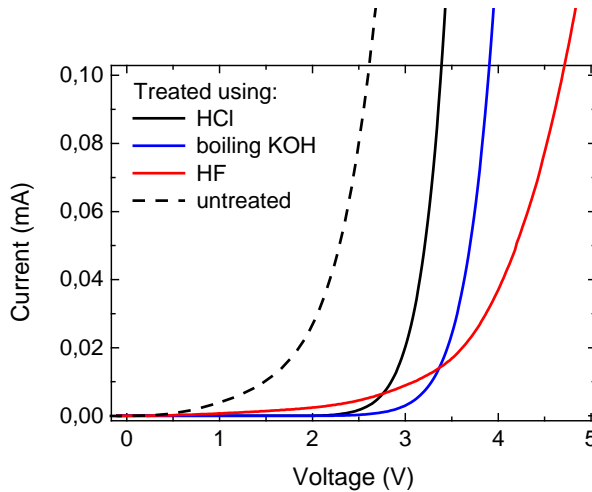


Figure 3.17. IVs of LEDs after post-ICP treatment in different chemistries. Untreated sample characteristic is same as in Figure 3.16 and showed as dashed line.

As it can be seen, both boiling KOH and HCl have removed damaged material and improved the electrical characteristics, while HF have showed slightly worse results. As etch in boiling KOH is more difficult and dangerous to perform and HCl treatment showed best results, it was decided to use the latter one for device fabrication.

IV of LED after HCl post-etching treatment is shown in Figure 3.18, where the inset in the left corner shows IV in a sub-threshold regime, where leakage would be most clearly visible.

3. Processing in the clean room

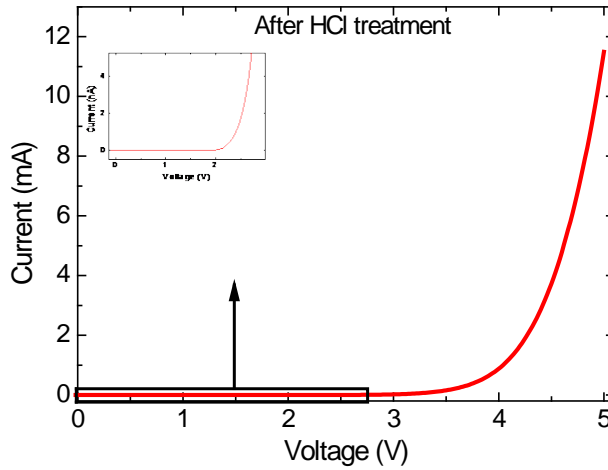


Figure 3.18. Diodes IV after HCl post-etching treatment.

3.2.5 Conclusions

In conclusion, in this section GaN/InGaN, GaN/AlGaN dry etching was discussed using RIE, ICP RIE as well as IBE techniques. Among those methods, ICP RIE from SPTS showed the best results: fast etching with low sample damage. Performance of this instrument allows achieving good enough wall verticality, and low surface roughness at high etch rate. Ion damage of the sample was successfully removed by the post-ICP treatment by dipping the sample for 1 hour in 37% HCl. However, if one needs to use etching of GaN materials in order to fabricate photonic crystal structures, the etching process in the III-V ICP in the Danchip clean room may require further improvement.

3.3 Contacts to GaN

LEDs have to have good electrical characteristics in order device to maintain good light emission and be efficient. Voltage has to be applied to the device using electrical contacts without any losses. Therefore, ohmic contacts play a critical role especially at high powers. High contact resistance will lead to the heating of a device and its failure. The etching damage has been reported to be the main cause of such a degradation [77]. Several methods used to reduce the influence of the damage were discussed in sub-section 3.2.4. Some other methods such as regrowth of p-GaN [80] or p-AlInGaN [81] on etched p-GaN were also proposed but not possible in Danchip.

GaN material differs from other III-V materials (such as GaAs and InP) in that it does not exhibit pinning of the Fermi level. Thus good ohmic contacts should obey the rule that the metal work functions has to be similar but a bit less than the electron affinity of the semiconductor.

However, contacts to p-type GaN are not simple to obtain due to low p-doping levels and high bandgap of GaN. A metal with large work function is needed as an ohmic contact to the p-type GaN (GaN electron affinity + the band-gap $4.1+3.4=7.5$ eV), while for the n-type contact metal work function of around 4.1 eV is required.

In following sub-sections contact development to the n- and p-type GaN is discussed are results are shown.

3.3.1 n-type contact

The electron affinity of the GaN equals to $\chi_{\text{GaN}} = 4.14$ eV. It was shown that Al, with its work function of $\Phi_{\text{Al}} = 4.08$ eV, is more suitable for n-type contact than for instance gold with $\Phi_{\text{Au}} = 5.1$ eV [82]. Gold

3. Processing in the clean room

showed rectifying contacts and interface reaction and phase formation for gold or silver metallization were not observed on GaN. Silver with its work function of 4.3 eV showed weakly rectifying contacts to n-GaN [83]. After annealing Au and Ag, they diffused across the surface [83]. Hence, pure Au or Ag cannot be used for stable ohmic contacts. It was also stressed that cleaning of the GaN surface even not damaged by the dry etching is very critical for good contacts formation [84]. Contamination can partially pin the Fermi level of GaN. We used GaN surface cleaning with dipping in the HCl before metals deposition, which removes native oxides and surface contamination.

We considered several metal composition for n-type contact, based on the published results. Ti/Al ohmics, annealed at 900°C [75], Cr/Pt/Au [85], [86], indium tin oxide (ITO) [87], [88], Al/Cr/Au [89], Ti [87], and Ti/Al/Ti/Au [90], [91] were suggested. Cr/Pt/Au, Ti/Al and Ti/Al/Ti/Au metal combinations were deposited and samples were measured.

Another way to achieve better Ohmics is to highly dope n-GaN. Si dopant reacts with metals, creates an n⁺ surface layer, which makes tunneling possible, resulting in an ohmic behavior. However, it is not easy to achieve high (10^{19} - 10^{20} cm⁻³) doping, and the heat treatment of the sample at high temperatures may be used as a way to increase it. With such heating a shallow donor with increased concentration of free electrons will be established due to the nitrogen vacancies formation [92], [93].

Although Ti has larger work function ($\Phi_{\text{Ti}} = 4.3$ eV) than GaN electron affinity and contacts based on it should exhibit rectifying properties, Ti reacts with GaN and TiN is formed. TiN has predicted work function of 3.74 eV which looks suitable for this material to be used as an ohmic contact.

3. Processing in the clean room

Cr/Pt/Au and Ti/Al metallizations were deposited, results are shown in Figure 3.19. Both of them showed rectifying behavior, so Ti/Al/Ti/Au composition for n-type contact was further tested. According to some authors [90], [91] this metal combination does not require annealing and shows ohmic behavior.

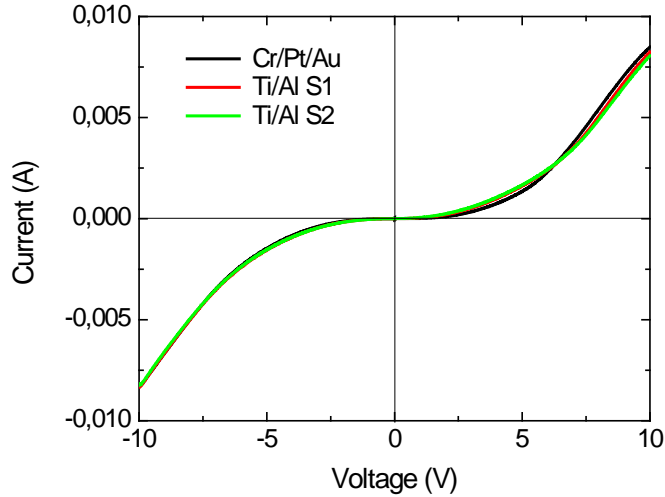


Figure 3.19. IVs for sample with Cr/Pt/Au and 2 samples (S1 and S2) with Ti/Al contacts.

Ohmic behavior has been indeed achieved by using $\text{Ti}_{20}\text{Al}_{50}\text{Ti}_{20}\text{Au}_{200}$ metal combination without annealing, as shown in Figure 3.20.

3. Processing in the clean room

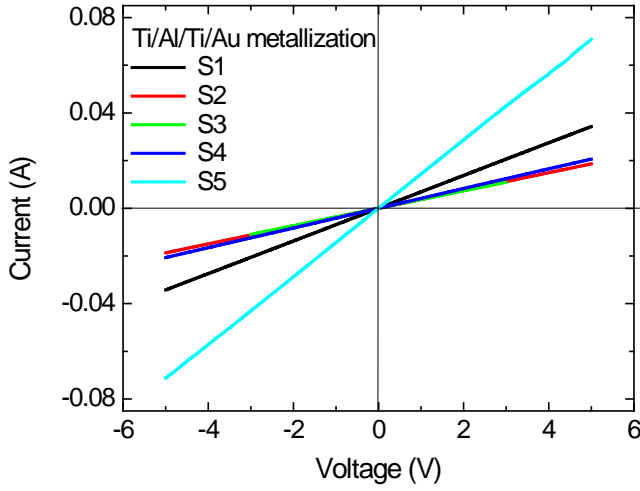


Figure 3.20. IVs for samples with not annealed Ti/Al/Ti/Au metallization on 5 samples with different contact areas.

3.3.2 p-type contact

In contrast to the metallization for the n-type contact, a metal with large work function is needed as an ohmic contact to the p-type GaN (GaN electron affinity + the band-gap $4.1+3.4=7.5$ eV), but no metals have such a high work function. Therefore in order to make ohmic contacts to p-type GaN one has to use highly dope p-GaN and choose appropriate metal combination.

Based on literature several metallization has shown better characteristics. Ti/Mo/Au was used for diodes emitting in violet spectrum range [94], however they were non-ohmic. Pd/Au contacts [75] showed good properties, and other options were Ni/In [95], Ni/Au [95], [96] and Cr/Au [97] metal combinations.

Among these metallization schemes, only some were available in Danchip and NiAu metal combination was chosen after Cr/Au showed non-ohmic behavior. As deposited NiAu showed non-ohmic behavior,

3. Processing in the clean room therefore annealing was considered. Figure 3.21 presents some of the annealing parameters tested while the details of annealing temperatures and times are presented in table 3.2.

Table 3.2. Annealing conditions for samples A, B, C, D, E and F.

Sample name	Annealing conditions
A	@ 850°C for 5 minutes
B	@ 850°C for 1 minute 20 sec, then 3 min @ 350°C and 1 min @ 850°C
C	@ 850°C for 1 minute, then 3 min @ 350°C and 1 min @ 850°C
D	@ 900°C for 5 minutes
E	@ 850°C for 30 seconds
F	@ 610°C for 30 minutes

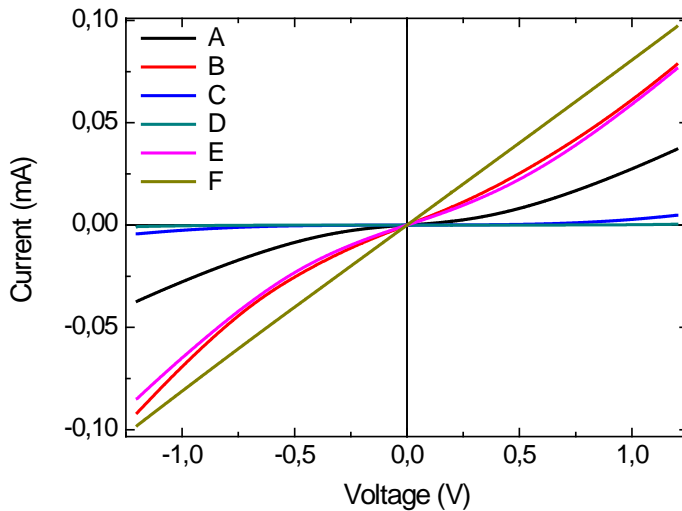


Figure 3.21. Current-voltage characteristics of NiAu contact annealed at different conditions.

I-V characteristics of the device with contacts annealed at 610°C were measured in three different points to make sure that results are

3. Processing in the clean room

reproducible. Results are presented in Figure 3.22. It is interesting that low annealing temperature provided better contacts than higher temperatures of 800-900°C, mentioned in papers as the most suitable temperatures for p-type contact to GaN [95], [96].

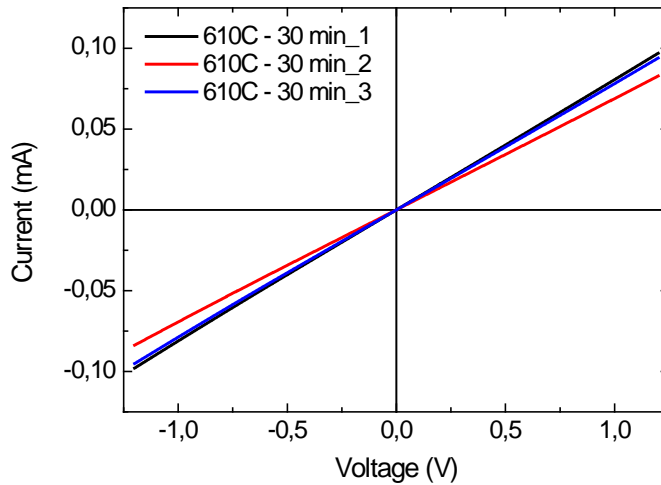


Figure 3.22. Current-voltage characteristics for the 3 different contact points.

In order to allow contacts use for the wire bonding, a thicker Au layer (of 200 nm) had to be used compared with the initial value. Thus the final combination for the p-type contact is $\text{Ni}_{15}\text{Au}_{200}$ annealed at 610 °C for 30 minutes.

3.3.3 Transmission line measurements

Transmission line measurements (TLM) or transfer length measurement is a technique used to measure the contact resistance between metal and semiconductor as well as the sheet resistance of the semiconductor layer. It relies on 2-terminal resistance measurement of a series of well defined contact lines with different length between contacts. As shown in Figure 3.23, the equivalent circuit of the sample

3. Processing in the clean room and measurement circuit consists of a probe resistance R_p , a probe-to-metal contact resistance, R_{cp} , a semiconductor sheet resistance R_s , and a metal-to-semiconductor contact resistance R_{cs} . A Keithley 4200 semiconductor characterizing system (SCS) was used as a voltage source and ammeter. One end of the probes is connected to the sample's contact pad and another is connected to the Keithley. The current flows from the SCS to the sample and the signal is analyzed also in the Keithley.

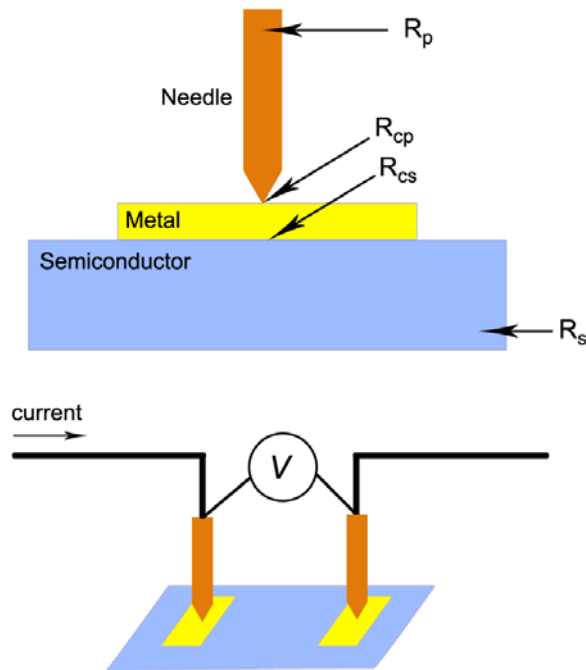


Figure 3.23. A sketch of contact resistance measurement.

The equivalent circuit for the measurement of the contact resistance is shown in Figure 3.24.

3. Processing in the clean room

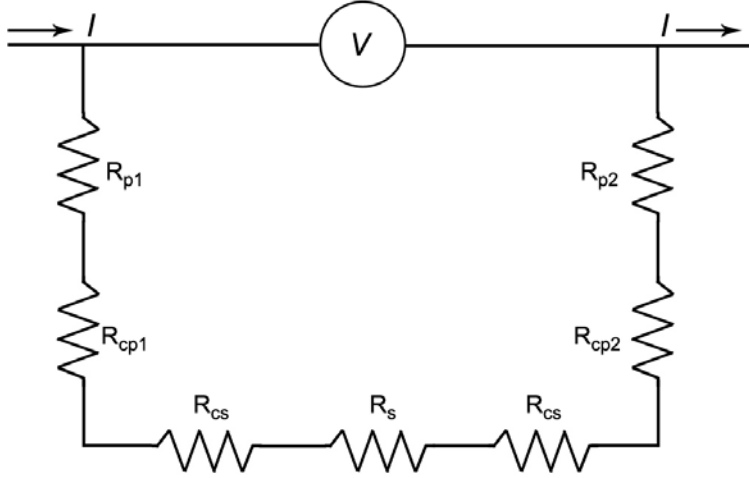


Figure 3.24. The equivalent circuit for the contact resistance measurement. R_p , R_{cp} , R_{cs} and R_s represent probe, probe-to-metal contact, metal-to-semiconductor, and semiconductor sheet resistances, respectively.

Since the resistance of the voltmeter is very large (ideally infinitely large) compared to the probe resistance and probe-to-metal contact resistance, R_p and R_{cp} can be neglected. Thus, total resistance R_T is expressed as follows:

$$R_T = 2R_c + R_s = V/I \quad (3.1)$$

where V is the voltage reading from the voltmeter and I is the current flowing between the two current-carrying probes.

In order to obtain contact and sheet resistances one needs to measure a series of contacts separated by various distances. An example of such a structure is shown in Figure 3.25. The structures used in this thesis are shown in Figure 3.26. This structure was made in a special program L-Edit that is used for making a design of a layout of the mask. Dark green rectangles are the contact pads with the area $50 \times 750 \mu\text{m}^2$. Resistance is measured for each pair of pads, as shown in Figure 3.27, where distances in the inset correspond to distances shown in Figure 3.25.

3. Processing in the clean room

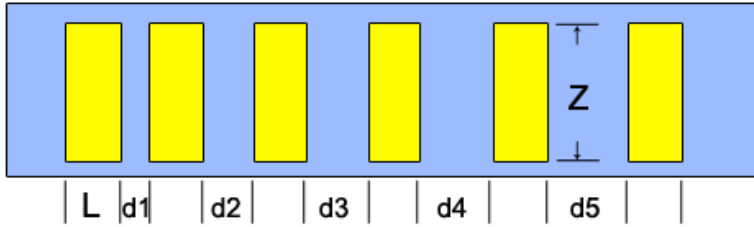


Figure 3.25. A sketch of contact pads for TLM.

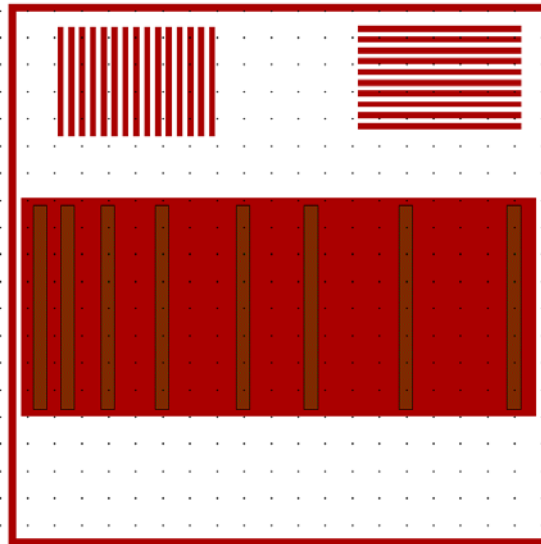


Figure 3.26. Real structures, image from L-Edit. Red background shows mesa, white area is etched away. Contact pads are on p-type GaN.

The measured resistances are then plotted versus separation distance as shown in Figure 3.28. Black squares, connected with the black lines are the data from the measurements, red line shows the fitting and blue line continues the fitting line until intersection with the Y-axis. According to the equation 3.1 we neglect other resistances except the contact and sheet resistances. The slope of the line is the sheet resistance, while the intercept with the Y-axis is doubled value of the contact resistance.

3. Processing in the clean room

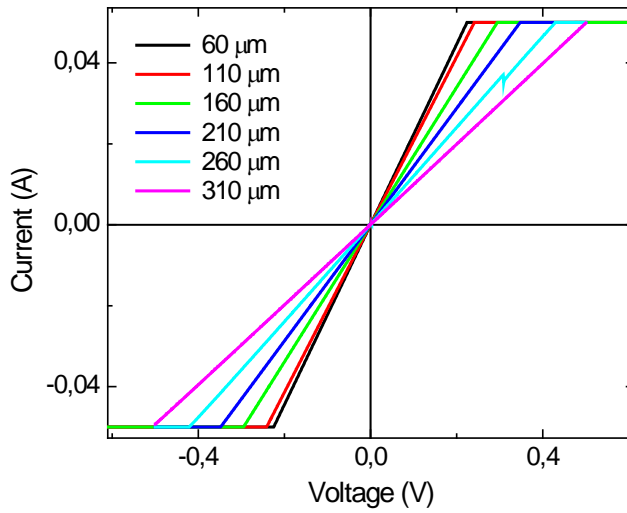


Figure 3.27. I-V measurements for the TLM.

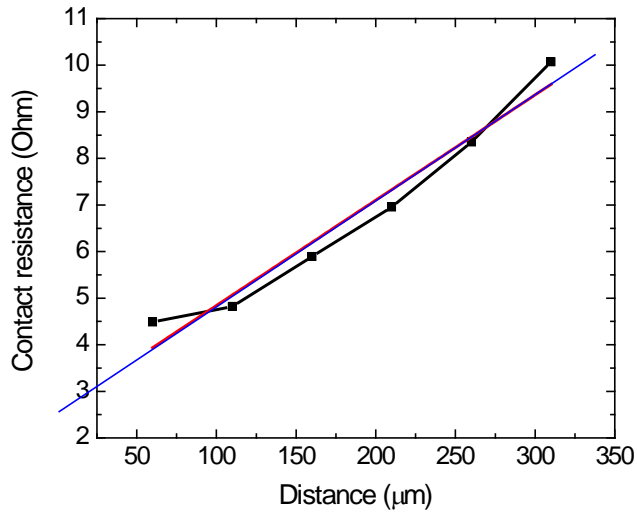


Figure 3.28. TLM for Ni/Au metallization.

The contact resistance R_c read from the fitted line equals $1.55 \, \Omega$ and therefore, the specific contact resistance ρ_c (or R_{cs}) equals $58 \cdot 10^{-5} \, \Omega \cdot \text{cm}^2$. This is rather a high value, however this is most likely due to the

3. Processing in the clean room

fact that R_p and R_{cp} could not be neglected in 2-terminal measurements. In cases when metal-to-semiconductor contact resistance is rather small, 4-terminal configuration (with four probes) should be used to eliminate the parasitic resistance induced by the probes and cables (R_p and R_{cp}). The difference in measurements performed in 2- and 4-terminal configurations has been shown to be up to 1 order of magnitude [98]. Even the value of $R_c \sim 1.55 \Omega$ is sufficient for LED measured in this thesis.

3.3.4 Conclusions

In conclusion, in this section metal combinations for the Ohmic contacts to both p- and n-type GaN were discussed. Contacts formation to the GaN material is different from other III-V materials because Fermi level pinning doesn't occur in GaN and only one simple rule has to be obeyed for the n-type GaN contact in order to have good ohmic contacts – that metal work function has to be less than electron affinity of the semiconductor. It is quite easy to do for n-type GaN, where electron affinity $\chi_{\text{GaN}} = 4.14 \text{ eV}$, but starts to be difficult for the p-type material where large working functions of around 7.5 eV are required due to the GaN band-gap. High doping of p-type GaN is required for the better contacts. For the n- and p-type contacts metal combinations of $\text{Ti}_{20}\text{Al}_{50}\text{Ti}_{20}\text{Au}_{200}$ (not annealed) and $\text{Ni}_{15}\text{Au}_{200}$ (annealed at 610°C for 30 minutes), respectively were employed.

3.4 Conclusions

This chapter was devoted to the processing of the devices performed in the Danchip clean room. Full fabrication cycle of the white

3. Processing in the clean room

LED was shown. Either photo- or electron beam lithography was used for sample patterning. A detailed recipe for the diode fabrication is introduced in the Appendix A. More stress was put on the etching of InGaN/AlGaN materials, including RIE and ICP RIE techniques. Etching recipes were established and results showing good control of the etch depth, surface morphology and verticality of walls were presented. ICP-induced surface damage was removed with post-etching treatment by dipping the sample for a hour in a beaker with 37% HCl. Development of metallization for p- and n-type GaN was described that lead to ohmic contacts of low contact resistance.

4. Characterization techniques

4.1 Photoluminescence measurements

Photoluminescence spectroscopy measurement technique is a widely used contactless, non-destructive characterization tool that allows probing of the electronic structure of the investigated material, and is a basic tool to characterize optoelectronic materials.

4.1.1 PL measurements in the lab

Some part of the PhD was devoted to design and establishment of the PL measurements setup, which required a lot of time, patience, and diligence.

Figure 4.1 shows a sketch of a PL setup built during PhD and used in this thesis for the analysis of the samples. A photo of the PL setup is presented in Figure 4.2. In order to excite a sample, a blue pulsed laser diode from PicoQuant emitting at 405 nm as well as a green CW laser diode were used. Emission energy of the blue laser (3.06 eV) was below the band-gaps of GaN (3.4 eV) and ZnS shell of the NC (3.54 eV), allowing carriers injection directly to the InGaN/GaN QW and the InP (or CdSe) core of the NC for the QWs or NCs analysis, respectively. The green laser emitting at 532 nm was used for the excitation of only NCs deposited on the top of the InGaN QWs to examine their characteristics without an influence of carriers or/and photons from the underlying QW. An excitation pulse energy density of 20 mJ/cm² of the blue laser was used for the experiments.

4. Characterization techniques

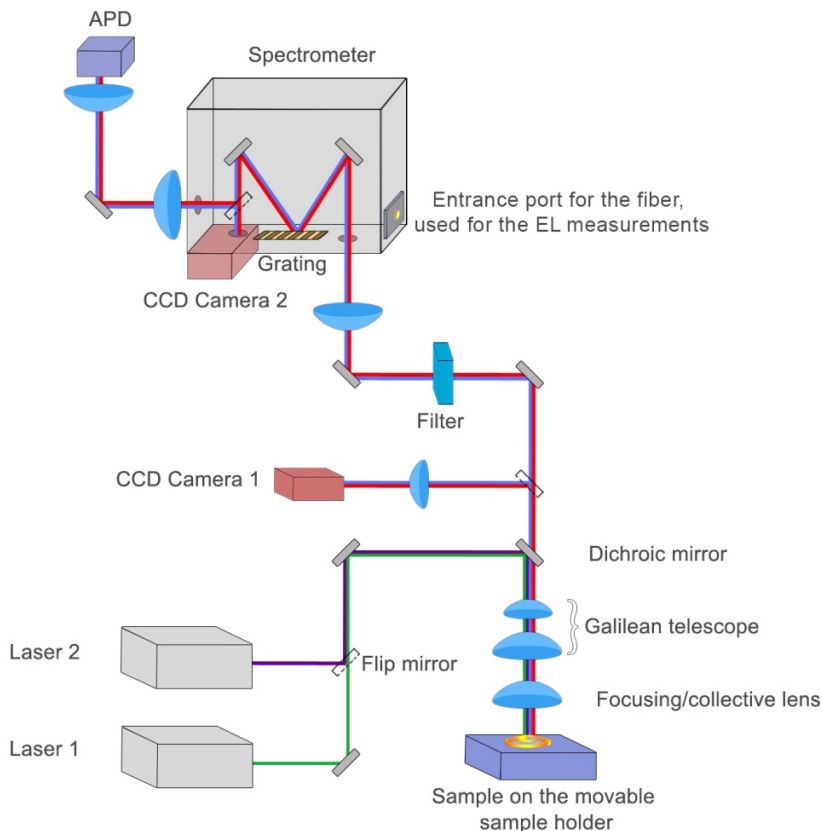


Figure 4.1. A sketch of the PL setup in the lab. Laser 1 and laser 2 are the lasers emitting at 532 nm and 405 nm wavelength, respectively. CCD camera 1 is usual visible camera in order to grab and then transmit image of the sample to the monitor of the computer. CCD camera 2 is Si-based CCD for visible part of spectrum. Filter – any filter needed for specific measurement.

Light emission from the sample was focused on an input slit of the Andor spectrometer and was further guided either to the Andor Si CCD camera or to the APD. The size of the output slit opening led narrow 6-7 nm wide spectrum band, with the peak emission center set by user and controlled by the spectrometer, to reach APD.

4. Characterization techniques

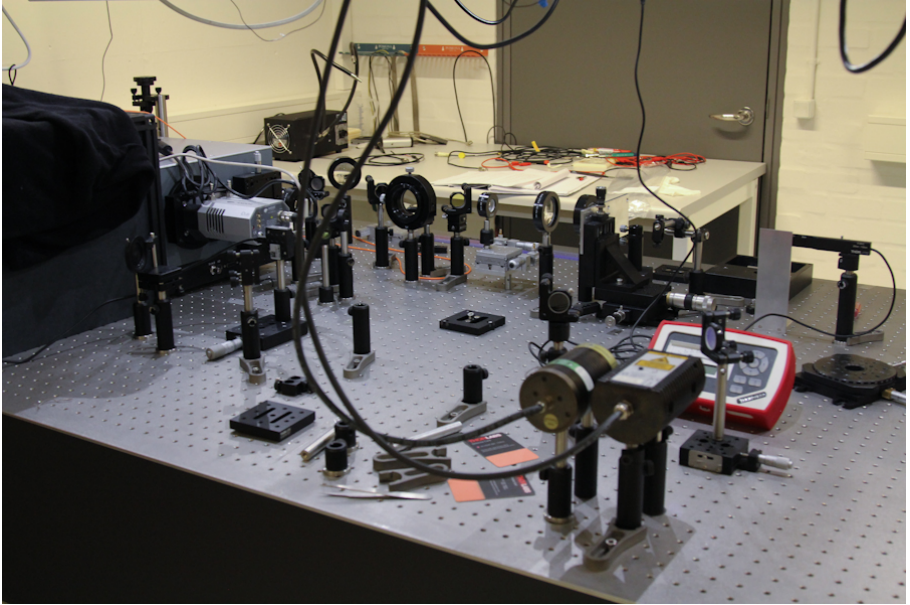


Figure 4.2. A PL setup.

For low temperature measurements a cold finger cryostat cooled with either liquid N_2 or liquid helium was used (Figure 4.3).

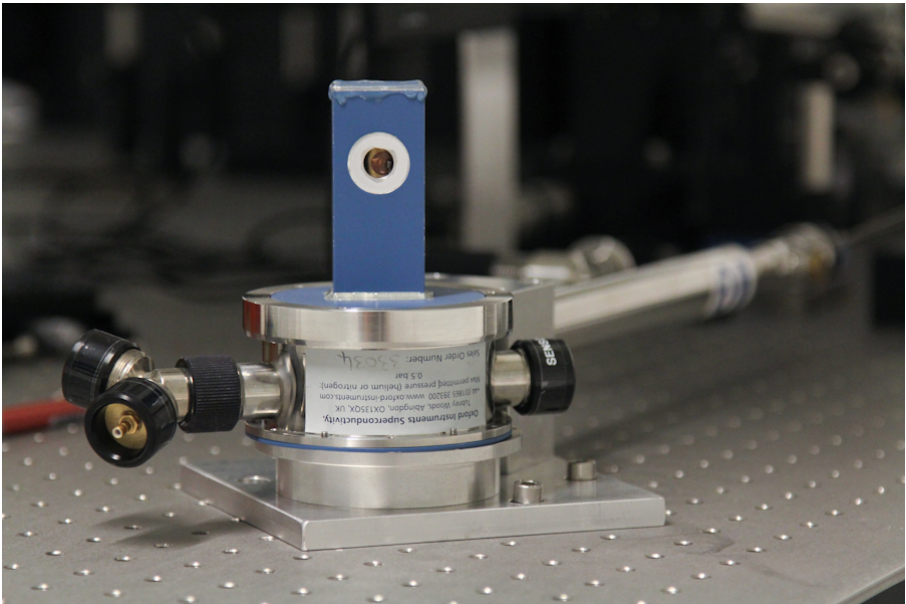


Figure 4.3. Cold finger cryostat

4. Characterization techniques

4.1.2 PL-mapper

The main task of a PL-mapper is to acquire a full wafer (up to 6 inches in size) PL map in one measurement within a short time, obtaining PL data at a grid of points covering the whole wafer with specified distance between the points on the grid. For this purpose Rapid Photoluminescence Mapper RPM2000 from Nanometrics, located in the Danchip clean room, was used.

The PL mapper was equipped with the blue 405 nm and green 532 nm lasers allowing pumping of both the InGaN QWs and NCs (using blue laser) or selective pumping of the NCs using the green laser. Excitation laser beams hit the sample surface at an angle in order to provide spatial filtering of the laser light. The beam is normally focused to a spot with a diameter of approximately 100 μm . The PL produced by the sample is collected by reflective optics coupled to a 0.3 m monochromator, providing excellent throughput across the spectral range. The RPM2000 can also provide true image quality PL mapping at high spatial and spectral resolutions, exhibiting the ability to examine hundreds of thousands of points on wafers up to 150 mm in diameter. It is possible to map with 0.2 mm spatial resolution and such an integrated map will correspond to over 455,800 points. the acquisition of such a map takes only 8 minutes [99]. For wafers up to 100 mm in diameter, spatial resolution is increased to 0.1 mm.

Maps, obtained with the PL mapper can be further analyzed, i.e. each point of the map contains information about the PL spectrum which is very useful. However, the PL-mapper is qualitative rather than the quantitative tool. Using the PL-mapper one should keep in mind different tunable parameters, such as slit size, laser power, gain, scan rate which have to be similar if one wants to compare intensities of different maps. The drawback of this device is that measurements using

4. Characterization techniques

identical parameters are not completely reproducible. It should be noted however that the differences from run to run are quite small, thus wafers with large (10% and more) difference in the amount of emitted signal can be compared. Examples of maps will be shown in sections 5.1 and 6.1 for thin cap and patterned samples, respectively.

4.1.3 Micro-PL

As our samples are patterned and we are interested in comparison of PL intensity behavior in different regions: in the patterned region and far away from it, a good spatial resolution is required. Unfortunately, PL-mapper with its resolution of 0.1 mm is too far from satisfying our needs. For better and more precise spatially resolved PL measurements, a micro-PL setup was used. A simple sketch of the setup is presented in Figure 4.4. Micro-PL measurements were performed in a collaboration with Dr. Alex Huck from DTU Physics, using his setup modified to suit our samples. A pulsed 405 nm laser with train of 70 ps wide pulses was used for optical pumping. A 420 to 520 nm band pass (BP) filter in front of the avalanche photodiode was used to separate the QW emission from the laser and NC signals. For measurements of the NCs a 562 nm long-pass (LP) filter was used instead. The NCs PL signal was also measured under a selective, off-resonant excitation of the NCs with a pulsed 532 nm laser with a pulse width of around 6 ps.

4. Characterization techniques

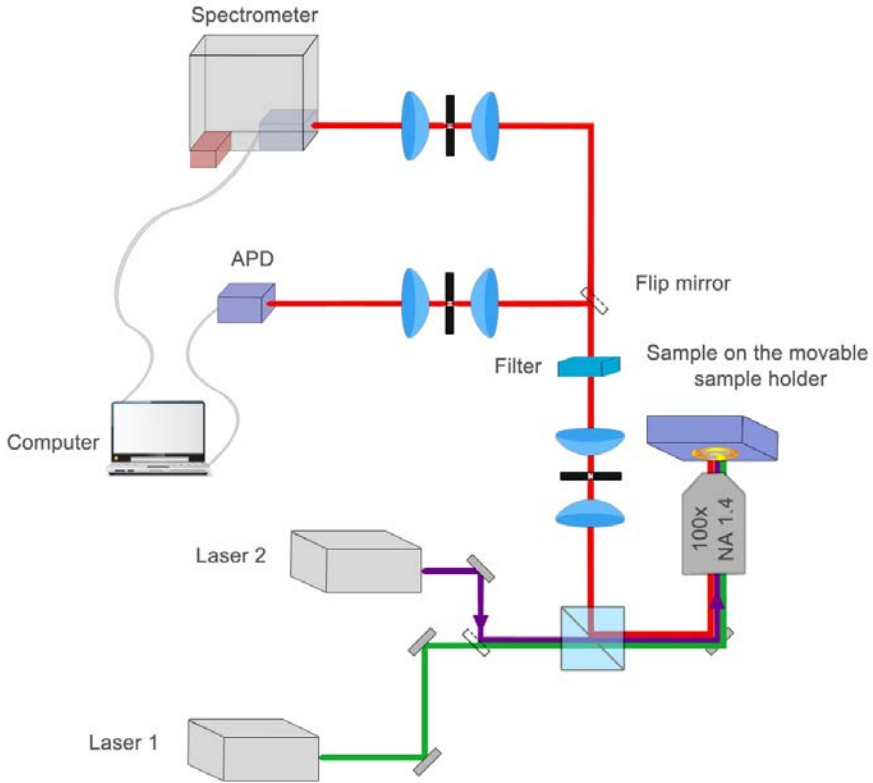


Figure 4.4. Sketch of the micro-PL setup.

The principle behind a for micro-PL are the same as for macro PL except that a sample is placed on the movable sample holder, whose position is changed in a controlled way using piezostages. By correlating the movement of the stage with the data acquisition, a map of PL intensities is obtained. An example of such a map with dimension 9 by 9 μm is shown in Figure 4.5. The spatial separation between points in the map is 130 nm. However, it is not the spatial resolution of the map, because it is also affected by the laser beam size. The laser beam sizes were approximately 0.8 μm and 0.6 μm in diameter for the blue and the green laser, respectively, moreover the beam shape of a blue excitation was slightly elongated, giving rise to some unwanted signal

4. Characterization techniques redistribution. The real spatial resolution was thus limited by the excitation beam sizes rather than the precision in the sample position change. These facts were taken into account during the analysis of the signal from these measurements.

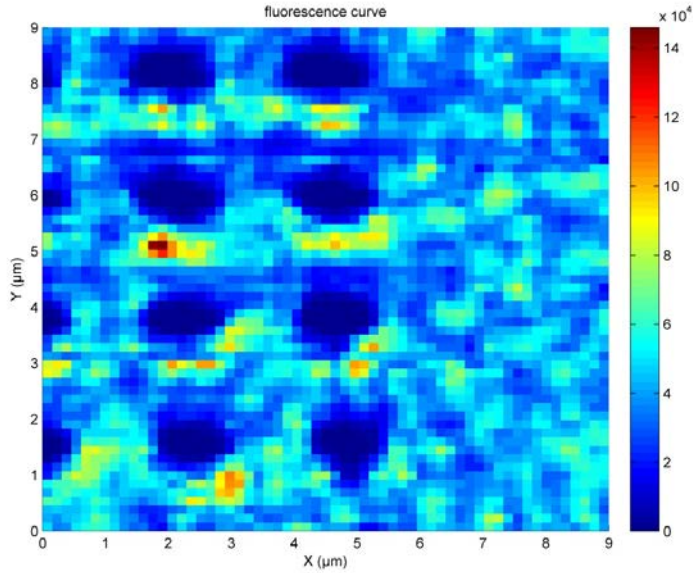


Figure 4.5. Example of micro-PL map acquired on a patterned LED under illumination with a 405 nm laser.

4.2 Time-resolved PL

Steady-state PL measurements are simple, fast and do not require complex setups and expensive equipment, but in fact only limited information is accessible from simple PL measurements about carrier dynamics due to the time averaging process. In order to gain information about carrier dynamics, a time-resolved PL (TRPL) is used. In this measurement, sample is excited with a pulse of laser light shorter than the carrier lifetime and the intensity of PL is measured as a function of time.

4. Characterization techniques

In this thesis TRPL was used to reveal a presence of RET as well as to characterize device decay time components.

For measuring TRPL time-correlated single photon counting (TCSPC) technique was used. TCSPC technique has been developed in late 1960s from measurements of excited nuclear states [100], [101]. Since then, the quality and time resolution was improving and the technique became widely used. It is based on a repeating of a registration of single photons, emitted by the sample under pulsed laser excitation.

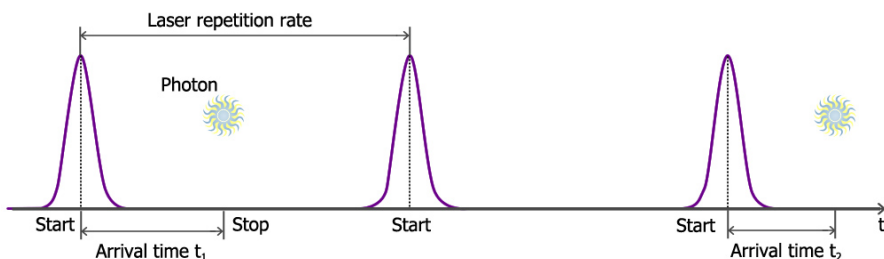


Figure 4.6. A sketch showing principles of TCSPC method

Fast laser pulses with high repetition rate excite the sample. Light intensity must be kept quite low so the detection of more than one photon within the period between laser pulses is very unlikely. It should be noted, that there are some periods where no photon is detected. When a photon is detected, its arrival time is measured. In this case the laser pulse arrival is the time reference and an avalanche photodiode (APD) or a single photon avalanche diode (SPAD) is used for a signal detection. A sketch in Figure 4.6 shows schematically when photons are detected. The measurement is repeated for each incoming laser pulse until the end of the acquisition (i.e. collection) time, set by the user.

More clear presentation of principles of the TCSPC is presented in Figure 4.7.

4. Characterization techniques

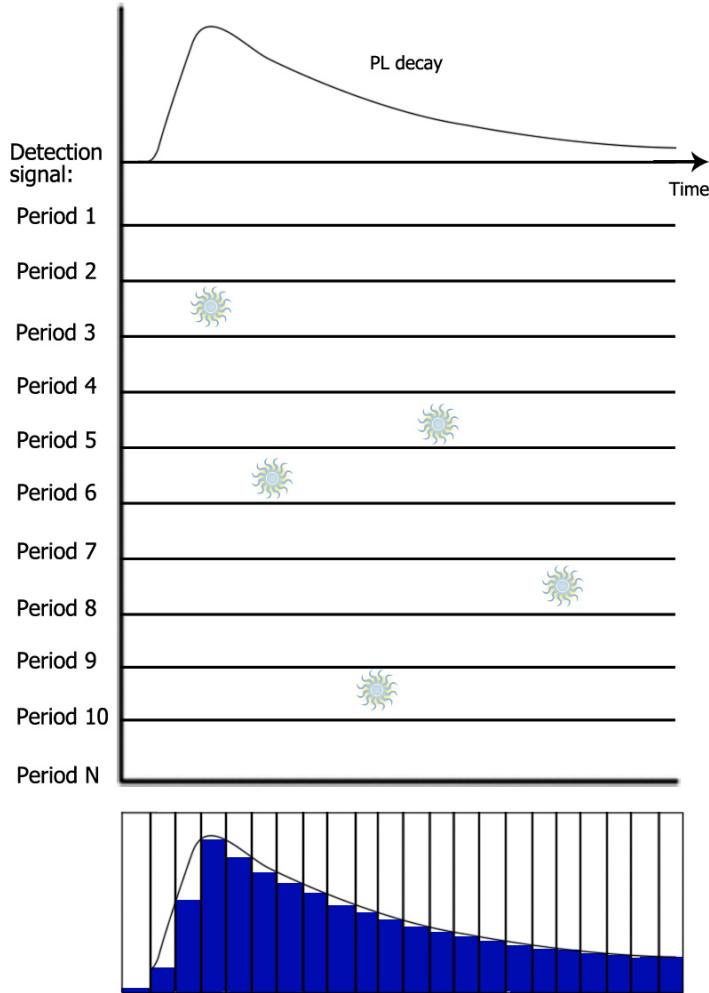


Figure 4.7. Principles of TCSPC method

All these events are collected and presented as a histogram of the arrival times in the final diagram. This interval between arrival times is set as:

$$\Delta t = \frac{1}{f * r} \quad (4.1)$$

where f is the repetition rate of the laser and therefore, measurement period; and $r = 4096$ is the resolution set on the timing card; The

4. Characterization techniques

interval Δt used in this thesis was equal to 98 ps. The time resolution of the experiments can however be limited by the time resolution of the detector or the pulse width of the laser.

In experiments described in this thesis, samples were excited with the same laser as for PL data acquisition: PicoQuant pulsed 405 nm laser diode with 70 ps long train of pulses at repetition rate of 2.5 MHz. However, for some measurements repetition rates up to 40 MHz were used. Repetition rate, i.e. time between pulses, was chosen in the way to allow sample to decay completely before the arrival of the next laser pulse comes. TCSPC module SPC-130 EM with a Si APD was used as a photon detector. In experiments presented in this thesis the resolution of the TRPL setup was limited by the laser pulse width and the APD response time, which was about 200 ps. The setup used for TRPL measurements is the same as shown in Figure 4.2.

4.2.1 TRPL data analysis

Carrier dynamics in both InGaN/GaN QW and in NCs (especially of InP/ZnS) is very complex and not completely understood [78-84]. In this case of the NCs due to decay of excitations via defect states, carrier transfer to the shell surfaces, coupling to ligands, the photoluminescence does not obey simple single-exponent carrier decay dependence which can be described using following equation:

$$I(t) = I_0 \exp(-t/\tau) \quad (4.2)$$

where $I(t)$ shows PL intensity dependence with time, I_0 is the intensity at time zero, τ is corresponding decay time.

However, in real systems, when many possible recombination paths are possible (e.g. for both InGaN/GaN QWs and NCs at room temperature (RT) as well as from different states in NCs and QWs by

4. Characterization techniques

themselves), single-exponential decay law cannot be used and $I(t)$ should be described by more sophisticated models.

NCs demonstrate carrier decay which is rather difficult to fit with a single-exponential decay function [109], [110]. It was proposed to fit such decays using several methods such as log-normal distribution [111], stretched exponential [112], [113] and multi-exponential decay [114], [115]. We have chosen for NCs description the latter method, which gave more precise fitting results. This type of fitting with two or three exponential decay components is widely-used. Analysis based on this method gives good fitting results and allows to get insight into an internal structure of NCs [110], [116]. Care has to be taken when interpreting the results of multi-exponential fitting, because a presence of certain decay time component obtained from fittings indicates only a presence of certain states rather than gives the real values of the recombination times.

InGaN QWs have exhibit some material properties, such as large exciton binding energy, large band-gap, and a wurtzite crystal structure which differentiate them from other semiconductors (such as GaAs or InP). Carrier dynamics is influenced by factors such as strong spontaneous polarization [117] and localization states [118]. Generally InGaN QWs show rather long decay times up to hundred ns [119] and do not show single-exponential decrease with time. It was proposed to fit such decays with the stretched exponential model [118], [120], [121], [122] or multi-exponential model with two [103], [119], [122], [123], [124], [125] or three exponential fitting [126].

Stretched exponential model is described with the following equation:

$$I(t) = I_0 \exp [-(t/\tau)^\beta] \quad (4.3)$$

4. Characterization techniques

where β has the value between 0 and 1. Stretched exponentials have been used to describe carrier dynamics of disordered systems for a long time. In our case the model didn't fit well the decay at very short delay times after the laser pulse. Moreover, in the case of RET in hybrid LEDs with NCs on top another decay component will be added, which can't be well explained by the stretched exponential model. Therefore it was decided to proceed with multi-exponential decay models were used instead. Two-exponential model is described by the following equation:

$$I(t) = A_1 e^{(-t/\tau_1)} + A_2 e^{(-t/\tau_2)} \quad (4.4)$$

where A_1 and A_2 are the weights of fitted decay times τ_1 and τ_2 .

However, for some carrier dynamic processes four-exponential decay models can be used for correct sample analysis, such as for fitting the PL decay of the thin cap samples. This is described in details in chapter 5. In such cases some average decay time τ_{av} may be worth using, which is described as:

$$\tau_{av} = \frac{\sum_i (A_i \cdot \tau_i^2)}{\sum_i (A_i \cdot \tau_i)} \quad (4.5)$$

It should be noted, that multi-exponential decay fitting often approximates real decay, that is why averaged decay time τ_{av} is introduced.

Therefore, for decay time analysis of both NCs and InGaN QWs multi-exponential model is used in this work.

4.3 Current-voltage measurements

One of the most important characteristics of LEDs is a current-voltage (I - V) dependence. I - V characteristics of the devices were

4. Characterization techniques measured using the setup, shown in Figure 4.10, all the data processing was performed in the processor of Keithley SCS with further data-file creation. Like in the EL measurements samples were electrically pumped via metallic probes, using the probe station.

I - V characteristic of a p-n junction is given by:

$$I = I_s \left(\exp\left(\frac{eV}{nkT}\right) - 1 \right) \quad (4.6)$$

where I is the diode current, I_s is the reverse bias saturation current, V is the voltage across the diode, n is the ideality factor, also known as the quality factor or emission coefficient. The ideality factor n typically varies from 1 to 2 (though can in some cases be higher), depending on the fabrication process and semiconductor material of the diode and in many cases is assumed to be approximately equal to 1; k is the Boltzmann constant, T is the absolute temperature of the p-n junction; e is the elementary charge.

In order to simplify equation thermal voltage V_T is introduced, as:

$$V_T = \frac{kT}{e} \quad (4.7)$$

which is constant at $T = 300 \text{ K}$ (temperature close to RT) and equals to 25.85 mV.

From I - V characteristic measurements of the device, its turn-on voltage and influence of parasitic resistances can be derived. The turn-on voltage or threshold voltage V_T is the voltage at which current strongly increases.

Figure 4.8 presents an ideal I - V characteristic and a number of parasitic effects that can affect it.

4. Characterization techniques

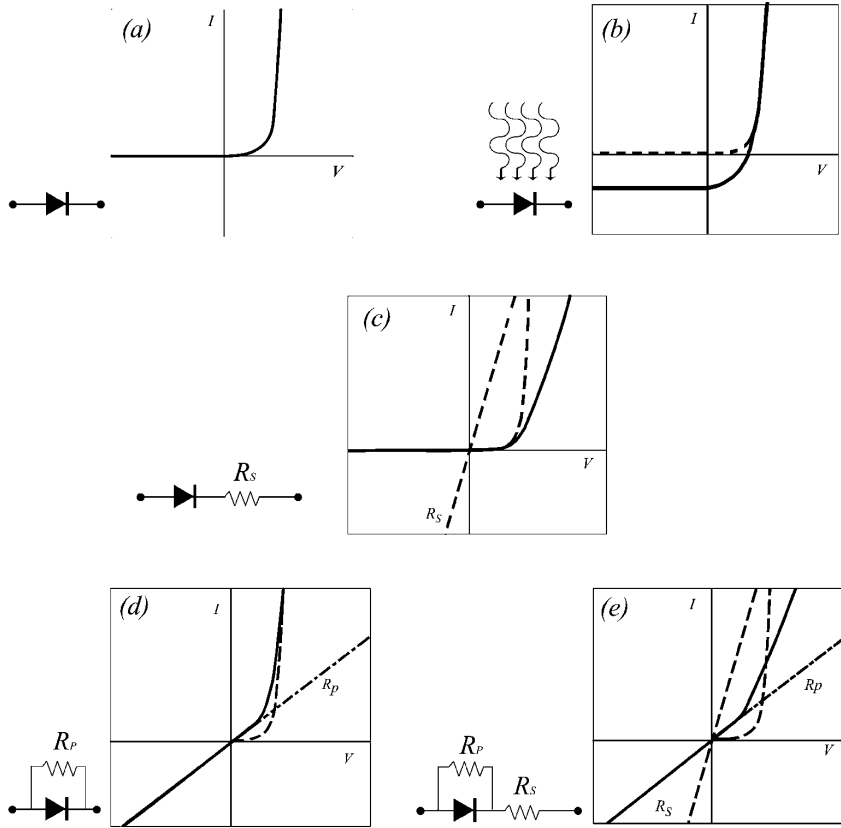


Figure 4.8. Diode's ideal I-V characteristic (a) and influenced by parasitic effects (b-e).

Figure 4.8 (a) shows ideal I-V.

Figure 4.8 (b) shows an effect of a photocurrent. In order to avoid it, measurements have to be carried out in the dark room or sample has to be covered from the ambient light. However, small non-zero currents of around 10^{-10} to 10^{-12} A will appear due to the limited accuracy of the measurement instrument or it may be a leakage current of the circuit.

Figure 4.8 (c) shows influence of parasitic series resistance. It causes a deviation from ideal exponential dependence at higher voltages. Voltages across the diode and resistor add up.

4. Characterization techniques

Figure 4.8 (d) shows influence of parasitic parallel resistance (shunt). In here the effect is best visible at low voltages. Currents through diode and resistor add up.

Figure 4.8 (e) shows influence of both parasitic series and parallel resistances. Effects from both of them add up.

Note, that some additional leakage currents may be non-linear (not represented by a single resistor) and their analysis is less straight forward.

4.4 Electroluminescence measurements

Electroluminescence (EL) is a light emission from a solid-state material, caused by electrical carrier injection. Since white LEDs are electrically-driven devices, EL is a very important measurement technique which needed to be used for full device characterization.

In order to examine electrical properties of devices, a setup to measure electroluminescence as a part of an existing electrical setup was built, which included a multi-fiber mounted on a holder developed by our group at DTU.

EL measurements were performed using a probe station to apply a voltage to the sample with probes placed on the LED contacts. Keithley 4200 semiconductor characterizing system (SCS) (Figure 4.9) was used as a voltage source and ammeter, although being very versatile, it was also used for measurements in the time-domain. Light emission was collected using multi-mode fiber guiding light to the input of the Andor spectrometer and Si CCD camera, that were also used for PL measurements.

4. Characterization techniques

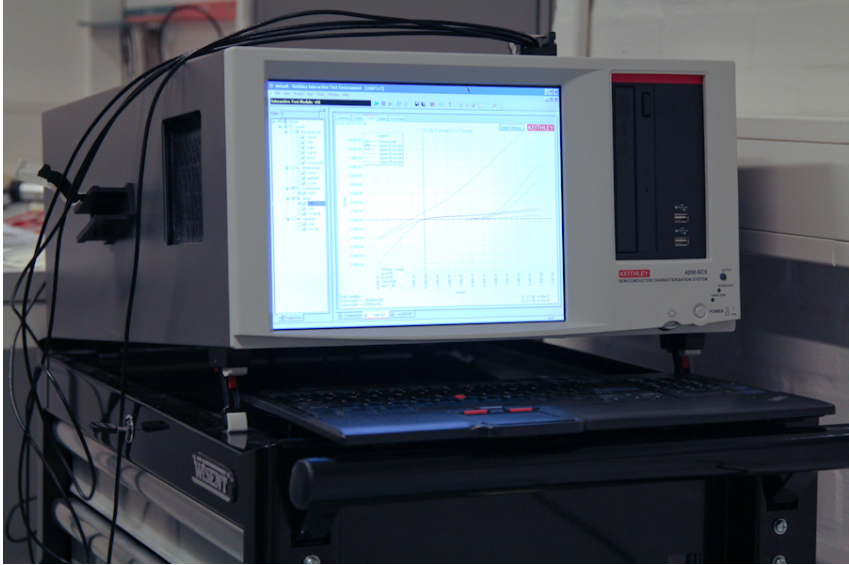


Figure 4.9. Keithley SCS-4200.

Figure 4.10 shows a photograph of the EL setup, used in the experiments. A sample is placed on a metallic sample holder, metallic probes are providing electrical connections. Their positions can be independently and precisely controlled with the help of positioners that allow movement in all three directions. The orange "wire" is the multi-mode fiber, which collects light from the sample and then guides it to the entrance of the spectrometer, where special fiber adaptor is installed in order to in-couple the maximum amount of light.

4. Characterization techniques

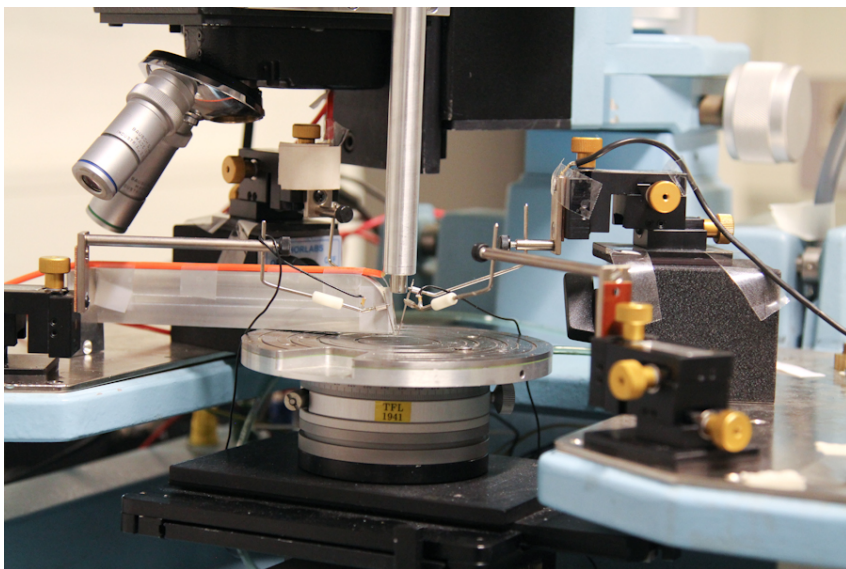


Figure 4.10. An EL setup.

Figure 4.11 presents electrically pumped blue InGaN/GaN LED chip before NCs deposition. In order to show the sample, optic fiber was removed. Keithley power supply was not limiting working voltage, however, maximum current was limited to the value of 0.1 A.

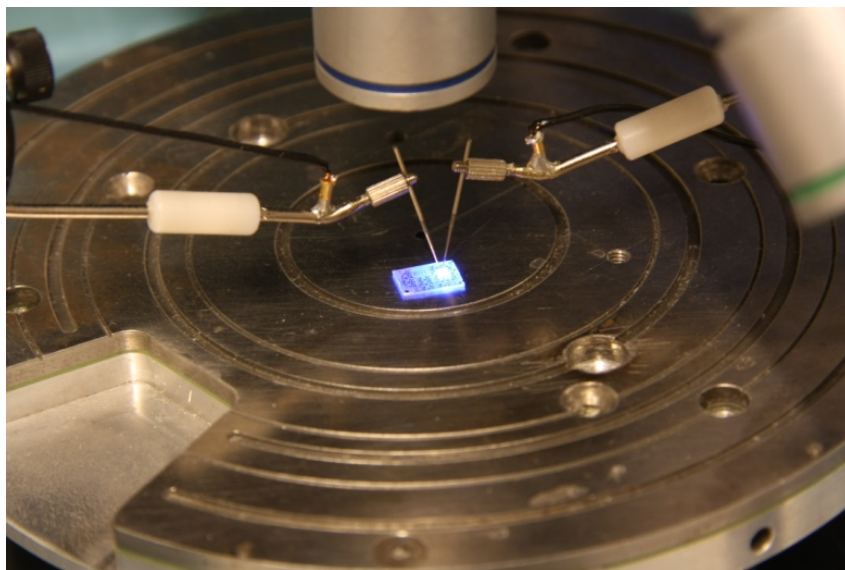


Figure 4.11. An example of the LED with a forward voltage applied to it.

4. Characterization techniques

4.5 Conclusions

In this chapter main characterization techniques used during this PhD work were presented, including PL, micro-PL as well as TRPL measurements and EL and I-V characterization techniques, which allowed devices characterization both optically and electrically, giving access to the full information about the samples. All setups (except the micro-PL which was built by collaborators at DTU Physics) were established during this PhD.

5. Thin cap LEDs

Recent interest in modifying radiative recombination by coupling to surface plasmons [127] or to emitters such as polymers [33] or colloidal nanocrystals (NCs) [15], [34] has led to the development of structures containing quantum wells capped with thin layers of barrier materials [128], which are necessary for the coupling. Due to the relatively weak effect of the surface states compared with the arsenides [129], [130], much of the development has concentrated on the nitride materials. Interest in nitrides has also been driven by the potential applications for SSL. As it was already mentioned in section 2.4, the interactions between the quantum well and the NCs are very sensitive to the cap thickness but also to the character of the excitation in both layers (presence of excitons or binding electron-hole pairs) [131], therefore understanding of carrier dynamics in the QWs itself is important for design of final devices. Much work until now has concentrated on low indium content quantum wells in which carrier localization is not important. Othonos et al. [132] have used samples with 2.5 and 15 nm cap thicknesses emitting at 415 nm and attributed the change in carrier recombination between the wafers to the surface-related states which enhanced non-radiative recombination. Tan et al. [133] used two series of samples with 2.5 and 15nm cap thicknesses, emitting at 390 and 415 nm, and explained the different behavior of thinner cap samples as an influence of strongly localized excitons. These experiments were carried out at room temperature. While all these studies were performed on quantum wells with low indium content, quantum wells with longer emission wavelength in the visible light spectral range are more relevant for the potential applications in SSL. It is known that the increase in the

5. Thin cap LEDs

amount of indium in QWs leads to drastic changes in the material properties and thus recombination of excitons. For example, carrier recombination in InGaN QWs depends strongly on the piezoelectric field induced by strain [104], thickness of the low-temperature grown GaN part of the capping of the quantum well [134], In content and its content fluctuations in the QW [102], which can be affected by the cap thickness.

In this chapter a thin cap LED structure as a platform for hybrid white LEDs based on a RET from the QWs to the NCs is presented, its optical and electrical characteristics and integration with NCs and ligands are discussed. We study the carrier dynamics in InGaN QW emitting in the blue part of the spectral range with thin capping layer and analyze what changes the cap thickness causes. The device structure is shown in section 5.1. Results of the characterization of the samples discussion of the effect of the capping layer thickness on the carrier dynamics of the sample are presented in section 5.2. In further sections of this chapter we study non-radiative energy transfer between InGaN quantum wells and colloidal InP/ZnS nanocrystals. A clear non-radiative energy transfer between the two layers is accompanied by reduced surface recombination in InGaN. This chapter includes materials presented in publications shown in publications list: journal publication #1, 2 and 5; and in the conference proceeding #2.

5.1 Device structure

Thin cap LED structures with various cap thicknesses were grown by collaborators from a group of Professor M. Sopanen from Aalto University, Helsinki, Finland. The sketch of the wafer structure is shown in Figure 5.1.

5. Thin cap LEDs

All epitaxial layers were grown in a vertical flow MOCVD reactor on c-plane sapphire substrates. The precursors were trimethylgallium (TMGa), trimethylindium (TMIn) and ammonia. Disilane was used to introduce n-type doping. The two-step growth method was used for the growth of buffer (2 μm thick un-doped GaN followed by 2 μm thick n-GaN layer) at a temperature of 1030 $^{\circ}\text{C}$. Active layers were grown on top of the buffer at 740 $^{\circ}\text{C}$ in nitrogen ambient to allow incorporation of indium. Growth was interrupted during the temperature ramp at the buffer–active region interface. Reactor was cooled down in nitrogen–ammonia ambient to minimize desorption from the sample surface. The active part of the structure is composed of a superlattice, single QW (SQW) and GaN capping layer. For the sample with 200 nm capping layer, initial 12 nm of the capping layer were grown at 740 $^{\circ}\text{C}$, after which the temperature was ramped up to 940 $^{\circ}\text{C}$ to grow the rest of the capping layer. Lower growth temperature of the initial 12 nm prevents indium desorption from the QW, while higher growth temperature for the rest of the capping layer improves its quality.

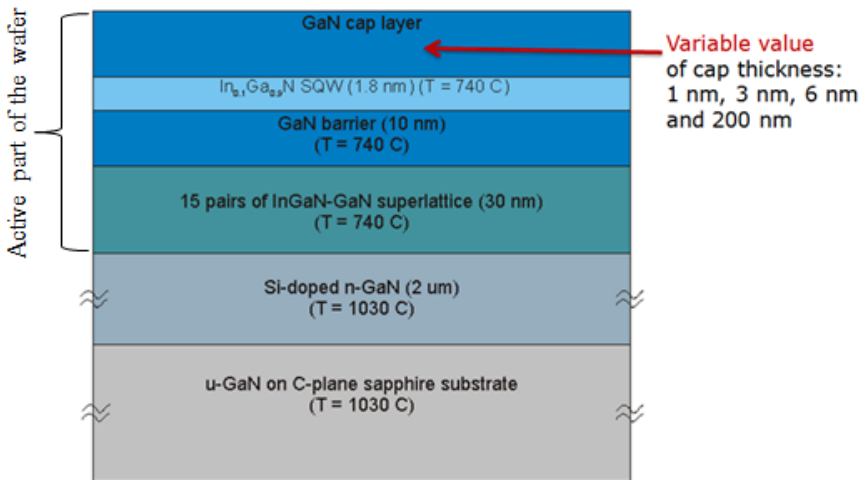


Figure 5.1. A sketch of the epitaxial structure of thin cap samples.

5. Thin cap LEDs

Table 5.1. Comparison of samples with different underneath structures and corresponding indium precursor flow. Optical performance of the thick 200 nm cap samples was characterized with room temperature PL measurements.

Sample	Underneath structure	TMIn flow rate	Normalized RT PL intensity
a	Grown on n-GaN buffer	0 sccm	0.10
b	30 nm of InGaN	2.5 sccm	0.85
c	30 nm of InGaN	5 sccm	0.74
d	15x(1nm/1nm) InGaN/GaN superlattice	10 sccm	1.00

The structure between the buffer and QW was developed specifically to achieve high quality QW. It was done by growing SQWs capped with 200 nm GaN cap with different structures between the buffer layer and the QW. The PL signal from various samples is presented in Table 5.1

It is seen from the table 5.1 that the superlattice underneath the active layer improved PL intensity of the sample, however, the presence of indium and rather high TMIn flows cause rough surface morphology, which may also affect dynamics of thin cap samples [135]. AFM analysis of the wafers' surfaces, performed by the growers, reveals undulations of up to 3 nm in amplitude, which according to the TEM analysis originate from the layers below the quantum wells [135].

$\text{In}_{0.15}\text{Ga}_{0.85}\text{N}/\text{GaN}$ heterostructure QW emitting around 470 nm was used as an active material thus as an energy donor. A set of wafers was used, each with a 1.8 nm thick $\text{In}_{0.15}\text{Ga}_{0.85}\text{N}$ embedded in GaN at different depths below the surface. A sketch of thin cap white LED structure with NCs as light conversion layer is presented in Figure 5.2.

5. Thin cap LEDs

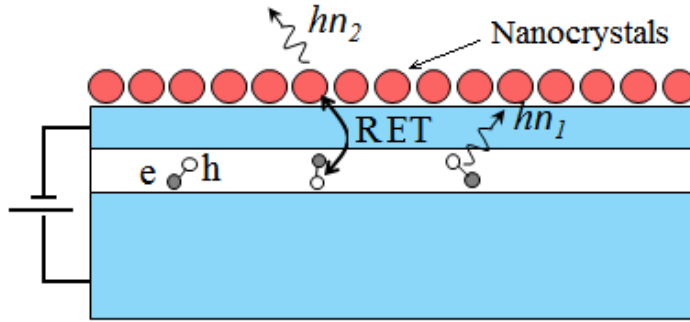


Figure 5.2. A sketch of the thin cap LED structure.

InP/ZnS nanocrystals coated with oleylamine ligands were acquired from NN-Labs [49]. A thin layer of nanocrystals with InP core size of about 4 nm and ZnS shell thickness of about 0.5 nm, emitting at 640 nm, were deposited on top of clean surfaces of wafers by spin coating. Colloidal InP/ZnS nanocrystals were used as energy acceptors, because they are non-toxic and thus compatible with commercial applications. The nanocrystal solution contained excess ligands, in order to ensure complete coating of NCs with the ligands. The combination of the band-gaps of the materials provided a good spectral overlap between emission of the QW and the absorption of the NCs as shown in Figure 5.3.

5. Thin cap LEDs

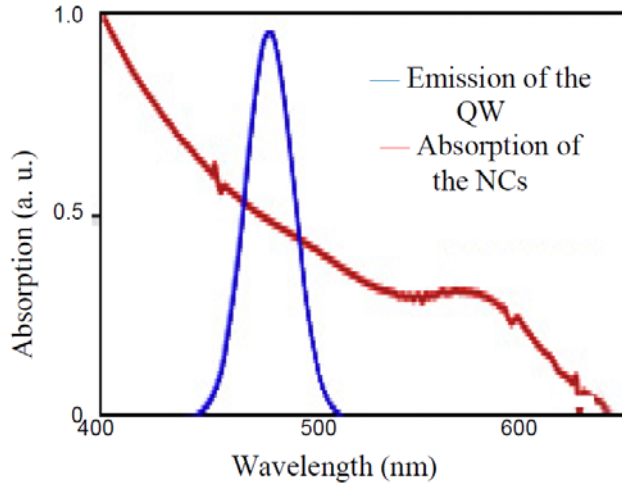


Figure 5.3. Spectral overlap between the emission of the QW and absorption of the NCs.

The InGaN QW wafers were first characterized with a PL mapper. As an example, the PL maps of the 6 nm cap sample are shown in Figure 5.4. It can be seen from the PL maps that the sample has good signal uniformity except the areas close to the edge of the wafer. For the experiments wafer was cut to smaller chips such that the peak intensity and the emission wavelength values are uniform across the chip. The edges of the wafer were not used in the experiments. The same was done for other samples used for analysis in this chapter.

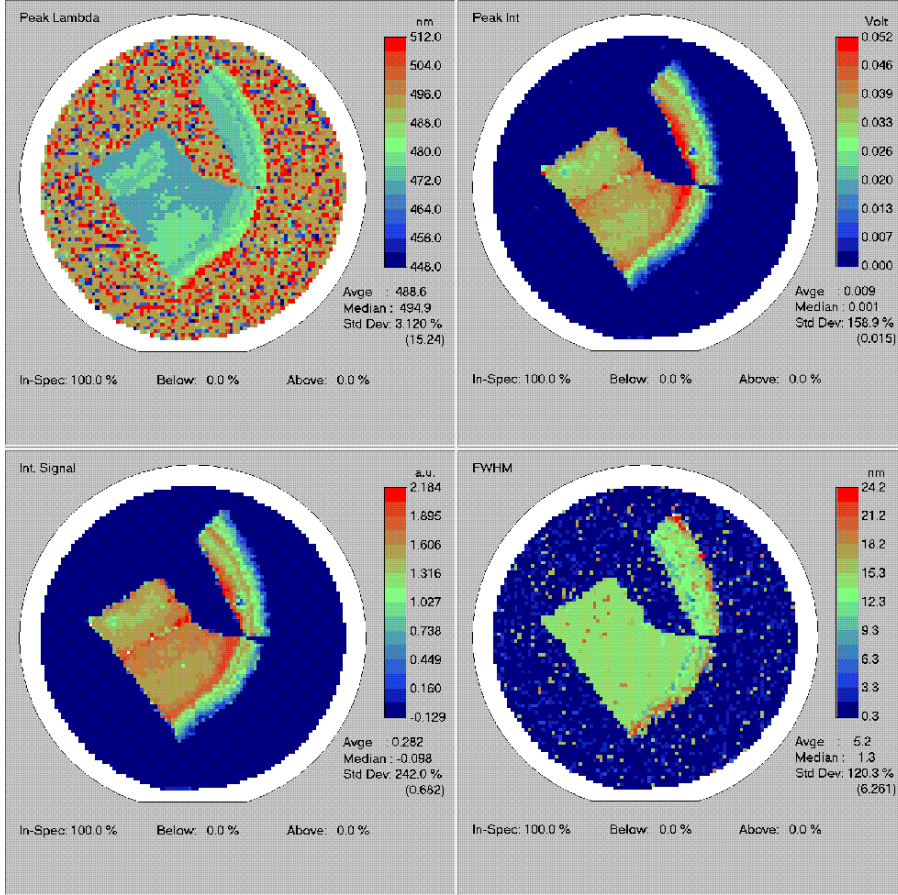


Figure 5.4. PL maps showing peak emission wavelength, integrated PL peak intensity, intensity signal and full width half maximum (FWHM) of the sample with 6 nm capping layer.

5.2 Effect of the capping layer thickness

The effect of GaN capping thickness on the recombination of electron-hole pairs in high indium-content InGaN quantum wells is discussed in this section. We show that reducing the cap thickness to 6 and then 3 nm leads to change of emission wavelength, increased localization and surface recombination. Experimental data is supported

5. Thin cap LEDs

by modeling using a fully coupled piezoelectric model. Modeling was performed by Morten Willatzen and Benny Lassen from DTU Fotonik, Kgs. Lyngby, Denmark and from the University of Southern Denmark, Sonderborg, Denmark, respectively. More detailed information about modeling can be found in Appendix C. The model was developed through numerous discussions to establish physically relevant structure.

5.2.1 Emission wavelength dependence on the cap thickness

Wafers with single QW with 1 nm, 3 nm, 6 nm and 200 nm distances from the surface were investigated.

We believe that sample with 1 nm thick capping layer shows strong coupling between the QW and surface states due to the small cap thickness. Moreover, such thin cap can be easily damaged or removed during processing of the device. Roughness of the sample surface of around 3 nm in amplitude makes analysis of 1 nm cap wafer less pronounced and observed effects more difficult to explain. Therefore, we decided to continue analysis with 3 other samples: having 3, 6 and 200 nm thick capping layers.

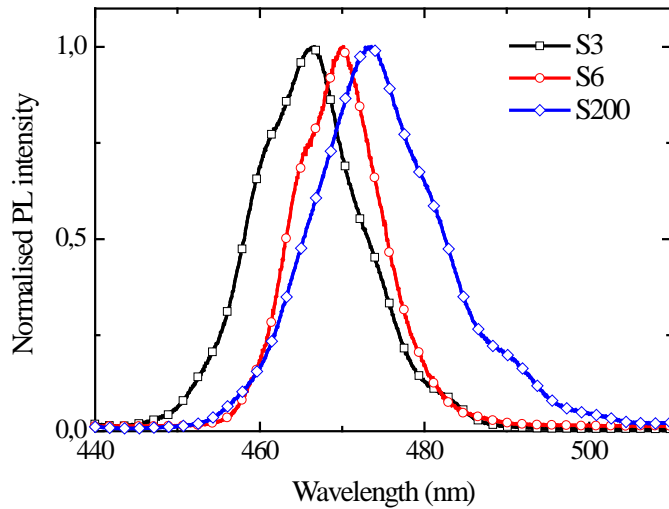


Figure 5.5. Normalized room temperature photoluminescence spectra of wafers with different cap thicknesses.

Normalized PL spectra acquired at 300 K are shown in Figure 5.5. The first thing that can be noticed is the redshift of the peak wavelength with increasing the cap thickness. Emission intensities vary for the samples and the trend in the PL intensity as the cap becomes thinner (which is collected in Table 5.2) suggests that there is an optimal cap thickness of 3 nm in order to get maximum light emission from the sample, at which the cumulative effect of non-radiative carrier losses due to the bulk non-radiative recombination states and the surface states is minimal [133].

Table 5.2. Integrated photoluminescence intensities for the series at room temperature normalized to 1 for 3 nm wafer.

Sample name	S3	S6	S200
Emission intensity, a.u.	1	0.64	0.41

5. Thin cap LEDs

Later in the chapter samples with 3 nm, 6 nm and 200 nm cap samples will be referred to as S3, S6 and S200, respectively. Temperature dependence of the PL measurements of the samples was further performed. Measurements at low temperatures allow probing the samples when non-radiative recombination can be neglected. PL spectra of InGaN/GaN QW measured at 4K upon excitation with the pulsed diode laser are shown in Figure 5.6 and can be seen to consist of the main emission peak and two smaller satellite peaks, which can be attributed to phonon replicas. Unlike at room temperature (RT), the PL signal is the strongest for the sample S200 and the weakest for the sample S3. This trend can originate from either surface state recombination or weaker wavefunctions overlap due to the depletion field and will be further discussed in the section. The systematic change of the main peak wavelength with the cap thickness, although the QWs are nominally the same, reflects an influence of internal piezo- and polarization effects as well as an electric field due to background and surface charges [134]. Figure 5.7 shows the simulated dependence of the emission wavelength on the cap thickness. Red shift is observed with thicker capping layer and the wavelength saturates at around 7 nm. Further increase of the cap thickness has no influence on the emission energy. While the simulations reflect the observed trend very well, calculated emission wavelengths are shorter than the measured ones. This is most likely due to the random growth-to-growth variations of the indium flux during the wafer growth, but possibly also due to the uncertainty of the InN and GaN parameters available in literature as well as can be explained with simplifications in simulations (one band effective mass model can be changed with more precise eight band model).

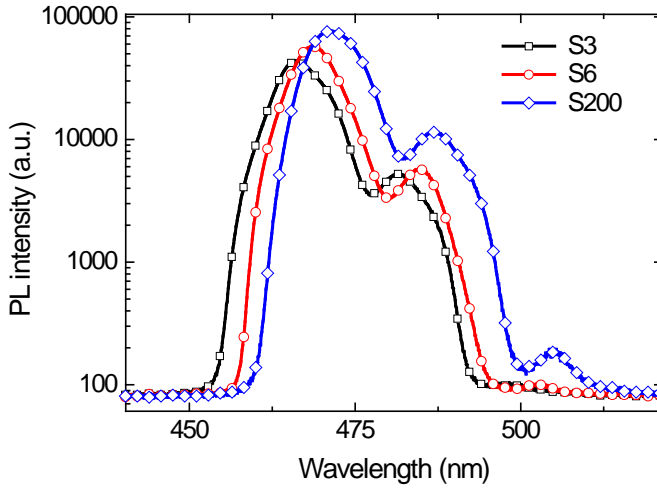


Figure 5.6. PL spectra for samples S3, S6 and S200 at 4K

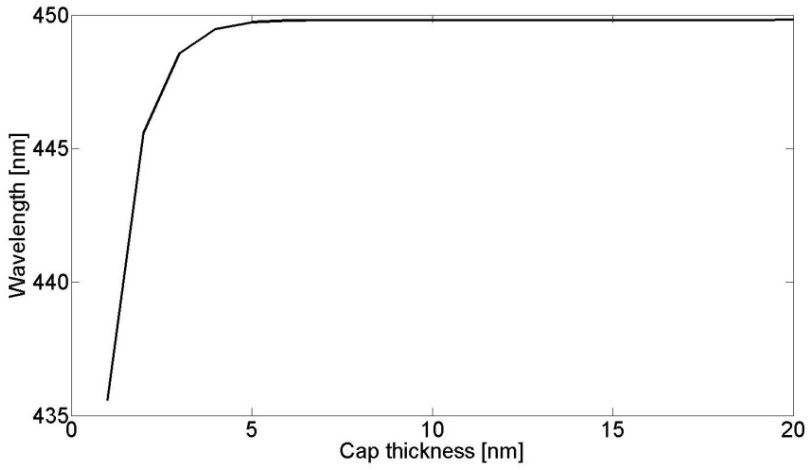


Figure 5.7. Simulated lowest state emission energies for different samples.

5. Thin cap LEDs

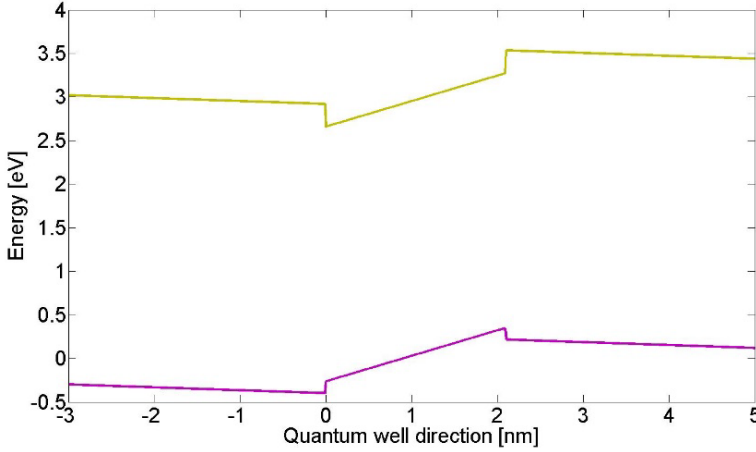


Figure 5.8. The effective valence and conduction band potential for a sample with capping layer thickness of 3 nm.

Figure 5.8 shows effective conduction and valence band potentials for the QW of sample S3. The effective potentials of the GaN barriers (Figure 5.8) are the same for the different capping layer thicknesses, and the difference to the emission energies of samples originates from the effect of the proximity of the surface and its effect on the electron wavefunctions. While the hole wavefunctions and energies do not show a significant dependence on a cap thickness, the lower mass of electrons combined with the potential shown in Figure 5.8 result in a significant penetration on electron wavefunction into the GaN cap. The observed change in emission wavelength with cap thickness is due to this partial delocalization of the electron wavefunctions, resulting in their energy renormalization.

5.2.2 Effect of the cap thickness on the carrier localization

In addition to the different emission energies, Figure 5.6 also shows the phonon replicas, whose presence indicates a high degree of localization in the system. Such LO-phonon sidebands (PSBs) of the PL are related to the degree of electron or hole localization [136], [137], [138]. In direct gap semiconductors carriers with well-defined k number have negligible intensity of the PSBs comparing with the main emission peak. This is a direct result of momentum conservation. Carriers from localized states have non-defined k number and are seen to exhibit stronger emission of PSBs [138]. I. Brener et al. have shown in [137] that weakly localized excitons do not show any PSBs, while tightly localized excitons and separately localized electrons and holes show strong PSBs. Analysis of the strength of localization can be performed using Huang-Rhys (HR) factors. HR factors (S_n) characterize the strength of the coupling between radiative transitions and LO-phonons and are defined from the intensity ratios of phonon replica's peaks:

$$S_n = (n + 1) \times \left(I_{n+1} / I_n \right), \quad (5.1)$$

where n is an index of the phonon replica, I – its intensity, and $n = 0$ corresponds to the main emission peak, the so called zero phonon line (ZPL).

Physical meaning of the HR factor S is the measure of the coupling strength of the radiative transition to the LO-phonon polarization field. S is given by [137], [138]:

$$S = \frac{1}{2\hbar\omega_{LO}^3} \sum_q |D_q|^2, \quad (5.2)$$

where $\hbar\omega_{LO}$ is LO-phonon energy, D_q is proportional to the q th - fourier-transform coefficient of the particle charge distribution, which is

5. Thin cap LEDs

related to the degree of its localization. Localized excitons exhibit strong PSBs due to the fact that their wavefunction contains large q components that allow them to couple to a wide range of LO-phonons [137].

By analyzing HR factors [133], [137], and photoluminescence peak energies, Tan et al. [133] have shown that the number of localized excitons increases with the reduction of the cap thickness in low indium content QW. Since increased level of indium should lead to stronger localization, such QWs will differ from ones, presented in literature, and have to be further analyzed in this thesis.

Information from the first HR factor, S_0 , may be misleading because the ZPL may include emission from delocalized excitons as well as the localized ones, therefore, the factor S_1 should give more precise information about localization [137].

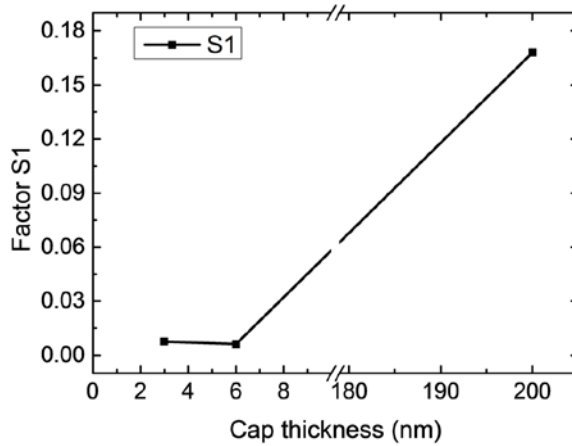


Figure 5.9. S_1 parameter depending on the cap thickness of the samples.

The thin cap samples have smaller values of the factor S_1 (Figure 5.9) indicating stronger localization in these samples, but one has to rule

5. Thin cap LEDs

out a possibility that the observed trend is caused by changes of the depletion/electric fields [133] which would lead to similar dependence.

Another evidence of localization is an S-like shape of the emission peak position versus the temperature, which is shown in Figure 5.10. It has been associated with the presence of localized states (LS) due to inhomogeneities of the potential due to indium segregation regions and probably also due to the influence of defects in the structure [139], [140]. Red-shift is due to the band shrinkage, and blue-shift is attributed to the thermal distribution within the localized states, as localized states are having slightly different energies which results from the change of average indium concentration, spatial fluctuations of indium percentage [141]. S-shape dependence of sample S6 is shown as an example. The other samples' peak energy dependencies from the temperature are similar to this one.

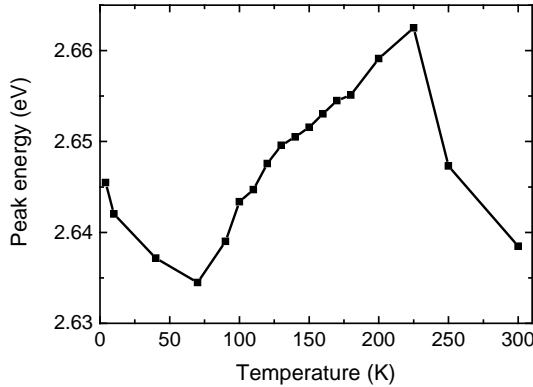


Figure 5.10. S-shape behavior of PL peak position versus temperature, as an example sample S6 is shown. The other samples have shown similar behavior.

5. Thin cap LEDs

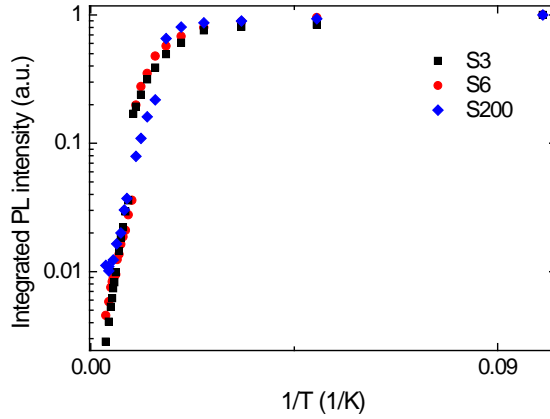


Figure 5.11. Arrhenius plot of integrated PL signal from samples S3, S6 and S200.

We looked at the temperature dependence of the integrated PL, which is shown as an Arrhenius plot for all three samples in Figure 5.11. In attempt to quantify the localization, the data was fitted with a function of the following form:

$$I = \frac{I_0}{1 + A_1 \cdot \exp(-E_{a1}/kT) + A_2 \cdot \exp(-E_{a2}/kT)}, \quad (5.3)$$

where k is the Boltzmann constant, A_1 and A_2 are the probability coefficients, I_0 is the PL intensity at 0K, E_{a1} and E_{a2} are activation energies for non-radiative centers.

Two fitting components reflect two slopes in the curves. Larger activation energy, E_{a1} , which has much stronger weight can be attributed to the depth of LS compared with conduction edge depth, assuming that the radiatively recombining excitons are localized and escape by thermal activation to recombine non-radiatively [20], [141].

5. Thin cap LEDs

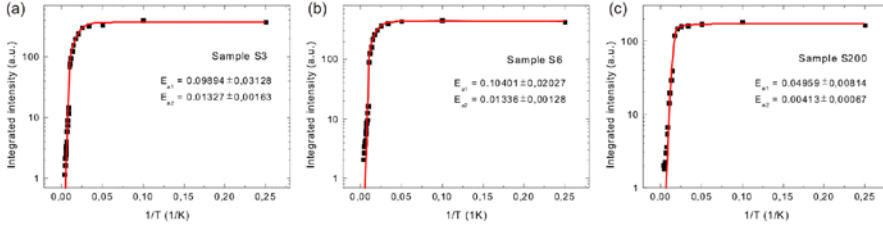


Figure 5.12. Fittings of activation energies for samples S3 (a), S6 (b) and S200 (c).

Fittings of the samples are shown in Figure 5.12. Activation energy E_{a1} was fitted to be 100 meV for samples S3 and S6 and 50 meV for sample S200. Samples S3 and S6 have double localization depth according to these fittings which confirms the stronger localization in the thin cap samples, observed in Figure 5.9. Stronger localization can be caused by surface roughness or surface defects or stronger indium inhomogeneity in the QWs caused by indium reorganization when wafers are cooled down and the GaN cap is thin. At low temperatures (4 to 60 K) a small decrease of intensity is seen with low activation energy, E_{a2} , of 4 and 13 meV for thick (S200) and thin cap (S3 and S6) samples, respectively. It is still not completely clear, what is the origin of such activation energy [142], but it is possibly attributed to the energy difference between different localized state energy bands. Levels with their energies and carrier concentration are shown schematically in Figure 5.13, where E_0 , E_d , E_{loc1} , E_{loc2} , E_{a1} , and E_{a2} are corresponding to the conduction band state, defect states, first and second localization states, first and second activation energies, respectively. Energy separation is not to scale.

5. Thin cap LEDs

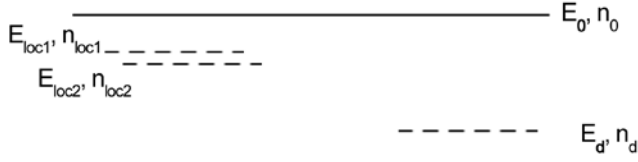


Figure 5.13. A diagram, presenting energy states, where E_0 , E_d , E_{loc1} , E_{loc2} , E_{a1} , and E_{a2} are corresponding to the conduction band state, defect states, first and second localization states, first and second activation energies, respectively.

Energy separation is not to scale. n_0 , n_d , n_{loc1} , n_{loc2} , n_{a1} , and n_{a2} are carrier concentration at respective states.

5.2.3 Change of carrier dynamics with decrease of the cap thickness

Surface states (SS) for thinner cap samples can be responsible for the decrease in PL signal which can be seen in Figure 5.6. Any defects close to or at the surface of the semiconductor promote recombination, or act as carrier traps. Such defects appear because of the broken periodicity of the crystal lattice, which causes dangling bonds at the surface of the wafer. The number of dangling bonds can be decreased by surface passivation, which relies on saturating the dangling bond by attaching them to atoms on the passivation layer.

The origin of the intensity change of thin cap samples, clear from Figure 5.6 is investigated with time-resolved PL (TRPL), using 405 nm pulsed laser, in order to explain the reasons of such behavior looking at the carrier dynamics of the samples. Detailed description of the TRPL setup can be found in section 4.2.

Room temperature TRPL of all three wafers, normalized to 1 at $t = 0$ is shown in Figure 5.14. The decay curves are non-exponential, showing long “tails” after initial decrease of PL intensity.

The decay time is shortest in a 200 nm cap wafer, and as the cap thickness decreases it becomes significantly longer. In InGaN QWs the

5. Thin cap LEDs

non-radiative recombination competes with the radiative recombination at localisation centres [102] and the quenching of the PL intensity (seen in table 5.2) and fast decays prove this fact.

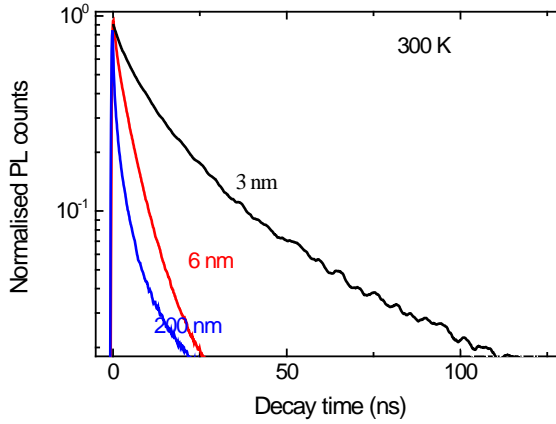


Figure 5.14. TRPL curves for samples S3, S6 and S200, measured at 300 K.

Since the non-radiative recombination in $\text{In}_x\text{Ga}_{1-x}\text{N}$ QWs is thermally activated, as it was shown in Figure 5.11, its relative contribution to the full recombination changes with temperature. As can be seen from Figure 5.15, the photoluminescence decay time increases as the wafers are cooled down from room temperature to 40 K. The change of the initial decay time is the largest in the 200 nm cap wafer and the lowest for 3 nm cap wafers (note the beginning of the decay curve). Fittings of the initial decay time of the samples showed that for sample S200 initial decay value has changed from 2.39 ns to 20 ns, while for S6 and S3 samples initial decay have changed from 4.15 ns to 21 ns and from 9.13 ns to 22 ns, respectively. Under initial decay we imply first decay component of the PL decay curve.

5. Thin cap LEDs

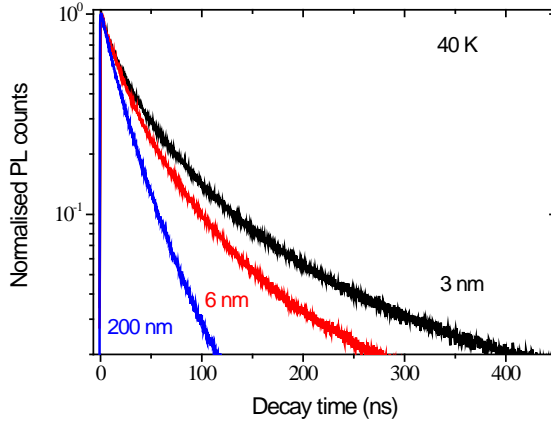


Figure 5.15. TRPL curves for samples S3, S6 and S200, measured at 40 K.

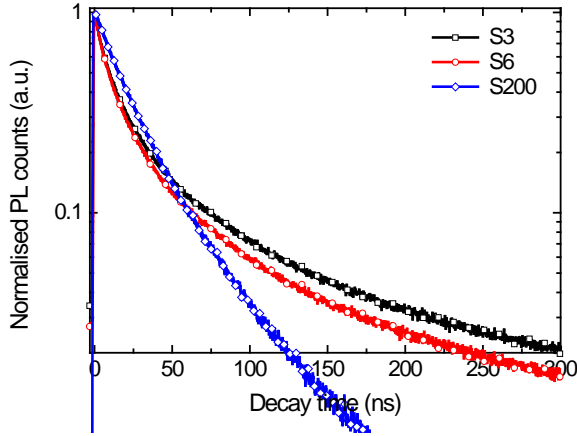


Figure 5.16. TRPL curves for samples S3, S6 and S200, measured at 4 K.

Figure 5.16 shows decay time curves for all samples at 4 K. It is assumed that there is no bulk non-radiative recombination at this temperature [20], [143]. While sample S200 shows a single-exponential decay with a decay rate of 0.045 ns^{-1} ($\tau = 22 \text{ ns}$), the thin cap samples show clear deviation from single-exponential decay. A fast initial decay due to radiative recombination and trapping on the surface states ($t \approx 20 \text{ ns}$) is followed by a long tail due to de-trapping of carriers from the

5. Thin cap LEDs

surface states ($t > 40 - 60$ ns). Proximity of the surface states may also lead to trap formation which can temporarily retain the carriers. Note that, a similar situation is observed in core-shell colloidal nanocrystals in which the surface is also very close to the light emitting core [107].

The initial decay in both thin cap samples is faster than the radiative recombination decay for the sample S200. While the faster initial recombination could be attributed to the stronger electron-hole overlap in the presence of an internal electric field, long emission "tail" cannot. In addition it could not explain lower PL intensity (Figure 5.6). Other explanation for the faster initial decay is fast non-radiative recombination on the SS [132].

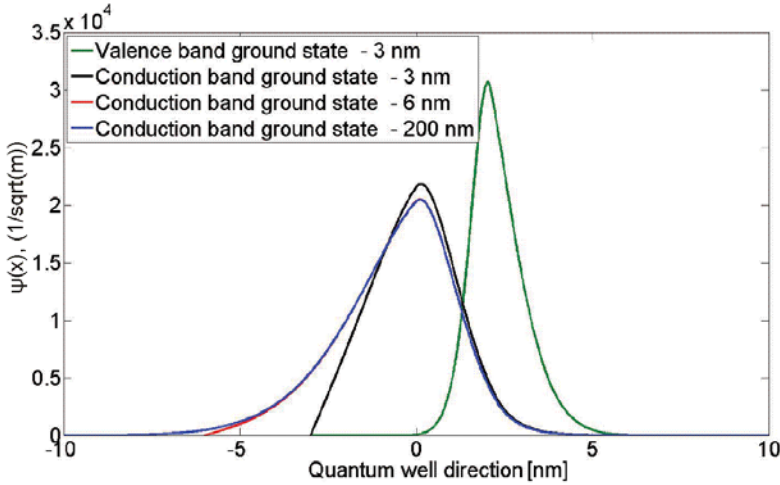


Figure 5.17. Wavefunction of the lowest energy electron state in the S3, S6 and S200 conduction (black, red and blue curves, respectively) and wavefunction of the lowest energy hole state in the quantum well structure (green) which does not depend significantly on capping layer thickness. The well is located between 0 and 2 nm.

5. Thin cap LEDs

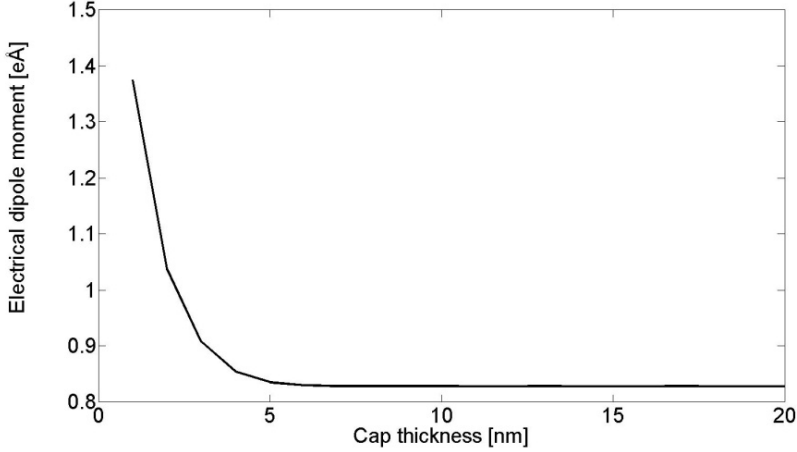


Figure 5.18. Overlap integral between the lowest energy electron state and the lowest energy hole state as a dependence on a cap thickness.

Simulations of electron and hole wavefunctions, results of which are presented in Figure 5.17, show that due to the leakage of electron wavefunction into the capping layer, overlap between electron and hole wavefunctions decreases with the cap thickness as shown in Figure 5.18.

Higher overlap between wavefunctions in thinner cap samples is consistent with faster initial decay times. However, it should also lead to PL emission (Figure 5.6) from S3 and S6 samples being the same or stronger than from S200, which is not the case. Experimentally it was found that initial decay times of both thinner cap samples, fitted from decays presented in Figure 5.16 to be around 6 ns, are much shorter than the single-exponential decay of sample S200 fitted to be around 22 ns. Initial decay times can only be explained by the presence of traps on SS, since at 4 K bulk non-radiative recombination centers are frozen out and integral overlap calculated above does not exhibit such a difference between samples S6 and S200.

Figure 5.19 shows distribution of fitted decay time components with temperature. As an example components of sample S6 are shown. Short component (τ_{NR}) is a well-known thermally activated non-

5. Thin cap LEDs

radiative recombination, which becomes negligibly low below 80K. Long tails are associated with recombination of carriers trapped on the SS. They are getting extremely long at low temperatures. Other components are radiative recombination. The extracted decay times only reflect complex carrier dynamics and cannot be associated directly with any process. Fitting with one less or one more components will change values of fitted decay times.

Such multi-exponential PL decay can be better described with the averaged decay time, defined as:

$$\tau_{av} = \frac{\sum_i (A_i * \tau_i^2)}{\sum_i (A_i * \tau_i)}, \quad (5.4)$$

where τ_i and A_i are decay components and their weights, respectively.

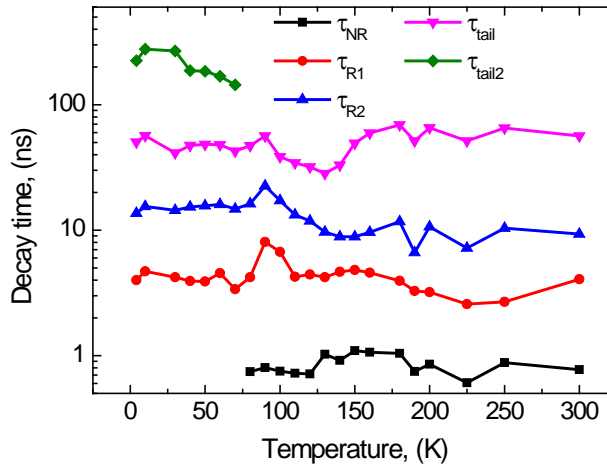


Figure 5.19. The decay time components of the sample S6 versus temperature.

5. Thin cap LEDs

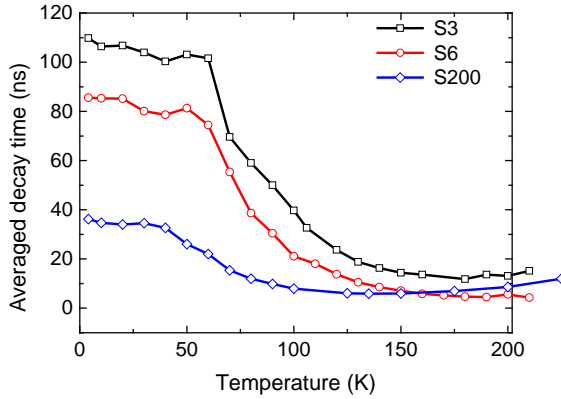


Figure 5.20. Averaged decay time temperature dependence.

Samples S3 and S6 were fitted with 4 components, while sample S200 was fitted with 3 components at higher temperatures (it didn't have long tails) and with 2 components at temperatures below 50 K (when non-radiative component became negligible). This number of components for fittings allowed good overlap of the fitted and experimental curves.

Figure 5.20 shows an evolution of the average decay time with temperature for all wafers. With decreasing the temperature averaged decay time value starting to grow as earlier as the thinner is the sample. A possible explanation for the averaged decay time increase could be decreased role of the non-radiative recombination or more effective radiative recombination of the excitons in the localisation centres [102]. It finally saturates at around 40 K for sample S200 and at around 50-60 K for thinner cap samples S3 and S6, when non-radiative recombination centers are frozen and are negligible. This saturation temperature is different for the samples. Before this temperature there is a steep slope of the averaged decay times, where while temperature increases decay time value decreases rapidly. It was shown by Minsky et al. [102] that for larger localization radiative decay time component

5. Thin cap LEDs

decreases at higher temperatures. The same is seen for our samples, so sample S3 has larger localization and sample S200 the lowest. Therefore, the stronger localization with reducing capping layer thickness has to be considered.

Much larger values of τ_{av} for thin cap samples S3 and S6 can be supported by the effect of SS, as it was mentioned above. Such SS work as traps that are able to capture carriers and then release, allowing recombination to occur afterwards with much longer times than the ones that were not trapped. Therefore, thin cap samples exhibit charge transfer to the SS and it gets larger with thinner capping layer. This charge transfer process will compete with the non-radiative energy transfer process if RET [131] is to be studied.

5.3 Effect of nanocrystals and influence of ligands

Non-radiative resonant energy transfer from the QW to the NCs results in additional recombination channel in carrier dynamics. As RET doesn't require photon emission, energy is transferred via dipole-dipole interaction, this process is rather fast, in order of hundreds picoseconds. Therefore, carrier dynamics of the QW exhibiting such energy transfer to the NCs would show faster decay times or increased decay rate k (as $k = 1/\tau$). Measured difference in decay rates of the QW before and after deposition of NCs would suggest existence of non-radiative energy transfer.

Figure 5.21 shows decay time curves measured at room temperature for QWs covered with 3 and 6 nm GaN capping layers, both before and after NCs layer deposition. For analysis of PL decay curves we fitted the

5. Thin cap LEDs

initial time (shown in the figure). The sample with 3 nm GaN cap above the QW (7 nm distance between centers of the QW and NCs) shows faster decay rates after NCs deposition, which is consistent with the presence of RET. RET rate calculated as a difference between decay rates measured with and without NCs is 0.02 ns^{-1} . Fitted decay times were 8.59 and 9.91 ns for samples with and without NCs, respectively, which corresponds to rates of 0.12 and 0.1 ns^{-1} . Sample with 6 nm GaN, showed slower decay rate by 0.05 ns^{-1} after NCs were deposited on its surface (7.35 and 5.25 ns for samples with and without NCs, respectively, which corresponds to rates of 0.14 and 0.19 ns^{-1}). Sample with 200 nm thick cap didn't show decay rate change after NCs deposition.

The slower decay rate seen in the 6 nm cap sample clearly cannot be related to RET but may be associated with decrease of recombination on SS. Since the NCs solution contains excess ligands (free ligands not bound to NCs) promoting stable coverage of the NCs with ligands, NCs deposition may be accompanied by the attachment of ligands to the clean surface of GaN. One possible explanation of the increased decay time in the wafer with 6 nm GaN cap is the passivation of the surface states by these organic ligands, that counteract RET [34].

To confirm this observation another sample was prepared and measured. Thin layer of oleylamine ligands was spin-coated on top of clean thin cap wafer. Measurements of the decay rate of the carriers' dynamics in QWs has showed slower decay rate than that of the bare wafer, as shown in Figure 5.22. This confirms that ligands act as surface passivation of the etched InGaN/GaN QWs.

As a conclusion of this section, nanocrystals in the solution with organic ligands after deposition on top of the thin cap sample in close proximity to the QW can cause two processes: RET and surface

5. Thin cap LEDs

passivation. Effect of these processes on carrier dynamics is opposite, RET makes it faster and passivation removes fast non-radiative decay channels, thus increasing total decay time. Therefore, one should be careful analyzing samples with NCs containing ligands, and take into account passivation effects.

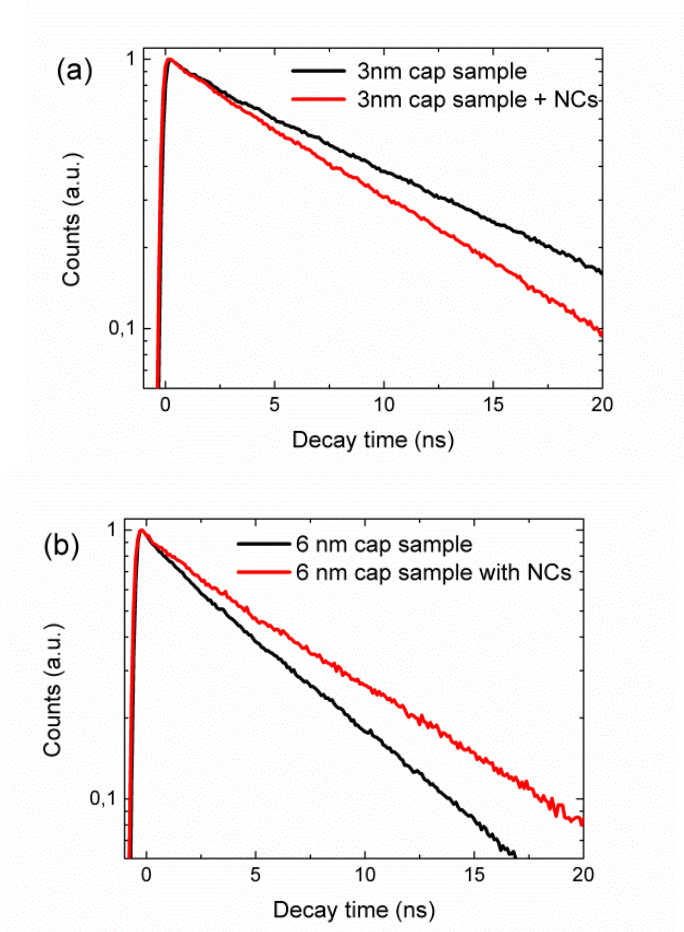


Figure 5.21. Effect of NCs deposition on PL decay of the QW with (a) 3 nm and (b) 6 nm GaN capping layer.

5. Thin cap LEDs

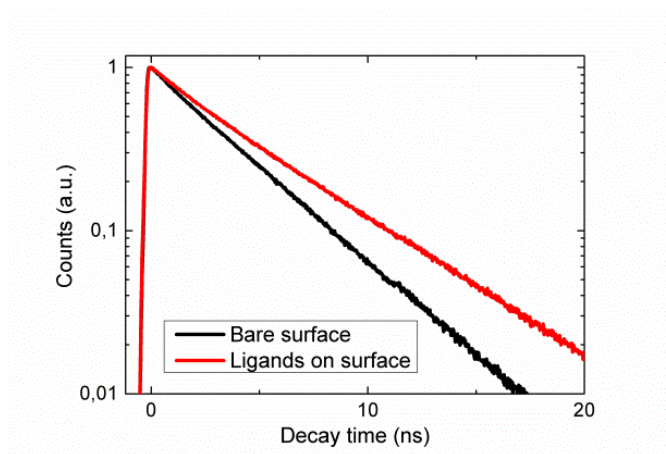


Figure 5.22. Effect of ligands deposition on the surface of the thin cap sample.

5.4 Electrical characterization of the diodes

Commercial LEDs used in different applications are electrically-driven rather than optically. Therefore, electrical characterization is necessary and more important for the customer than optical one. Devices with the thin capping layer used in this thesis were characterized electrically.

Electrical measurements have been performed on LED structures with thin capping layer. The wafer structure consisted of the n-type GaN followed by 1.8 nm InGaN QW emitting at 470 nm and covered with 3 nm p-GaN. Note that in order to achieve RET the additional layers such as AlGaIn electron-blocking layer, present in high-brightness LEDs, were not used.

Figure 5.23 shows IV characteristic of the sample from this wafer with NCs deposited on the top. At low voltages, current is flowing via defect states as can be seen from excessive current below the expected threshold voltage of about 2.7-3 V. This current was measured both with and without NCs and if the measurement was repeated a few times, the

5. Thin cap LEDs

sub-threshold current would increase until eventual breakdown. In even more extreme cases, the sample did not produce any light under electrical excitation and showed linear IV characteristics. This points the problem with such devices, namely a diffusion of the annealed p-type contact metals inside the structure that can shunt the p-n junction. For the thin cap samples, where the separation between p- and n-contact areas is very small, is very important to avoid such diffusion.

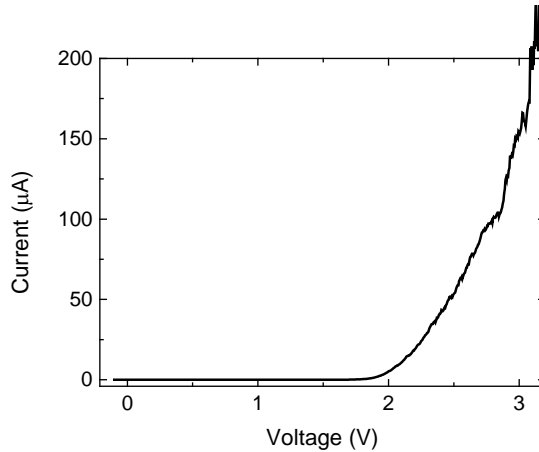
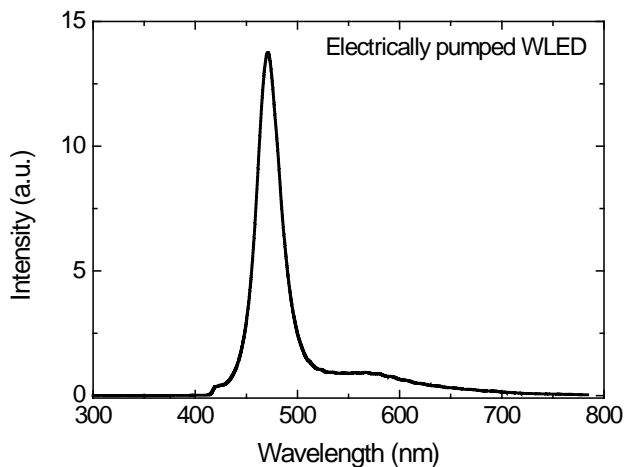


Figure 5.23. A typical IV characteristic of the thin cap sample before breakdown.



5. Thin cap LEDs

Figure 5.24. EL of the thin cap sample with NCs deposited on its surface.

During EL measurements samples exhibited strong emission from the defect state in yellow spectral range. It was especially visible at low currents, when most of carriers were trapped by the surface or p-type layer defect states.

NCs deposited on top of the electrically-driven sample with thin capping layer didn't emit enough red light to achieve white color after mixing of this red with the blue emission from the QW, as shown in Figure 5.24. We believe this was due to several reasons: the absorption of the NCs at LED emission wavelength is half of the absorption at laser emission wavelength (see Figure 5.3), the LED wafer is not perfect due to the low temperature capping layer growth and quite probable and easy way for carriers was to recombine via surface states or defect states in the crystal.

Based on results of the measurements of this wafer, it is clear that a different device structure is needed. The next device to study was a patterned, regular LED structure, which is the subject of the next chapter.

5.5 Conclusions

In this chapter a hybrid device composed of the LED with QW close to the surface with NCs has been considered. Particular attention was paid to the design of GaN/InGaN QW wafer. Both optical and electrical properties of the wafers and hybrid devices were studied.

It was shown that multiple processes, such as non-radiative recombination on surface states and/or carrier trapping on surface states, recombination from localized states are important and affect carrier

5. Thin cap LEDs

dynamics and PL from quantum wells positioned near the surface. Internal piezoelectric field and spontaneous polarization as well as effect of surface charges caused PL peak position shift and affected the carrier dynamics, making radiative recombination in samples S3 and S6 faster. At the same time leakage of electron wavefunction into the capping layer meant that recombination and trapping on SS are very important resulting in long “tails” in TRPL decay curves.

We have found that the degree of carrier localization in nominally identical InGaN quantum wells positioned at different distances from the surface increases as the distance between the QW and the wafer surface is reduced. This was shown by a larger activation energy for the thinner cap wafers and higher value of so called saturation temperature, when further increase of the temperature leads to rapid decrease of the averaged decay time.

When using NCs for wavelength conversion of excitation from GaN/InGaN QW by non-radiative energy transfer, clear signature of RET was observed, yet the recombination on SS competed with RET, making the hybrid devices less efficient. However, it can be prevented by an efficient surface passivation, as it was observed on the example of surface passivation with organic ligands. Effect of ligands on the carrier dynamics makes the quantitative analysis of the transfer rate difficult. With the appropriate choice of passivation layers, hybrid structures are thus more efficient light emitters.

Although optical characteristics of devices were satisfactory, excitation of NCs from electroluminescence from the LEDs with thin p-type GaN cap over the QW resulted in very weak emission of red light from the NCs. In addition, light emission from defect states in p-GaN in yellow spectral range was observed. The recombination on these states at low currents was dominant, and it was still competing with radiative

5. Thin cap LEDs

processes at higher currents. The yield of LEDs from wafers with thin p-type cap was very low due to difficulties in contacting of the p-layer without shunting the p-n junction.

6. Patterned LEDs.

In contrast to the previous chapter where a small distance between the QWs and NCs was achieved by an epitaxial growth of thin nm-size capping layer above the QW, patterning of a standard LED wafer with holes is employed in this chapter. The etching of the hole pattern must at least reach the QWs, so the NCs on the sidewalls are in a close proximity to them. A patterned LED device structure is described in more details in section 6.1. A white LED both optical and electrical characterization is presented in section 6.2. The RET is discussed in section 6.3. This chapter includes materials presented in publications shown in publications list: a journal publication #6 and a conference proceeding #1.

Although an extra decay channel in the QW emission [10], [128], identified as RET, has been observed in hybrid QW-NC structures, the surface state recombination of the QW excitations, that has a large impact on the decay dynamics, has been widely neglected with only a few exceptions [144]. The carrier dynamics of the QW is influence by the surface states and they are of particular importance in the case of small separations between the surface and the QW. However, covering the surface with the NCs solution may change surface states. In this section we demonstrate a room temperature non-radiative energy transfer from InGaN/GaN quantum wells to colloidal CdSe/ZnS nanocrystals emitting around 440 nm and 620 nm, respectively, suitable for solid-state lighting. In addition, we address the surface state assisted non-radiative recombination of the QW energy donors modified by the alumina passivation thickness. This is in contrast to previous work [10],

6. Patterned LEDs.

[128], [144], where either non-radiative energy transfer has not been unambiguously demonstrated or it has been shown on devices operating in the near-infrared spectral region, which are not suitable for solid state lighting applications.

6.1 Device structure and fabrication

In order to fabricate hybrid white LEDs we used a standard blue GaN/InGaN LED with an emission peak wavelength of 440 nm and both InP/ZnS and CdSe/ZnS core/shell colloidal quantum dots (for simplicity – nanocrystals) with a strong absorption at the emission wavelength of the blue LED, and emitting in the yellow-red wavelength range. The NCs can be excited optically from the QW either via absorption or via non-radiative RET [12], [15], [38], [70].

Samples used in the experiments presented in this chapter were fabricated from a standard bright LED wafer containing 9 InGaN quantum wells (QWs) grown using metalorganic vapor phase epitaxy. The InGaN QW photoluminescence maximum is at a wavelength of around 470 nm. The QWs are 2.7 nm thick and separated by approximately 12 nm thick GaN barrier layers, as shown on the scanning transmission electron microscope (STEM) images in Figure 6.1 (a) and (b).

6. Patterned LEDs.

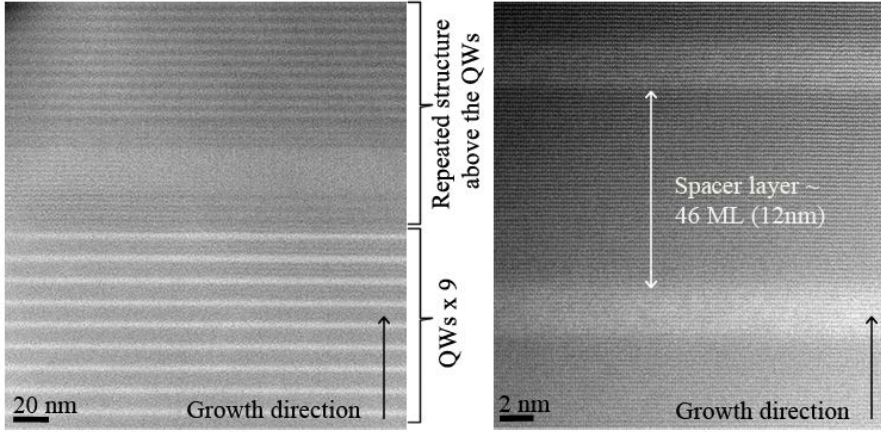


Figure 6.1. STEM images of the wafer: (a) full structure and (b) quantum wells. Images were taken by Dr. Shima Kadkhodazadeh.

Figure 6.1 (a) shows all 9 QWs and a top p-type contact layer consisting from an AlGaIn/GaN superlattice with a total thickness of approximately 200 nm. Figure 6.1 (b) shows two InGaIn QWs and GaIn spacer layer between them. High quality of the wafers is clear from the images. The interfaces between QWs and the barriers are straight and very smooth, with the top interface a little less abrupt, suggestive of more gradual transition between the layers.

Before device processing, a 2 inch LED wafer has been cut into chips with the size of 7 by 7 mm each. A quick qualitative measurement of the chip was performed using the PL mapper. Results are shown in Figure 6.2. The signal from the sample is a square inside the circle. Good uniformity of the sample is seen in the three images of emission peak wavelength, FWHM and PL intensity distribution on the chip.

6. Patterned LEDs.

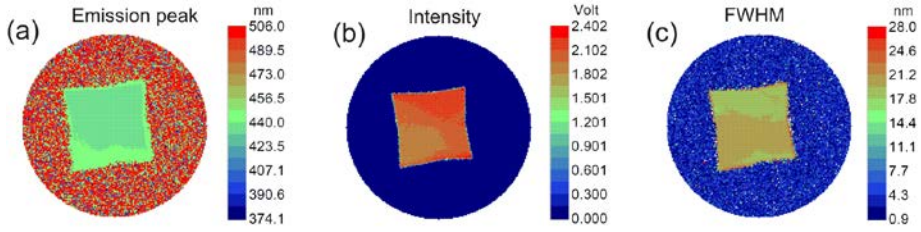


Figure 6.2. Emission peak wavelength (a), PL intensity (b), and FWHM (c) of the unprocessed LED chip, obtained from PL mapper.

Our samples were patterned using optical lithography and a SiO_2 as a hard mask. Mesas with diameters of $300\ \mu\text{m}$ were formed in order to define diode dimensions and provide p- and n-GaN contact access. Hole pattern was introduced at this step to provide contact area with the NCs. Etching of the mesas and hole pattern was performed using an inductively coupled plasma (ICP) etcher with Ar/Cl_2 chemistry. The hole diameter is $1\ \mu\text{m}$ and the depth is $0.4\ \mu\text{m}$, which is sufficiently deep to etch through the QWs into the n-type GaN contact layer. Wet chemical etching in HF for 2 minutes to remove a hard mask followed by etching in 37% HCl for 60 minutes to remove the layer of material damaged by the ICP-RIE was used. For electrically driven devices, contacts to the p-type layer were formed by evaporation of Ni/Au followed by thermal annealing for 30 minutes at $610\ ^\circ\text{C}$ in order to activate the Mg dopants. For the n-type contact, a Ti/Al/Ti/Au metal combination was used. Finally, after both contacts were fabricated and tested, the devices were packaged and wire bonded to simplify the electrical measurements. In the final step, the NCs, diluted in toluene, were deposited by spin-coating. A homogeneous layers of NCs, that covered the devices conformally (including the areas patterned with holes) was obtained after the conditions of the process were optimized. As the diameter of NCs (including the ligands) is around 7-8 nm, they easily penetrate into the patterned holes. Detailed fabrication process is

6. Patterned LEDs.

discussed in Chapter 3 a full set of process recipes is included in the Appendix A.

The images in Figure 6.3 illustrate the geometry of the holes etched to bring NCs into the close proximity of the quantum well. A large part of the mesa top, shown in yellow in Figure 6.3 (a), is covered by a metal contact (needed for bonding). A semicircular free surface of GaN surrounded by the metal contains a rectangular array of holes (shown in grey in the figure), while the rest of the surface is left unpatterned (shown in green) to aid comparison between patterned and unpatterned areas of the device.

While Figure 6.3 (a) shows a magnified optical microscope's image of the pattern, Figure 6.3 (b) presents a micrograph taken with a scanning electron microscope (SEM). Such images were used to assess the quality of the patterning and to measure the holes sizes. The diameter of the holes shown in Figure 6.3 (b) has been measured to be $1\text{ }\mu\text{m}$ and the pitch of the array to be $2\text{ }\mu\text{m}$. Two different sizes of the pattern were used: the first with hole diameters of $1\text{ }\mu\text{m}$ and $2\text{ }\mu\text{m}$ pitch of the array and the second with $1.5\text{ }\mu\text{m}$ wide holes and $3\text{ }\mu\text{m}$ pitch of the array.

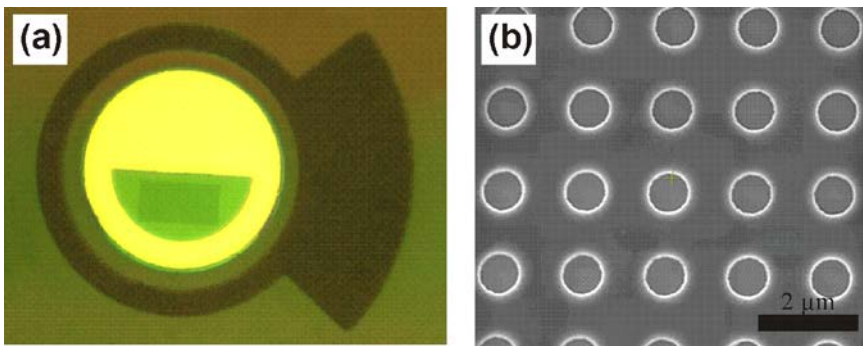


Figure 6.3. (a) Mesa view from the top. Yellow – top contact to p-GaN, grey rectangle on green semicircle – patterned area of free GaN surface, green area – GaN surface on the mesa, dark brown is a bottom contact to n-GaN, (b) SEM image of the holes in the patterned area of the device.

6. Patterned LEDs.

A sketch of the device cross-section is presented in Figure 6.4. Blue circles show approximate size of the blue laser spot compared to the size of the holes. NCs and other layers are drawn not up to scale. The figure shows that NCs (sizes not to scale) are placed in the close proximity to the QWs inside openings etched through the QWs. In this device design, the nanocrystals that can be excited with RET decorate the sides of the holes, and are in contact with the sides of the QWs. The contact area is thus smaller than in the case of thin cap wafers and not only electron-hole generation in the QWs but also carriers' diffusion need to be considered in the device performance analysis.

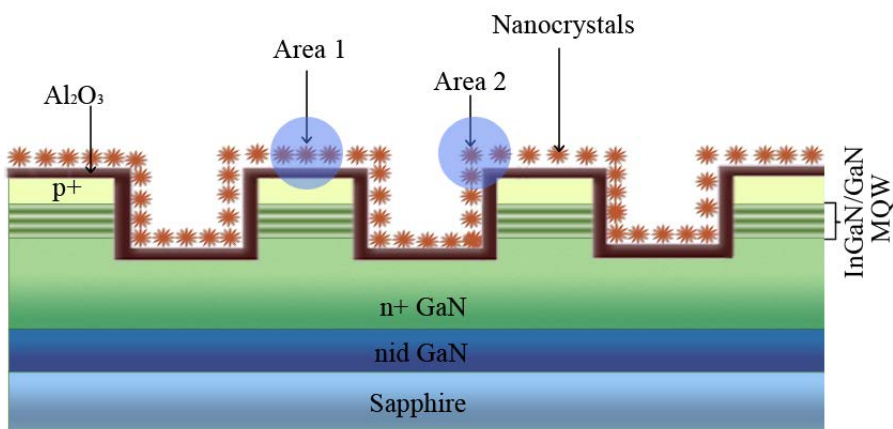


Figure 6.4. A sketch of the patterned LED structure in cross-section.

While initial experiments were performed using InP/ZnS nanocrystals, it became apparent that charge trapping and subsequent Auger recombination [116] were limiting device performance. In experiment, described in this chapter, CdSe/ZnS NCs were used instead of InP/ZnS. Absorption and emission spectra of the CdSe/ZnS NCs used in the studied devices are presented in Figure 6.5.

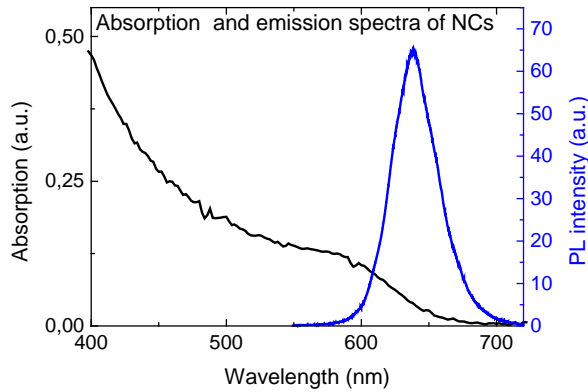


Figure 6.5. An absorption and emission spectra of the CdSe/ZnS NCs used in the studied devices.

6.2 White LED characterization

Photoluminescence (PL) measurement obtained with a 405 nm pump laser is presented in Figure 6.6. This sample has InP/ZnS NCs deposited inside holes in the patterned area. Good color mixing results for the patterned devices are shown. The color rendering index (CRI) has a reasonable value of 73 and CCT of 6190 K (values were calculated using the SpecWin software from “Instrument System” company, supplied with the spectrometer), which supports the assumption that good quality white light can be obtained from hybrid white LEDs where NCs will substitute phosphor. Note that higher CRI index would be obtained if the NCs of different sizes, thus different emission wavelengths, were used to extend the emission beyond 600 nm wavelength. It should be mentioned, that the data was taken with a 420 nm long-pass filter needed to remove the signal from the excitation laser beam resulting in an abrupt cut-off of the luminescence for shorter wavelengths.

6. Patterned LEDs.

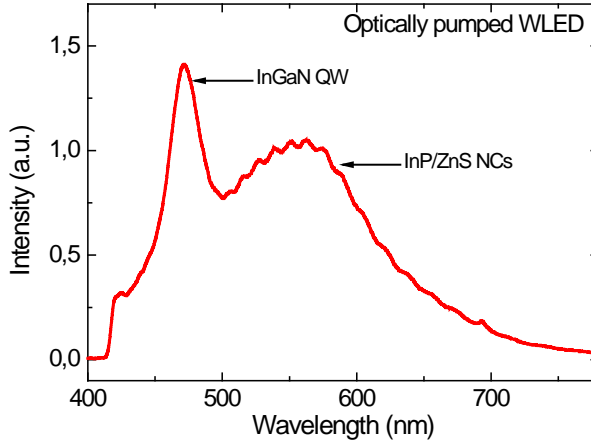


Figure 6.6. Spectrum of an optically pumped white LED.

As the laser beam size used in this experiment was rather large (around 100 μm in diameter) it was not possible to establish the role of RET in the total emission. In order to see the effect of patterning and since the interactions between the NCs and the QWs take place on the etched surfaces of the openings, we performed spatially resolved photoluminescence. Spatially- and time-resolved PL (TRPL) measurements discussed further in section 6.3 are particularly suitable for establishing the presence of RET between the QW and the NCs.

EL measurements performed on this sample didn't show red emission from the NCs. We attribute it partly to low absorption coefficient for the InP/ZnS NCs at the emission wavelength of the LED and partly to the charge trapping and subsequent Auger recombination that were limiting the performance of NCs [116]. Optically driven diodes don't suffer from these problems that much. NCs have higher absorption coefficient for emission wavelength of the laser. Moreover, intensity of the laser emission is high enough to overcome charge trapping and other non-radiative processes in the NCs and supply

6. Patterned LEDs.

enough carriers for the radiative recombination. More importantly, if the device is excited with a pulsed laser with the period longer than the decay rate of carriers in both QW and NCs, the ratio of emission between the two is defined by the ratio of the absorption probabilities and the quantum yield of QW and NCs. Under electrical excitation (which is CW) the number of photons emitted by the QW is defined by the current, while number of photons emitted by the NC is defined by the absorption of QW emission by NCs at low excitation levels and by the decay time of the carriers in QW and NC at the intermediate excitation level. At low excitation level the number of photons emitted by the NCs will increase linearly with the current through the LED and the intensity ratio should reflect the absorption probability. At the intermediate excitation level, when there is a high chance of photon absorption during the exciton lifetime, Auger recombination will start limiting the number of photons emitted by the NCs. Finally, at very high excitation levels, the number of red photons emitted by the NCs will be defined by the number of the NCs and the lifetime of the exciton (~20 ns) and will be current independent. The decay time of the QW is of the order of 4 ns and decay time of NCs is of the order of 13 ns. Auger recombination tends to be very fast, occurring with the decay time of sub-ns.

Following this observation devices with CdSe/ZnS NCs as energy acceptors were prepared in order to substitute InP/ZnS NCs with more efficient ones.

A typical current-voltage characteristic of the LED is presented in Figure 6.7, where the inset shows the low voltage part of the curve on a μA scale. The device has a good turn-on voltage value of around 4.2 V, but starts emitting light intense enough to see by naked eye at 2.6 V. Patterning followed by post-etching treatment didn't affect the IV

6. Patterned LEDs.

characteristics. This confirms that surface damage caused by ICP etching was successfully removed and patterning using etching techniques may be used without sacrificing the electrical characteristics of the device.

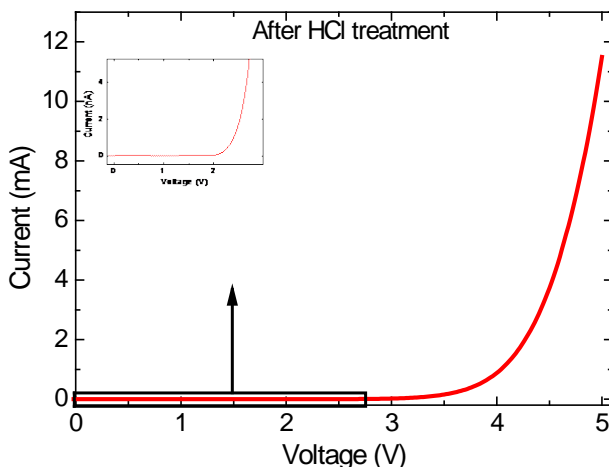


Figure 6.7. IV characteristic of the device. Inset shows low current and low voltage part of the curve.

It should be noted, that the amount of the solution with CdSe NCs deposited on a sample was the same as amount of the solution with InP NCs. It resulted in higher emission from the CdSe NCs. Figure 6.8 presents PL and EL measurements of the patterned device with CdSe/ZnS NCs covering conformally the surface of the LED. For the optical measurements the same blue laser emitting at 405 nm together with 405 nm notch filter were used. Optically driven sample exhibits strong emission from the NCs, but driven electrically it shows negligible color conversion of blue to the red emission via optical absorption and RET. Since the geometry of the device allows only small number of NCs to interact with the QW carriers, it is not expected that RET would be significant.

6. Patterned LEDs.

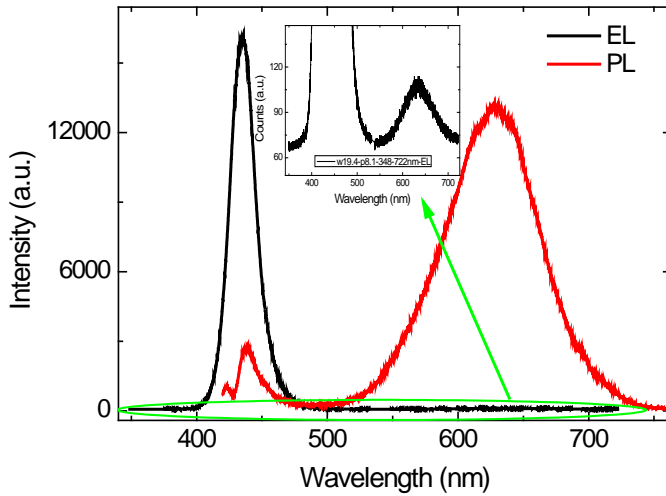


Figure 6.8. PL and EL measurements of the patterned device with CdSe/ZnS NCs in close vicinity to the QW.

Measurements of electrically driven diode showed higher overall emission from the patterned area. This can be seen even better in Figure 6.9, where the patterned areas are the brightest rectangular emission spots in the picture. Holes themselves help to extract light from the QWs, thereby increasing the external efficiency of blue emission [78], [146].



6. Patterned LEDs.

Figure 6.9. A photo of electrically driven device, two probes provide current to the electrical contacts. As generated photons are guided in GaN, light is emitted from large part of the chip around the contact device. Note, that the arrays of hole patterns are always brighter than the surrounding unpatterned parts of the same mesas.

Global characteristics of electrically and optically driven diodes have shown complicated behavior of devices. Time-resolved PL analysis performed with high spatial resolution has to be done. This analysis will give information about carrier dynamics in the small region where NCs are in close vicinity to the QWs instead of gathering signal from the area of tens of μm .

6.3 Non-radiative energy transfer in patterned devices

In order to measure RET and surface recombination in the patterned devices, micro-PL setup described in section 4.1.3 of chapter 4 had to be used. A variety of laser excitation wavelengths and collection wavelengths (defined with bandpass filters) were used to analyze the effects of RET, surface recombination and optical absorption on carrier recombination in the quantum wells and in the nanocrystals. This way, we were able to demonstrate RET (as opposed to an extra non-radiative recombination in samples with NCs) and we were able to reach conclusions regarding optimum sample design for maximum color conversion efficiency.

Prior to the micro-PL measurements, PL and EL was measured to study the effect of the patterning on the device performance, which was shown in previous section.

6.3.1 Influence of RET on dynamics of carriers in the QW

In order to study the carrier dynamics in the QWs micro-PL data were acquired with 405 nm laser and 420-520 nm bandpass filter to remove the remaining laser signal and the emission from the NCs.

Patterned devices with hole sizes of 1 and 1.5 μm and array period of 2 and 3 μm , respectively, were investigated. Their microscope pictures and examples of micro-PL maps are shown in Figure 6.10 and Figure 6.11. The fact that the images in Figure 6.10 (b) and Figure 6.11 (b) do not show any emission from the holes can be explained by the size of the excitation laser beam spot used to pump optically the QWs. Due to the use of a high NA objective lens the laser beam size is around 0.8 μm in diameter. As the pattern was etched through the QWs, there is no excitation and correspondingly collection when the excitation point is inside the hole.

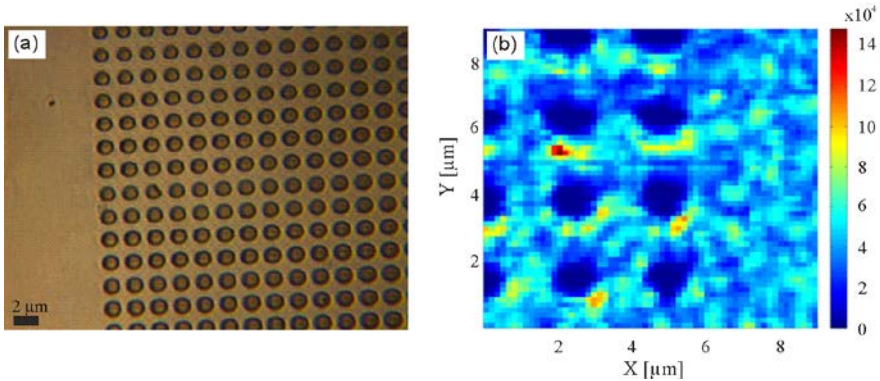


Figure 6.10. (a) A microscope picture of the sample with holes size of 1 μm and array period of 2 μm before micro-PL, and (b) a micro-PL map of the QW emission of the patterned and unpatterned areas of this sample, measured in the area 9 by 9 μm .

6. Patterned LEDs.

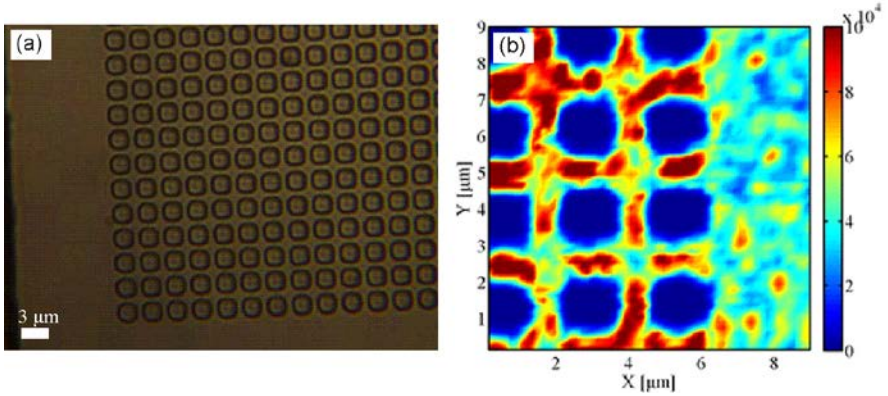


Figure 6.11. (a) A microscope picture of the sample with holes size of $1.5\ \mu\text{m}$ and array period of $3\ \mu\text{m}$ before micro-PL, and (b) a micro-PL map of the QW emission of the patterned and unpatterned areas of this sample, measured in the area $9\ \mu\text{m}$ by $9\ \mu\text{m}$.

In Figure 6.12 (a) we present a scanning electron microscopy (SEM) image of a typical patterned sample surface. Although, following the patterning, wet chemical etching to remove the damaged material was used, surface recombination that could compete with RET remained an issue in the device design since it was present even in as-grown wafer (see chapter 5). It has been addressed by adding another processing step: atomic layer deposition (ALD) of 1, 4, 10, and 25 nm aluminum oxide spacer layers on different chips. The aluminum oxide layers with different thicknesses allow us to investigate distance dependence of non-resonant energy transfer (RET) between the energy donor QWs and energy acceptor NC dipoles [36], as well as the effect of passivation on the QWs. Finally, a layer of colloidal CdSe/ZnS nanocrystals (NCs) was spun from a solution containing excess of oleylamine ligands on top of the aluminum oxide layer. Nanocrystals emitting at $620\pm 10\ \text{nm}$ wavelength were used. We verified the uniformity of the QW and NC layers by recording the spatially resolved photoluminescence (PL). For simplicity, the LED samples with 1, 4, 10

6. Patterned LEDs.

and 25 nm thick aluminum oxide layers will be referred to as S1, S4, S10, and S25 throughout the chapter.

Spatial and time-resolved photoluminescence (TRPL) measurements, as shown for instance in Figure 6.12 (b), were performed using a 405 nm pulsed diode laser as an off-resonant excitation light source for the QWs and NCs. The green 532 nm laser was used to excite selectively the NCs. The laser beam sizes were approximately $0.8\ \mu\text{m}$ and $0.6\ \mu\text{m}$ in diameter for the blue and green lasers, respectively.

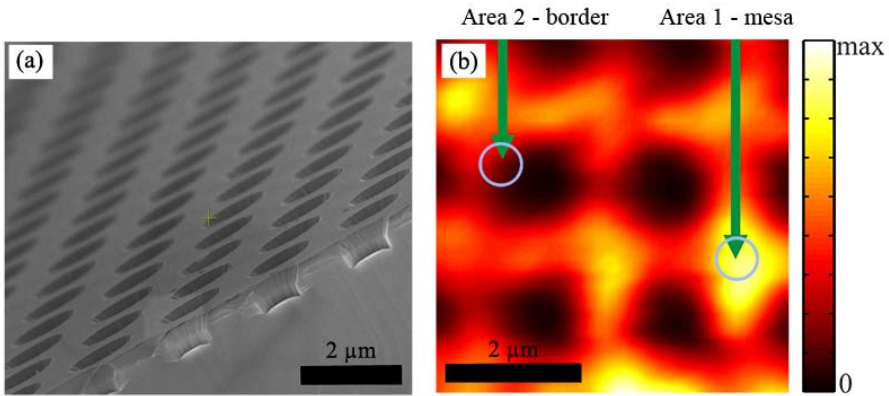


Figure 6.12. SEM image of the patterned area (a); micro-PL intensity (of 420 to 520 nm) map of sample S1 (b), positions of areas 1 and 2 are indicated.

A typical micro-photoluminescence (micro-PL) map of the QW signal taken on sample S1 on an area patterned with holes is presented in Figure 6.12 (b). A strong PL signal is obtained from the mesa region between the holes, while almost no signal emerges from the center of the hole, where the QWs were etched away. Two regions of the sample, labeled “area 1” and “area 2” are marked in the figure and will be compared throughout the text. Area 1 is located between two different holes, as shown in Figure 6.12 (b) and also indicated by the circles in Figure 6.4, while area 2 was chosen at the edge of the hole, at the location where the PL signal dropped by a factor of 3 relative to the

6. Patterned LEDs.

signal from area 1. The proximity of the quantum wells to the sample surface in area 2 (as illustrated in Figure 6.4) supports RET between QWs and NCs, as well as surface recombination of QW excitons. It should be noted that the carrier decay rates from area 2 (taken near the edge of the holes) are affected by the carrier decay rates from the close-by region defined by the beam size of the excitation laser, which is larger than the small border area 2, as shown by blue circles in Figure 6.4 and Figure 6.12 (b).

Following the acquisition of micro-PL intensity maps for samples with different thicknesses of Al_2O_3 passivation layer, maps with PL decay curves were acquired with the same spatial resolution. The QW decay curves from both areas 1 and 2 extracted from the maps are shown in Figure 6.13 (a). Each curve is an average of around 10 spatially different points within the same area. The same averaging is performed to reduce the noise and ensure that spatial variations are accounted for all the data shown in this chapter. All decay rates presented here are total decay rates obtained from single exponential fits.

The PL decay has been fitted using following equation:

$$I(t) = I_0 \exp(-k \cdot t) \quad (6.1)$$

where $I(t)$ shows PL intensity dependence with time, I_0 is the intensity at time zero, k is corresponding decay rate. Single exponential function represents well the PL intensity decay in the time period of interest. Only very first initial decay times after laser activation have been used for the data analysis as both RET and recombination on SS are fast processes. As they are in order of several ns and error bars of measured times (which are due to the averaging measurements from different points of the same area in the same map) are in order of few hundred ps,

6. Patterned LEDs.

instrument response function (IRF) which is around 200 ps was not deconvoluted from the decay curve before fittings.

In general, the decay rates from the area 1 of different samples are similar and vary between $0.2 \pm 0.02 \text{ ns}^{-1}$ and $0.23 \pm 0.02 \text{ ns}^{-1}$. The photoluminescence decay from the area 2 is faster than that from the area 1 in different samples, indicating the presence of an additional carrier recombination process at the border compared with the mesa centers. The recombination rate in the area 2 scales inversely with the thickness of the aluminum oxide layer and there is very little difference between the recombination rates from both areas of sample S25 ($\Gamma_{S25NC,1} = 0.22 \pm 0.03 \text{ ns}^{-1}$ and $\Gamma_{S25NC,2} = 0.27 \pm 0.03 \text{ ns}^{-1}$ for areas 1 and 2, respectively). The higher decay rate in the area 2 compared to the area 1 could be caused both by RET from the QW to the NCs [147], [148] and non-radiative surface recombination [132]. From these measurements alone, we cannot determine the exact physical origin for the higher decay rate at the border of the hole.

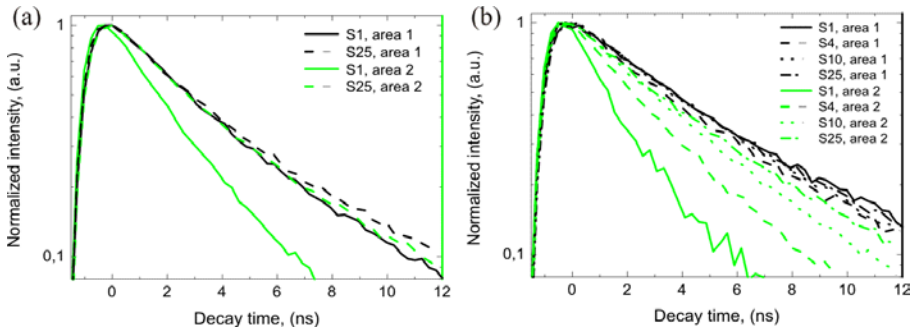


Figure 6.13. (a) QW PL decays of samples S1 (solid line) and S25 (dashed line) from areas 1 (black) and 2 (green) before NCs deposition, and (b) Decay curves of QW emission from areas 1 and 2 (black and green, respectively), from all samples with NC deposited.

In order to investigate the effect of passivation on surface recombination, we recorded decay curves from samples S1 and S25 before the deposition of NCs, as shown in Figure 6.13 (a). Since in these

6. Patterned LEDs.

measurements no NCs are present, the effect of RET can be excluded as a possible decay channel in the border area 2.

The signal from the area 2 of sample S1 with a rate of $k_{S1,2} = 0,37 \pm 0,04 \text{ ns}^{-1}$, is faster than from the area 1, with a rate of $k_{S1,1} = 0,20 \pm 0,003 \text{ ns}^{-1}$. In contrast, the same decay rates: $k_{S25,1} = 0,27 \pm 0,02 \text{ ns}^{-1}$ and $k_{S25,2} = 0,27 \pm 0,03 \text{ ns}^{-1}$, respectively for areas 1 and 2 are measured for sample S25. These measurements illustrate, that non-radiative surface recombination significantly increases the total recombination rate of carriers in the QW decay rate close to the hole, and that it is eliminated to a large extend by the passivation through a 25 nm thick aluminum oxide layer. The difference between decay rates for the samples S1 and S25 from area 1 ($k_{S1,1}$ and $k_{S25,1}$) may originate from the diffusion of carriers to the surface states, which shouldn't take place for the sample S25.

The observations from Figure 6.13 (a) and (b) show that the QW carrier decay rates extracted from area 1 are having similar values for all the samples and in particular they are not affected by the presence of NCs or by the aluminum oxide layers. The carrier decay rate $k_{S1N,2} = 0,51 \pm 0,04 \text{ ns}^{-1}$ from area 2 of sample S1 with a NC layer (see Figure 6.13 (b)) is significantly larger than the rate $k_{S1,2} = 0,37 \pm 0,04 \text{ ns}^{-1}$ obtained without NCs (see Figure 6.13 (a)). This clearly indicates that an additional recombination channel must be present when NCs are placed in the vicinity of the QWs. Strong dependence of the QW decay rate on the aluminum oxide layer thickness suggests short range effects, such as RET from the QWs to the NCs as possible additional decay component.

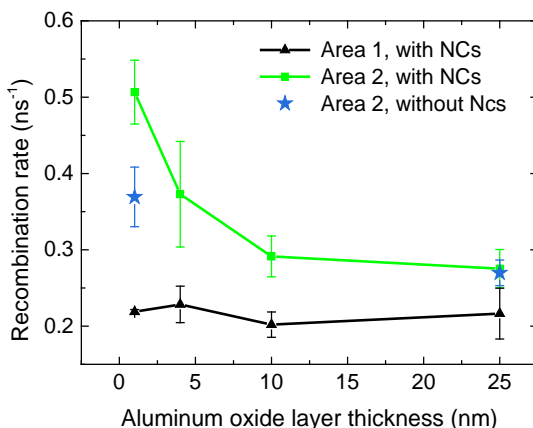


Figure 6.14. QW PL decay rates vs. thickness of the oxide layer from area 1 with NCs on top (black triangulars), area 2 with NCs on top with possible RET+SS (green squares), area 2 without NCs on top with possible SS on S1 and S25 (blue stars).

The total decay rates obtained from all curves of Figure 6.13 are plotted against the aluminum oxide thickness in Figure 6.14. The mean values and error bars (equal to the standard deviation) are derived from different points of corresponding TRPL map. A strong dependence of the rates on the aluminum oxide layer thickness is clearly observed in area 2 both for the measurements with and without NCs, especially for an aluminum oxide layer of less than 10 nm-thick. From these measurements we conclude that for QW to NC separations of more than 10 nm RET between donor and acceptor materials does not occur.

6.3.2 Influence of RET on the dynamics of carriers in the nanocrystals

The main conclusion of the previous section simply states that the recombination of electron-hole pairs in the QW is faster in the presence of the NCs in its vicinity and RET does not occur at separation distances

6. Patterned LEDs.

between the QW and NCs of more than 10 nm. In order to distinguish RET from potential non-radiative surface recombination processes introduced by the NCs layers, the PL and decay curve maps of the NCs have also be measured with excitation with a 405 nm laser and a 562 nm long-pass filter to eliminate the collection of laser and QW emission light.

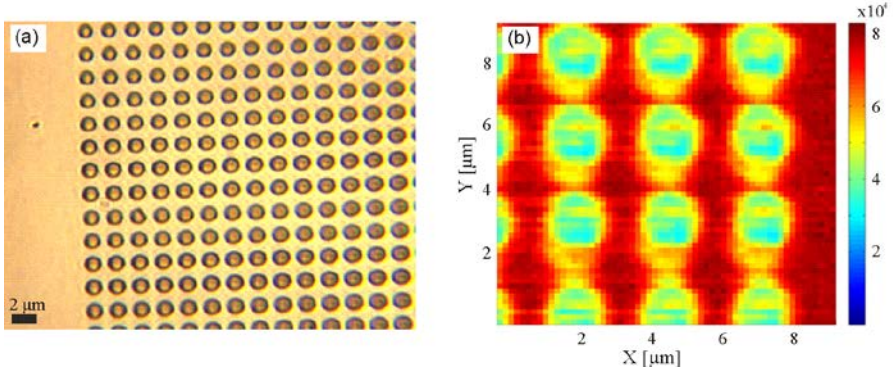


Figure 6.15. (a) A microscope picture of the sample with holes size of 1 μm and array period of 2 μm before micro-PL, and (b) a micro-PL map of the NCs emission of the patterned and unpatterned areas of this sample, measured in the area 9 by 9 μm .

A $1/e$ decay times map of the NCs is presented in Figure 6.16. The scan was taken from an area with a size of 9 by 9 μm (X and Y axis) in steps of 150 nm. One can easily recognize the hole pattern in the image and the fact that NCs have apparently a longer decay time in close proximity to the QW (inside the pattern, close to the edge), indicating the presence of RET. In this case the population of excitons in the NCs decays with its typical decay rate, but it increases via RET as long as there are electron-hole pairs present in the QWs resulting in an apparent longer average decay time of the NCs in the presence of RET.

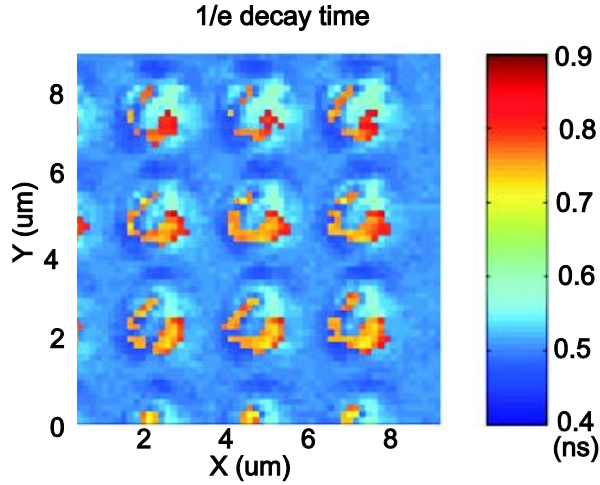


Figure 6.16. $1/e$ decay time map of NCs deposited on a wafer under optical pumping.

Another conclusion that can be drawn from the measurement in Figure 6.16 is that the hole size is larger than the area where RET had occurred, some areas inside the hole are not involved in RET, which means that the efficiency of this process may be improved by changing the pattern dimensions, reducing the hole size.

Typical NC decay curves taken under 405 nm laser excitation from samples S1 and S10 are presented in Figure 6.17. There is a clear difference between the decay curves in areas 1 and 2; the PL decay curves from area 2 are delayed compared to the curves taken from area 1. After the delay, the photoluminescence from areas 1 and 2 decay with identical rates of $k_{NC} = 0,09 \pm 0,007 \text{ ns}^{-1}$. Since the delay is of the order of the decay rate of carriers in the QW (shown in Figure 6.17), the time delay can be explained as non-radiative energy transfer from the QW to the NCs. It should be noted, that in all measurements the time zero was defined in the same way: by the reference signal from the laser controller triggering the timing card.

6. Patterned LEDs.

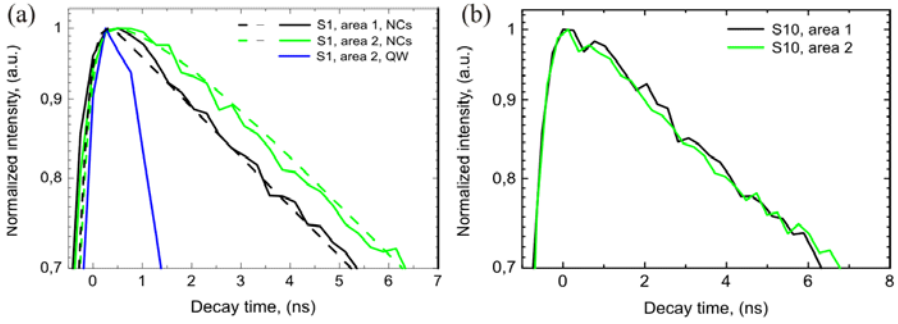


Figure 6.17. Experimental (solid lines) and simulated (dashed lines) decay curves from NCs of sample S1 (a) and experimental results for sample S10 (b) for areas 1 and 2 (black and green curves, respectively). For comparison, in (a) we also plot the bulk QW decay curve as a blue line.

Decay curves for S4 and S25 obtained under the blue laser excitation are shown in Figure 6.18. Dashed lines in Figure 6.18 (a) show results of the simulations, confirming that RET is present in the structure with 4 nm of aluminum oxide layer. Decay curves from sample S25 in Figure 6.18 (b) overlap each other as RET is very unlikely at this separation distance and as expected from the data for sample S10.

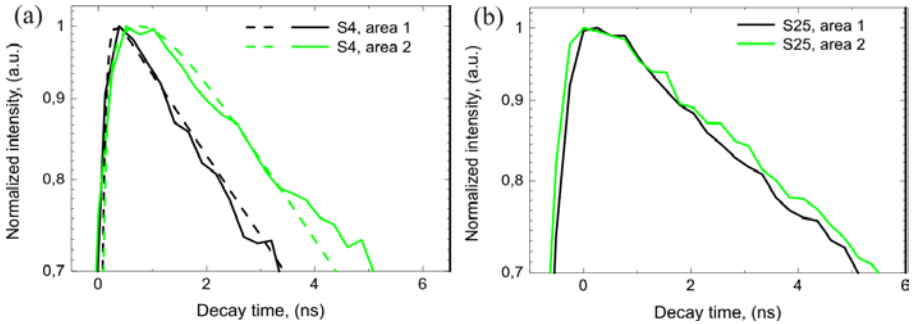


Figure 6.18. Experimental (solid lines) and simulated (dashed lines) decay curves from NCs of sample S4 (a) and experimental results for sample S25 (b) for areas 1 and 2 (black and green curves, respectively).

In order to simulate the RET process a system of three equations was used:

$$\frac{dn_{QW}}{dt} = -(k_{rad}^{QW} + k_{SR}^{QW} + k_{RET}) * n_{QW} \quad (6.2)$$

6. Patterned LEDs.

$$\frac{dn_{NC1}}{dt} = -k_{tot}^{NC1} * n_{NC1} + k_{RET} * n_{QW} \quad (6.3)$$

$$\frac{dn_{NC2}}{dt} = -k_{tot}^{NC2} * n_{NC2} , \quad (6.4)$$

Here, n_{QW} , n_{NC1} and n_{NC2} are exciton populations in the QWs and NCs close to the QWs and far from those, respectively, k_{rad}^{QW} and k_{SR}^{QW} are radiative rate far from the surface, and surface recombination rate of the QW, k_{tot}^{NC1} and k_{tot}^{NC2} to the total decay rates of the NCs close and far from the QWs. This total decay rate is comprised of radiative and non-radiative contributions. And k_{RET} is the RET rate from the QWs to the NCs. Photon absorption and RET between pairs of NCs are neglected as much weaker effects.

Due to the fact that the laser beam is slightly larger than the small area 2 (Figure 6.4) and NCs that are far from QW walls are also excited by the laser, equation 6.4 has been added to show their contribution. The energy levels of the QW and NCs are presented in Figure 6.19 by numbers from 1 to 6. Energy levels of the NCs in the close proximity are far from the QWs are taken into account and shown in this figure.

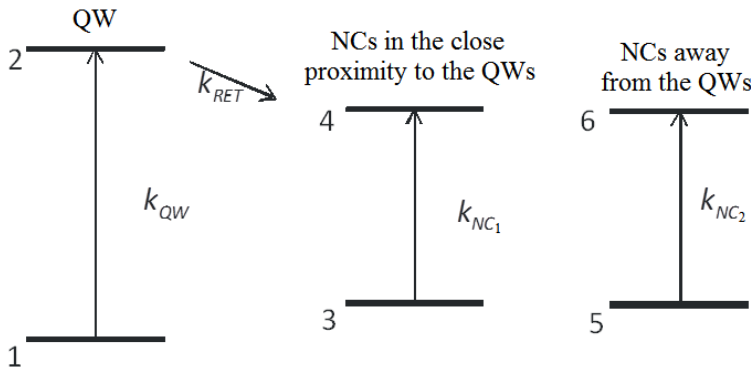


Figure 6.19. Energy levels of the QW and NCs that are excited by the laser.

Measured decay rates k_{NC1} and k_{NC2} were used for the simulations, n_{QW} and $n_{NC1} + n_{NC2}$ were set to 1 at $t=0$ while k_{RET} and n_{NC1}/n_{NC2} were

6. Patterned LEDs.

freely adjusted parameters. As a starting point k_{RET} derived from Figure 6.14 was used for S1, but it was further adjusted to account for spatial averaging due to the size of the laser beam. The simulation results for the samples S1 and S4 agree well with the experimental data, as shown by the plots in Figure 6.17 (a) and Figure 6.18 (a). Due to the unknown ratio of $n_{\text{NC1}}/n_{\text{NC2}}$ we can only determine a lower bound on the RET rate from the comparison of the data with the simulations.

The shift of the decay curves obtained from samples S1 and S4 is related to the energy transfer from QWs to the NCs and therefore occurs only within the lifetime of the excitons in the QWs. Since the decay of the QW excitons (blue line in Figure 6.17 (a)) is more than a factor of 2 faster compared to the NC decay rate, the resulting shift is small compared with the decay times of the NCs.

When the separation between QWs and NCs is increased to 10 nm or 25 nm, there is no difference in NC decay curves between areas 1 and 2, as shown for S10 in Figure 6.17 (b). We therefore conclude that the different QW decay dynamics of the samples S10 and S25, as presented in Figure 6.13 (b), is due to the effect of SR.

From the figures above is clear, that efficiency of RET is limited by the radiative lifetime of the NCs. Non-radiative energy transfer depends also on processes in the QWs, but as they are faster than radiative lifetime in the NCs (shown in Figure 6.17 (a)) electron-hole pair from the QW has to "wait" until states in the NC will be ready for an energy transfer to occur and result in radiative recombination. In fact the transfer can occur at any time but it will result in Auger recombination if there is already an exciton in the NC. This mismatch may be responsible for the difference between the measured emission of light from NCs under optical pulsed excitation and electrical CW excitation as discussed in the section 6.2.

6. Patterned LEDs.

Further evidence that RET is responsible for the time delayed decay, shown in Figure 6.20 and Figure 6.21 (a), comes from TRPL maps with NCs on top measured upon selective excitation of the NCs with the 532 nm pulsed laser. Under these conditions only NCs are excited. The resulting decay curves from areas 1 and 2 of sample S1 are presented in Figure 6.20. Figure 6.21 (a) shows 20 decay curves from both areas 1 and 2, while Figure 6.21 (b) presents $1/e$ decay time map of this sample. The decay curves in Figure 6.20 as well as all the curves in Figure 6.21 (a) overlap each other, thus demonstrating that in the absence of QW excitation, there is no difference in the carrier dynamics of NCs in the areas 1 and 2, and no influence of the pattern on the carrier dynamics of NCs is seen. Furthermore, this observation confirms that the differences in carrier dynamics, obtained under excitation with 405 nm laser are due to non-radiative coupling of the electron-hole pairs in QWs to the NCs excitons.

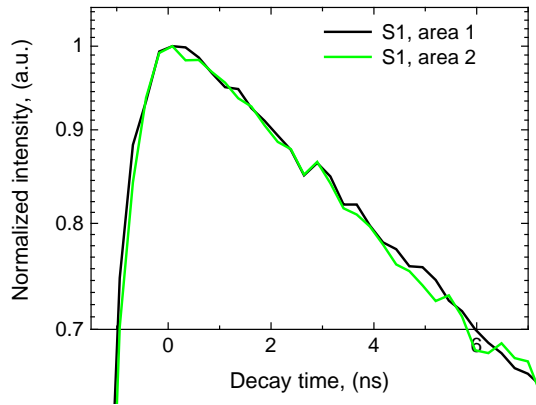


Figure 6.20. NCs PL decay curves of sample S1 from areas 1 (black) and 2 (green) obtained with pulsed 532 nm laser excitation.

6. Patterned LEDs.

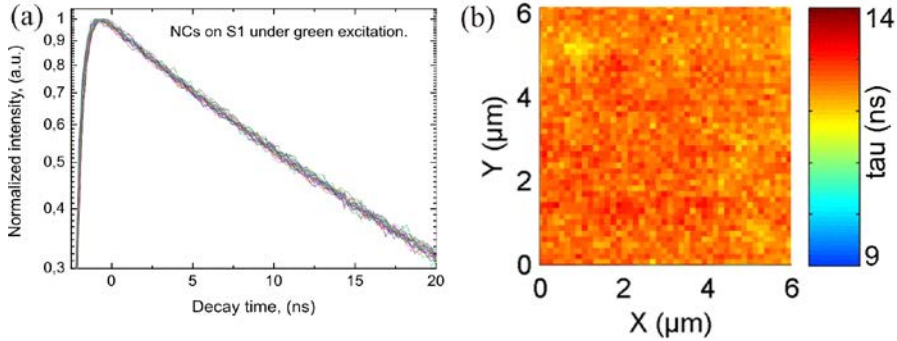


Figure 6.21. (a) decay curves from 20 different points of NCs on top of sample S1 under green laser excitation and (b) 1/e decay map of this sample.

6.4 Conclusions

In conclusion, we have presented light-emitting diodes fabricated with hole patterns for color conversion via non-radiative resonant energy transfer from the quantum wells to the nanocrystals. Device patterning improved the extraction efficiency of the blue light [146] and allowed NCs to be placed close to the QWs in order for RET to occur. Non-radiative energy transfer from the QWs to the NCs occurred in the close proximity to the QWs which was confirmed by longer decay times of NCs placed there.

Non-radiative energy transfer from InGaN/GaN QWs to CdSe/ZnS NCs was studied by measuring the carrier dynamics of both the QWs and the NCs. By doing so, the modification of surface recombination due to the NC layer as the origin of the observed increased recombination rate in the QWs was ruled out. The measurements performed on the NCs with green laser excitation have proven that the dynamic modifications of the NCs decay in area 2 under blue laser excitation were caused by the RET.

6. Patterned LEDs.

RET was found to decrease strongly with the separation between QWs and NCs, and it was not measurable at separation of 10 nm or more. Thin passivation layers reduce surface recombination, but they also slow down the RET rate due to increased separation between the donor and acceptor layers. It is therefore very important that device processing is optimized to avoid the generation of surface states for devices which would utilize RET.

The white color generation with color temperature of 6190 K and CRI of 73 was achieved using optically driven blue LED with InP/ZnS NCs (with central emission wavelength of 580 nm) deposited inside the hole patterns. Electrically driven diodes did not show white light generation irrespective of the choice of NCs. A mismatch between the measured fast decay rates of carriers in the QWs and slow decay rates of the NCs in combination with high Auger recombination probability may be responsible for the difference between the measured emission of light from NCs under optical pulsed excitation and electrical CW excitation.

7. Conclusions and outlook

7. Conclusions and outlook

A hybrid white LED based on non-radiative resonant energy transfer from the QWs to the emissive NCs was proposed and demonstrated in two different device geometries. In the first type of LED structure, thin capping layer was covering QWs, resulting in small separation distances between the QWs and the NCs needed for the resonant energy transfer. The second type of device was based on standard LED structure which was patterned to expose quantum wells from the sides.

Fabrication of devices with both geometries was established in the Danchip clean room facilities. Some processes such as dry etching of InAlGaN materials, p- and n-type contact metal combinations were developed.

Non-radiative resonant energy transfer (RET) between InGaN QW and nanocrystals was experimentally demonstrated for devices of both types. Strong dependence of RET efficiency on the separation between the QW and the NCs was shown. Decay rate of the carriers in the QW drops from the $\sim 0.51 \text{ ns}^{-1}$ to $\sim 0.37 \text{ ns}^{-1}$ when separation between the QW and NCs increases from 1 to 4 nm in samples with the patterned geometry. Influence of recombination on surface states and passivation effect of ligands, connected to the NCs, have to be considered for hybrid devices.

Optically driven diode emitting white light with CRI of 73 was shown. However, electrically driven LED showed very little luminescence from the nanocrystals, proving that RET does not result in sufficient color conversion. This has been partly explained by Auger

7. Conclusions and outlook

recombination and a long lifetime of excitons in the NCs compared with the lifetime of electron-hole pairs in the quantum well.

If carriers decayed radiatively faster in NCs, under CW excitation (EL) they would produce more red photons. NCs or other materials such as organic molecules with faster decay radiative decay times should lead to potentially more efficient white LEDs.

Although RET was measured in both types of devices, the patterned standard LED, having good electrical characteristic, has better potential to be developed into a commercially competitive device. In future, optimization of the pattern in such devices to achieve larger area of interactions between the QW and the NCs for the LED should be performed. Since stronger light extraction in the patterned device has been observed, it would be interesting to consider patterns with photonic properties: e.g. photonic crystals. The device would benefit greatly from incorporating NCs with higher quantum efficiencies. Nanocrystals of different size, i.e. emission wavelength, should be used for broader emission spectrum, and thus higher CRI value and easier color temperature control. Since RET and surface recombination are both strong at the same length scales, more work should be devoted to minimizing the surface defects density many of which may be introduced during device processing.

Resonant energy transfer can be used for other applications such as: single photon sources based on nanocrystals, sensors of the separation between the molecules in physical and biological research and clinical laboratories. RET can also be used to improve the spectral characteristics of fluorescent dyes and dye combinations, such as the tandem dyes in flow and image cytometry and the RET primers in DNA sequencing and polymerase chain reactions.

7. Conclusions and outlook

Photo- and other proteins and many enzymes involved in photo-activated biological events can be tuned and enhanced by using light harvesting NCs.

0. Appendix A. Patterned LED fabrication procedure.

Appendix A. Patterned LED fabrication procedure.

Cleaning:

5 min in acetone (+ultrasonic), 1-2 min in ethanol, 1 min rinsing in running DI water, drying with nitrogen.

If very dirty: a) piranha wash – $\text{H}_2\text{SO}_4:\text{H}_2\text{O}_2 = 4:1$ for 5-10 min,

 b) HCl for 5-10 min.

SiO₂ deposition

Depositing of 300 nm of SiO₂ in PECVD2: SiO₂ for 3 minutes program "SiO₂KY" also with Si piece for SiO₂ thickness inspection. Deposition rate is 100 nm/min.

Chemical reaction used for glass deposition is: $\text{SiH}_4 + 2 \text{N}_2\text{O} \rightarrow \text{SiO}_2 + 2\text{H}_2 + 2\text{N}_2$

Check of SiO₂ thickness in FilmTek.

Choose program 1_SiO₂_4inch_1point, measure in several points. Thickness may be different in the corners compared with the center of the sample.

HMDS treatment. To be placed in HMDS vapor for 15 min, then in free air in fume hood for 5 min.

Photolithography.

Spinning of photolithography resist AZ5206E (thickness of resist ~600 nm)

Program 3 was used with settings:

0. Appendix A. Patterned LED fabrication procedure.

1 40 10	Closed spin 400rpm, acc 1000rpm/s
3 5	For 5 s
1 600 40	Closed spin 4000rpm, acc 4000rpm/s
3 30	For 30s

Beads to be removed. Then prebake for 90 s in 90°C.

Expose using mesa mask and program 8: vacuum mode, on time: 10 sec, align sep: 20um, 10s, 10s. Development: 1 min in AZ351B 1:5 H₂O, DI rinse and N₂ dry.

Check pattern is well developed with microscope.

Removing of resist residues with oxygen (O₂) plasma. Time used: 60 s, pressure 0.2mbar O₂, power 40%. One needs to be careful and check the power of the plasma asher, not to use higher power and remove all resist.

SiO₂ etching.

SiO₂ etch in RIE (Plassys). The process etch rate is 30 nm/min for SiO₂ and 29 nm/min for the resist. The parameters of CHF₃/O₂ etch were: O₂ gas – 2.0 sccm, CHF₃ gas – 16.0 sccm, RF = 60 W, pressure – 100 mTorr, etch time – 10-15 minutes, to be more precisely controlled with the laser interferometry.

After etching to clean chamber using process clean.prg consist of 10 minutes O₂ etch.

Check glass thickness (on Si wafer) in FilmTek.

Strip resist with acetone (10 min), ethanol for 1min, rinse in DI water for 1 min and N₂ dry; O₂ plasma Asher (power 100%, 2-3 minutes, up to 5 minutes) to remove rests of photoresist. Optical microscope is needed to be used to confirm that glass is etched through, Dektak profiler for inspection of the etched depth.

0. Appendix A. Patterned LED fabrication procedure.

E-beam lithography (patterned device):

- a) ZEP deposition (thickness is around 500 nm),
- b) 20 nm of Al in Wordentec,
- c) E-beam lithography,
- d) ZEP development and Al removing:
 - MF-322 for 50 s to remove Al, rinse in water, N₂;
 - ZED N50 for 2 min, IPA for 30 s, N₂

SiO₂ etching in RIE (Plassys), ZEP removal.

Acetone, ethanol cleaning of surface by dipping the sample in the beaker, as described in section "cleaning".

Inspection of the sample in the optical microscope and if needed using scanning electron microscope (SEM).

GaN etching

Mesa formation and patterning of mesas in ICP. Use “GaN etch” program for 1 min (550 nm depth). Or 45-50 s for 400-450 nm. Detailed recipe with gases and flows is shown in Appendix B.

Use Dektak afterwards to measure etch depth with rests of SiO₂.

Remove glass (BHF etch rate ~200 nm/min), Dektak without SiO₂ to measure GaN etch depth.

Post-ICP treatment: etching in 37% HCl for 1 hour.

Cleaning. Acetone 5min, Ethanol 1min+squirt, DI water for 1 min, N₂ dry.

Inspection of the sample quality and surface cleanliness in the optical microscope and if needed using SEM.

Top contact.

0. Appendix A. Patterned LED fabrication procedure.

Photolithography for top contact (using “T”-marked photolithography mask)

Hotplate bake @ 170°C for 5 min.

1. Spin on adhesion promoter AP3000 (for the metal):

2 50 10	Open spin 500rpm, acc 1000rpm/s
3 15	For 15 s
2 100 10	Open spin 1000rpm, acc 1000rpm/s
3 60	For 60s

2. Spin Lift-Off Resist (LOR5B), thickness ~0.7um

1 40 10	Closed spin 400rpm, acc 1000rpm/s
3 5	For 5 s
1 200 40	Closed spin 2000rpm, acc 4000 rpm/s
3 45	For 45s

3. Edge beads were removed using EBR PG and then baked for 5 min @ 170°C (Set point 180°C).

4. Spinning of AZ5206E (resist thickness ~0.6 µm) which will be exposed in aligner to open windows for metal deposition and then for lift-off.

1 40 10	Closed spin 400rpm, acc 1000rpm/s
3 5	For 5 s
1 400 40	Closed spin 4000rpm, acc 4000rpm/s
3 30	For 30s

5. Edge beads were removed using EBR PG and sample was baked for 90s @90C.

0. Appendix A. Patterned LED fabrication procedure.

6. Alignment and exposure of resist with top metal pattern. program 3: exposure time 10 sec, Vacuum mode: 20um, 10s, 10s. Sample was aligned using alignment marks.

7. Developed with AZ351B 1: 5 H₂O for 5min with stirring gently while exposing.

8. HCl cleaning (10 min) before metal deposition

9. Evaporation of “p-type” contact metals in Physimex. Metal combination is Ni₁₅Au₂₀₀.

10. Lift-off. Samples were immersed in warm “Remover 1165” at 60°C for 1-2 hours. Then rinsed by Isopropanol and DI water and finally dried with N₂.

11. Thermal annealing by RTA at 610 C for 30 min.

Bottom contact.

1. Lithography for bottom contact (using “B”-marked photolithography mask) - same steps as for top contact but different mask.

2. HCl cleaning (10 min).

3. Evaporation of “n-type” contact metals combination using Alcatel (TiAlTiAu, prog.#45).

4. Lift-off. Samples were immersed in warm “Remover 1165” at 60°C for 1-2 hours. Then rinsed by Isopropanol and DI water and finally dried with N₂.

Ultrasonic bath with low level of ultrasound can be used (level 1-2) if metal does not lift off within 1-2 hours.

Nanocrystals deposition:

Is done using spin-coating. Around 50 µl of solution with NCs was used for a chip with the size 7*7 mm.

0. Appendix A. Patterned LED fabrication procedure.

2 20 10	Open spin 200rpm, acc 1000rpm/s
3 10	For 15 s
1 700 50	Closed spin at 7000rpm, acc 5000rpm/s
3 60	For 60s

0.

0. Appendix B. Etching recipes for RIE Plassys and III-V ICP placed in the Danchip clean room for III-Nitrides etch.

Appendix B. Etching recipes for RIE Plassys and III-V ICP placed in the Danchip clean room for III-Nitrides etch.

Parameters for SiO₂ etch in RIE.

CHF ₃ flow	16 sccm
O ₂ flow	2 sccm
RF power	60 W
Pressure	100 mTorr
SiO ₂ etch rate	30 nm/min

Parameters for GaN etch in RIE.

Recipe #1 is for shallow etch, where higher etching depth precision and better surface morphology is required. Recipe #2 is for faster and deeper etch.

Recipe #1.

Cycle 1. GaN etch.

CH ₄ flow	8.3 sccm
H ₂ flow	42 sccm
RF power	60 W
Pressure	84 mTorr
Length of the cycle	2 min

Cycle 2. O₂ polymer cleaning.

O ₂ flow	40 sccm
RF power	20 W
Pressure	150 mTorr
Length of the cycle	1 min 30 sec

0. Appendix B. Etching recipes for RIE Plassys and III-V ICP placed in the Danchip clean room for III-Nitrides etch.

GaN etch rate is around 3 nm/min

Recipe #2.

Cycle 1. GaN etch.

CH ₄ flow	8.2 sccm
H ₂ flow	41 sccm
RF power	90 W
Pressure	80 mTorr
Length of the cycle	2 min

Cycle 2. O₂ polymer cleaning.

O ₂ flow	40 sccm
RF power	20 W
Pressure	150 mTorr
Length of the cycle	1 min 30 sec

GaN etch rate is around 6 nm/min

Parameters for GaN etch in ICP:

Cl ₂ flow	30 sccm
Ar flow	10 sccm
Platen power	200 W
Coil power	600 W
Pressure	2 mTorr
Platen chiller temperature	20°C

GaN etch rate is around 550 nm/min

Appendix C. Simulations of the effect of GaN capping thickness on recombination of electron-hole pairs in high indium-content InGaN quantum wells.

The structures were simulated using a fully coupled piezoelectric model which includes strain, piezoelectric effects, spontaneous polarization and surface charges. Lattice constants of $a_s = 3.222 \text{ \AA}$ and $c_s = 5.233 \text{ \AA}$ has been assumed for the substrate to incorporate the relaxation induced by the superlattice layers [149]. First, the full coupling of spontaneous polarization, piezoelectric coefficients, electric fields, and lattice mismatch is included in the continuum elastic equations for the strain calculation. The resulting strain tensor in space is then used for the band structure calculations, performed using a one-band effective mass model for the conduction band. Hence the conduction-band Hamiltonian is:

$$H_c = -\frac{\hbar^2}{2} \left(\frac{\partial}{\partial z} \frac{1}{m_{\parallel}(z)} \frac{\partial}{\partial z} \right) + D_{\parallel}(z)\epsilon_{33} + D_{\perp}(z)(\epsilon_{11} + \epsilon_{22}) + eV(z) + V_{c,B}(z) \quad (\text{C.1})$$

where m_{\parallel} , D_{\parallel} , D_{\perp} , ϵ_{ij} ($i, j = 1, 2, 3$), V and $V_{c,B}$ are the conduction-band effective mass, the anisotropic deformation potentials, the strain tensor, the electric potential and the conduction band edge, respectively. The valence-band Hamiltonian in the one-band model is given by:

0. Appendix C. Simulations of the effect of GaN capping thickness on recombination of electron-hole pairs in high indium-content InGaN quantum wells.

$$H_v = -\frac{\hbar^2}{2} \left(\frac{\partial}{\partial z} \frac{1}{m_{\parallel, hh}(z)} \frac{\partial}{\partial z} \right) + (D_1(z) + D_3(z))\epsilon_{33} + (D_2(z) + D_4(z)\epsilon_{11} + \epsilon_{22} + eV_z + V_{v,B}(z)) \quad (C.2)$$

where $m_{\parallel, hh}$, D_1 , D_2 , D_3 , D_4 , ϵ_{ij} ($i, j = 1, 2, 3$), V and $V_{v,B}$ are the heavy hole effective mass, the anisotropic deformation potentials, the strain tensor, the electric potential and the valence band edge, respectively. All material parameters are step functions in space. It is assumed that the capping layer interfaces with vacuum which has an infinite barrier potential.

All the parameters used in the calculations (see table C1) were taken from [150] except from the piezoelectric coefficients and relative permittivities which have been taken from [151]. A surface charge density of $2.8 \cdot 10^{13} \text{ cm}^{-2}$ was used in calculations. This choice gives good agreement with experimental results and is in the range of surface charge densities reported previously [152]. It should be noted that there is no consensus in the literature regarding InN material parameters and there are some deviations in the parameters reported for GaN.

Change in surface charges leads to change of the band potential, wavefunctions and therefore emission wavelength as well as integral overlap between electron and hole wavefunctions. Figures, demonstrating dependence of the surface charge density are shown below.

TABLE C1. Material properties. Here m_0 is the free electron mass. All parameters are taken from Ref. [150], except the piezoelectric coefficients and

0. Appendix C. Simulations of the effect of GaN capping thickness on recombination of electron-hole pairs in high indium-content InGaN quantum wells. relative permittivities which have been taken from Ref. [151]. Bowing parameters for the band-gaps of 1.4 was used in calculations.

	GaN	InN
a [nm]	0.3189	0.3545
c [nm]	0.5185	0.5703
C_{11} [GPa]	390	223
C_{12} [GPa]	145	115
C_{13} [GPa]	106	92
C_{33} [GPa]	398	224
C_{44} [GPa]	105	48
e_{31} [C/m^2]	-0.45	-0.52
e_{33} [C/m^2]	0.83	0.95
e_{15} [C/m^2]	-0.38	-0.44
P_{sp} [C/m^2]	-0.034	-0.042
ε_{\parallel}	9.24	8.061
ε_{\perp}	10.35	7.054
$a_{c\parallel}$ [eV]	-11.3	-3.5
$a_{c\perp}$ [eV]	-4.9	-3.5
m_{\parallel} [m_0]	0.2	0.07
E_g [eV]	3.51	0.78
VBO [eV]	-0.5	0
$m_{hh,\parallel}$ [m_0]	1.88	1.16
D_1 [eV]	-3.7	-3.7
D_2 [eV]	4.5	4.5
D_3 [eV]	8.2	8.2
D_4 [eV]	-4.1	-4.1

0. Appendix C. Simulations of the effect of GaN capping thickness on recombination of electron-hole pairs in high indium-content InGaN quantum wells.

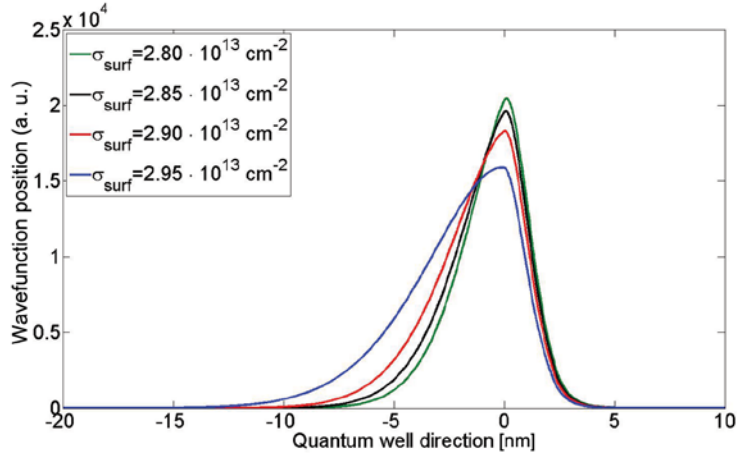


Figure C.0.1. Electron wavefunctions in the QW at various surface charge densities.

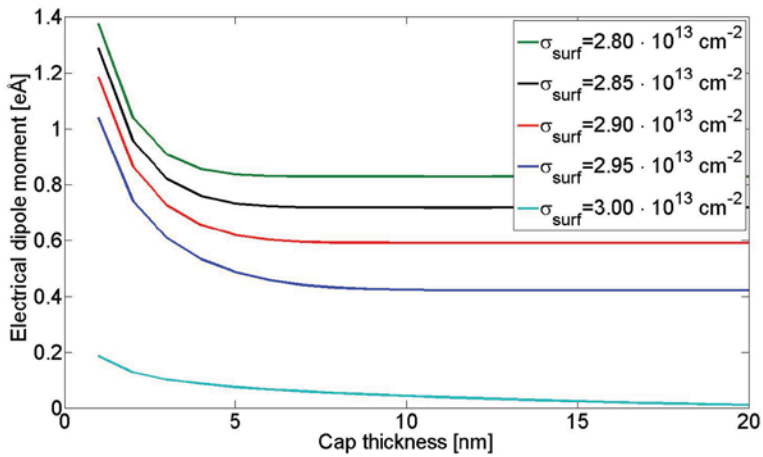


Figure C.0.2. Overlap integral between electron and hole GS versus cap thickness at various surface charge densities.

0. Appendix C. Simulations of the effect of GaN capping thickness on recombination of electron-hole pairs in high indium-content InGaN quantum wells.

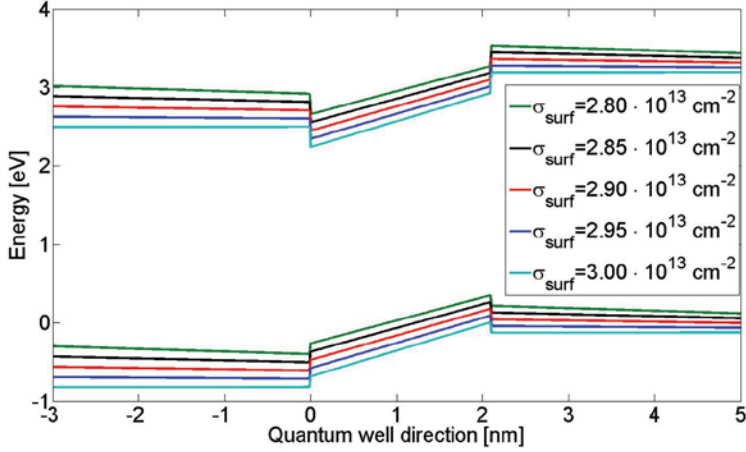


Figure C.0.3. The effective valence and conduction band potential at various surface charge densities.

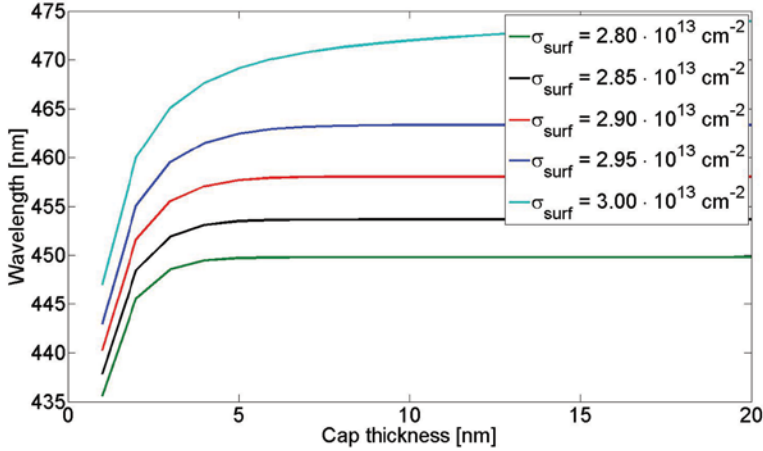


Figure C.0.4. Emission wavelength at various surface charge densities.

In Figure C.0.1 we plot the various electron wavefunctions as a function of the surface charge density. Similar plots are shown in Figure C.0.2, Figure C.0.3 and Figure C.0.4 for the electrical dipole moment, band-gap energy levels and emission wavelength, respectively. All these figures present results for the sample with 6 nm cap thickness.

0. Abbreviations

Abbreviations

AFM - atomic force microscopy

Al₂O₃ - aluminum oxide

ALD - atomic layer deposition

AlGaN - aluminum gallium nitride

Ar - argon

BCl₃ - boron trichloride

BHF - buffered hydrogen fluoride

CH₄ - methane

CHF₃ - freon

CH₃ - methyl

Cl₂ - chlorine

DI - deionized water

FWHM - full width half maximum

GaN - gallium nitride

H₂ - hydrogen

HCl - hydrochloric acid

HF - hydrogen fluoride

ICP – inductively coupled plasma

InGaN - indium gallium nitride

InN - indium nitride

IR - infrared

IRF - instrument response function

ITO - indium tin oxide

LED – light-emitting diode

MOCVD - metal organic chemical vapor deposition

0. Abbreviations

NCs - nanocrystals

O₂ - oxygen

PECVD – plasma enhanced chemical vapor deposition

PL - photoluminescence

QD – quantum dot

QW - quantum well

RF - radio-frequency

RIE – reactive ion etching

sccm - standard cubic centimeter per minute

SEM - scanning electron microscopy

SiO₂ - silicon dioxide

SSL - solid-state lighting

TCSPC – time-correlated single photon counting

TEM - transmission electron microscopy

TRPL - time-resolved photoluminescence

UV - ultraviolet

Bibliography

- [1] K. Davitt, Y.-K. Song, W. Patterson Iii, A. Nurmikko, M. Gherasimova, J. Han, Y.-L. Pan, and R. Chang, “290 and 340 nm UV LED arrays for fluorescence detection from single airborne particles.,” *Optics express*, vol. 13, no. 23, pp. 9548–55, Nov. 2005.
- [2] T. Nishida, H. Saito, and N. Kobayashi, “Efficient and high-power AlGaIn-based ultraviolet light-emitting diode grown on bulk GaN,” *Applied Physics Letters*, vol. 79, no. 6, p. 711, 2001.
- [3] H. P. Xin, R. J. Welty, and C. W. Tu, “GaIn_{0.011}P_{0.989} red light-emitting diodes directly grown on GaP substrates,” *Applied Physics Letters*, vol. 77, no. 13, p. 1946, 2000.
- [4] M. R. Krames, M. Ochiai-Holcomb, G. E. Höfler, C. Carter-Coman, E. I. Chen, I.-H. Tan, P. Grillot, N. F. Gardner, H. C. Chui, J.-W. Huang, S. a. Stockman, F. a. Kish, M. G. Craford, T. S. Tan, C. P. Kocot, M. Hueschen, J. Posselt, B. Loh, G. Sasser, and D. Collins, “High-power truncated-inverted-pyramid (Al_xGa_{1-x})_{0.5}In_{0.5}P/GaP light-emitting diodes exhibiting >50% external quantum efficiency,” *Applied Physics Letters*, vol. 75, no. 16, p. 2365, 1999.
- [5] F. a. Kish, F. M. Steranka, D. C. DeFever, D. a. Vanderwater, K. G. Park, C. P. Kuo, T. D. Osentowski, M. J. Peanasky, J. G. Yu, R. M. Fletcher, D. a. Steigerwald, M. G. Craford, and V. M. Robbins, “Very high-efficiency semiconductor wafer-bonded transparent-substrate (Al_xGa_{1-x})_{0.5}In_{0.5}P/GaP light-emitting diodes,” *Applied Physics Letters*, vol. 64, no. 21, p. 2839, 1994.
- [6] W. Gaynor, S. Hofmann, M. G. Christoforo, C. Sachse, S. Mehra, A. Salleo, M. D. McGehee, M. C. Gather, B. Lüssem, L. Müller-Meskamp, P. Peumans, and K. Leo, “Color in the Corners: ITO-Free White OLEDs with Angular Color Stability.,” *Advanced materials (Deerfield Beach, Fla.)*, pp. 1–8, May 2013.
- [7] Y. Narukawa, I. Niki, K. Izuno, M. Yamada, Y. Murazaki, and T. Mukai, “Phosphor-Conversion White Light Emitting Diode Using

O. Bibliography

- InGaN Near-Ultraviolet Chip,” *Japanese Journal of Applied Physics*, vol. 41, no. Part 2, No. 4A, pp. L371–L373, Apr. 2002.
- [8] P. Yang, X. Yu, X. Xu, T. Jiang, H. Yu, D. Zhou, Z. Yang, Z. Song, and J. Qiu, “Single-phased $\text{CaAl}_2\text{Si}_2\text{O}_8:\text{Tm}^{3+}$, Dy^{3+} white-light phosphors under ultraviolet excitation,” *Journal of Solid State Chemistry*, vol. 202, pp. 143–148, Jun. 2013.
- [9] W. Guo, M. Zhang, A. Banerjee, and P. Bhattacharya, “Catalyst-free InGaN/GaN nanowire light emitting diodes grown on (001) silicon by molecular beam epitaxy.,” *Nano letters*, vol. 10, no. 9, pp. 3355–9, Sep. 2010.
- [10] M. Achermann, M. a Petruska, D. D. Koleske, M. H. Crawford, and V. I. Klimov, “Nanocrystal-based light-emitting diodes utilizing high-efficiency nonradiative energy transfer for color conversion.,” *Nano letters*, vol. 6, no. 7, pp. 1396–1400, Jul. 2006.
- [11] G. Itskos, C. R. Belton, G. Heliotis, I. M. Watson, M. D. Dawson, R. Murray, and D. D. C. Bradley, “White light emission via cascade Förster energy transfer in (Ga, In)N quantum well/polymer blend hybrid structures.,” *Nanotechnology*, vol. 20, no. 27, p. 275207, Jul. 2009.
- [12] V. M. Agranovich, G. C. Rocca, and F. Bassani, “Efficient electronic energy transfer from a semiconductor quantum well to an organic material,” *Journal of Experimental and Theoretical Physics Letters*, vol. 66, no. 11, pp. 748–751, Dec. 1997.
- [13] C. R. Belton, G. Itskos, G. Heliotis, P. N. Stavrinou, P. G. Lagoudakis, J. Lupton, S. Pereira, E. Gu, C. Griffin, B. Guilhabert, I. M. Watson, a R. Mackintosh, R. a Pethrick, J. Feldmann, R. Murray, M. D. Dawson, and D. D. C. Bradley, “New light from hybrid inorganic–organic emitters,” *Journal of Physics D: Applied Physics*, vol. 41, no. 9, p. 094006, May 2008.
- [14] Š. Kos, M. Achermann, V. Klimov, and D. Smith, “Different regimes of Förster-type energy transfer between an epitaxial quantum well and a proximal monolayer of semiconductor nanocrystals,” *Physical Review B*, vol. 71, no. 20, p. 205309, May 2005.
- [15] M. Achermann, M. a Petruska, D. D. Koleske, M. H. Crawford, and V. I. Klimov, “Nanocrystal-based light-emitting diodes utilizing

O. Bibliography

- high-efficiency nonradiative energy transfer for color conversion.,” *Nano letters*, vol. 6, no. 7, pp. 1396–400, Jul. 2006.
- [16] H. J. Round, “A Note on Carborundum,” *Electrical World*, vol. 49, p. 309, 1907.
- [17] E. F. Schubert, *Light-Emitting Diodes*, Second edi. Cambridge: Cambridge University Press, 2006.
- [18] C. Adachi, M. a. Baldo, M. E. Thompson, and S. R. Forrest, “Nearly 100% internal phosphorescence efficiency in an organic light-emitting device,” *Journal of Applied Physics*, vol. 90, no. 10, p. 5048, 2001.
- [19] S. Coe, W. Woo, and V. M. Bawendi, “Electroluminescence from single monolayers of nanocrystals in molecular organic devices,” *Nature*, vol. 420, no. December, pp. 3–6, 2002.
- [20] C. B. Soh, W. Liu, a M. Yong, S. J. Chua, S. Y. Chow, S. Tripathy, and R. J. N. Tan, “Phosphor-Free Apple-White LEDs with Embedded Indium-Rich Nanostructures Grown on Strain Relaxed Nano-epitaxy GaN.,” *Nanoscale research letters*, vol. 5, no. 11, pp. 1788–1794, Jan. 2010.
- [21] T. Miyoshi, S. Masui, T. Okada, T. Yanamoto, T. Kozaki, S. Nagahama, and T. Mukai, “510–515 nm InGaN-Based Green Laser Diodes on c -Plane GaN Substrate,” *Applied Physics Express*, vol. 2, p. 062201, May 2009.
- [22] Y. Enya, Y. Yoshizumi, T. Kyono, K. Akita, M. Ueno, M. Adachi, T. Sumitomo, S. Tokuyama, T. Ikegami, K. Katayama, and T. Nakamura, “531 nm Green Lasing of InGaN Based Laser Diodes on Semi-Polar {20 $\bar{2}$ 1} Free-Standing GaN Substrates,” *Applied Physics Express*, vol. 2, p. 082101, Jul. 2009.
- [23] M. T. Hardy, D. F. Feezell, S. P. DenBaars, and S. Nakamura, “Group III-nitride lasers: a materials perspective,” *Materials Today*, vol. 14, no. 9, pp. 408–415, Sep. 2011.
- [24] Y.-D. Lin, S. Yamamoto, C.-Y. Huang, C.-L. Hsiung, F. Wu, K. Fujito, H. Ohta, J. S. Speck, S. P. DenBaars, and S. Nakamura, “High Quality InGaN/AlGaN Multiple Quantum Wells for Semipolar

0. Bibliography

- InGaN Green Laser Diodes,” *Applied Physics Express*, vol. 3, no. 8, p. 082001, Jul. 2010.
- [25] “Energy consumption,” *How much energy can be saved with solid-state lighting? How much will these energy savings reduce CO2 emissions?* [Online]. Available: [Http://lighting.sandia.gov/XlightingoverviewFAQ.htm#much](http://lighting.sandia.gov/XlightingoverviewFAQ.htm#much).
- [26] “Energy efficiency requirements for light bulbs and other energy-using products on track for adoption.” [Online]. Available: http://europa.eu/rapid/press-release_IP-07-867_en.htm?locale=en.
- [27] E. F. Schubert, J. K. Kim, H. Luo, and J.-Q. Xi, “Solid-state lighting—a benevolent technology,” *Reports on Progress in Physics*, vol. 69, no. 12, pp. 3069–3099, Dec. 2006.
- [28] J. M. Phillips, M. E. Coltrin, M. H. Crawford, a. J. Fischer, M. R. Krames, R. Mueller-Mach, G. O. Mueller, Y. Ohno, L. E. S. Rohwer, J. a. Simmons, and J. Y. Tsao, “Research challenges to ultra-efficient inorganic solid-state lighting,” *Laser & Photonics Review*, vol. 1, no. 4, pp. 307–333, Dec. 2007.
- [29] M. R. Krames, O. B. Shchekin, R. Mueller-Mach, G. O. Mueller, L. Zhou, G. Harbers, and M. G. Craford, “Status and Future of High-Power Light-Emitting Diodes for Solid-State Lighting,” *Journal of Display Technology*, vol. 3, no. 2, pp. 160–175, Jun. 2007.
- [30] [Http://www.nichia.co.jp/en/product/led.html](http://www.nichia.co.jp/en/product/led.html),
“<http://www.nichia.co.jp/en/product/led.html>.”
- [31] H.-F. Xiang, S.-C. Yu, C.-M. Che, and P. T. Lai, “Efficient white and red light emission from GaN/tris-(8-hydroxyquinolato) aluminum/platinum(II) meso-tetrakis(pentafluorophenyl) porphyrin hybrid light-emitting diodes,” *Applied Physics Letters*, vol. 83, no. 8, p. 1518, 2003.
- [32] C. Wetzel, Y. Xia, T. Detchprohm, P. Li, and J. S. Nelson, “Junction temperature in light-emitting diodes assessed by different methods,” in *Light-Emitting Diodes: Research, Manufacturing, and Applications IX, 1*, 2005, vol. 5739, pp. 1–6.
- [33] G. Heliotis, G. Itskos, R. Murray, M. D. Dawson, I. M. Watson, and D. D. C. Bradley, “Hybrid Inorganic/Organic Semiconductor

O. Bibliography

- Heterostructures with Efficient Non-Radiative Energy Transfer,” *Advanced Materials*, vol. 18, no. 3, pp. 334–338, Feb. 2006.
- [34] S. Chanyawadee, P. G. Lagoudakis, R. T. Harley, M. D. B. Charlton, D. V Talapin, H. W. Huang, and C.-H. Lin, “Increased color-conversion efficiency in hybrid light-emitting diodes utilizing non-radiative energy transfer.,” *Advanced materials (Deerfield Beach, Fla.)*, vol. 22, no. 5, pp. 602–6, Feb. 2010.
- [35] Z. Energiewanderung and F. Von, “Zwischenmolekulare Energiewanderung und Fluoreszenz,” vol. 437, p. 55, 1948.
- [36] H. Sahoo, “Journal of Photochemistry and Photobiology C : Photochemistry Reviews Förster resonance energy transfer – A spectroscopic nanoruler : Principle and applications,” “*Journal of Photochemistry & Photobiology, C: Photochemistry Reviews*,” vol. 12, no. 1, pp. 20–30, 2011.
- [37] R. Yasuda, “Imaging spatiotemporal dynamics of neuronal signaling using fluorescence resonance energy transfer and fluorescence lifetime imaging microscopy.,” *Current opinion in neurobiology*, vol. 16, no. 5, pp. 551–61, Oct. 2006.
- [38] G. Heliotis, G. Itskos, R. Murray, M. D. Dawson, I. M. Watson, and D. D. C. Bradley, “Hybrid Inorganic/Organic Semiconductor Heterostructures with Efficient Non-Radiative Energy Transfer,” *Advanced Materials*, vol. 18, no. 3, pp. 334–338, Feb. 2006.
- [39] J. Hill, S. Heriot, O. Worsfold, T. Richardson, a. Fox, and D. Bradley, “Controlled Förster energy transfer in emissive polymer Langmuir-Blodgett structures,” *Physical Review B*, vol. 69, no. 4, pp. 1–4, Jan. 2004.
- [40] T. Sen, S. Sadhu, and A. Patra, “Surface energy transfer from rhodamine 6G to gold nanoparticles: A spectroscopic ruler,” *Applied Physics Letters*, vol. 91, no. 4, p. 043104, 2007.
- [41] M. Achermann, M. a Petruska, S. Kos, D. L. Smith, D. D. Koleske, and V. I. Klimov, “Energy-transfer pumping of semiconductor nanocrystals using an epitaxial quantum well.,” *Nature*, vol. 429, no. 6992, pp. 642–6, Jun. 2004.

O. Bibliography

- [42] R. H. Fairclough and C. R. Cantor, "The use of singlet-singlet energy transfer to study macromolecular assemblies," *Biochemistry*, vol. 15, pp. 347–379, 1976.
- [43] C. G. dos Remedios, M. Miki, and J. a Barden, "Fluorescence resonance energy transfer measurements of distances in actin and myosin. A critical evaluation.," *Journal of muscle research and cell motility*, vol. 8, no. 2, pp. 97–117, Apr. 1987.
- [44] P. Wu and L. Brand, "Resonance energy transfer - methods and applications..pdf," *Analytical Biochemistry*, no. 218, pp. 1–13, 1994.
- [45] Y. Gladush, C. Piermarocchi, and V. Agranovich, "Dynamics of excitons and free carriers in hybrid organic-inorganic quantum well structures," *Physical Review B*, vol. 84, no. 20, p. 205312, Nov. 2011.
- [46] V. I. Klimov, "Nanocrystal Quantum Dots," no. 28, pp. 214–220, 2003.
- [47] Y. Yin and A. Alivisatos, "Colloidal nanocrystal synthesis and the organic–inorganic interface," *Nature*, vol. 437, no. 7059, pp. 664–70, Sep. 2004.
- [48] I. Zns, C. Shell, Q. Dots, A. Narayanaswamy, L. F. F. A. Meijerink, and P. J. Van Der Zaag, "The Effect of Temperature and Dot Size on the Spectral Properties of Colloidal," vol. 3, no. 9, pp. 2539–2546, 2009.
- [49] "Nanocrystals," *Nanomaterials & nanofabrication laboratories*. [Online]. Available: <http://www.nn-labs.com/>.
- [50] N. Pradhan, D. Goorskey, J. Thessing, and X. Peng, "An alternative of CdSe nanocrystal emitters: pure and tunable impurity emissions in ZnSe nanocrystals.," *Journal of the American Chemical Society*, vol. 127, no. 50, pp. 17586–7, Dec. 2005.
- [51] R. Xie, D. Battaglia, and X. Peng, "Colloidal InP nanocrystals as efficient emitters covering blue to near-infrared.," *Journal of the American Chemical Society*, vol. 129, no. 50, pp. 15432–3, Dec. 2007.

O. Bibliography

- [52] B. L. Wehrenberg, C. Wang, and P. Guyot-Sionnest, "Interband and Intraband Optical Studies of PbSe Colloidal Quantum Dots," *The Journal of Physical Chemistry B*, vol. 106, no. 41, pp. 10634–10640, Oct. 2002.
- [53] C. de Mello Donegá, S. G. Hickey, S. F. Wuister, D. Vanmaekelbergh, and A. Meijerink, "Single-Step Synthesis to Control the Photoluminescence Quantum Yield and Size Dispersion of CdSe Nanocrystals," *The Journal of Physical Chemistry B*, vol. 107, no. 2, pp. 489–496, Jan. 2003.
- [54] B. MacEvoy, *Color temperature*. 2009.
- [55] and R. F. D. L. L. Smith, S. W. King, R. J. Nemanich, "Cleaning of GaN Surfaces.pdf," *Journal of Electronic Materials*, vol. 25, no. 5, pp. 805–810, 1996.
- [56] W. Kern, "The Evolution of Silicon Wafer Cleaning Technology," *Journal of The Electrochemical Society*, vol. 137, no. 6, p. 1887, 1990.
- [57] T. Ohmi, "Total Room Temperature Wet Cleaning for Si Substrate Surface," *Journal of The Electrochemical Society*, vol. 143, no. 9, p. 2957, 1996.
- [58] S. W. King, J. P. Barnak, M. D. Bremser, K. M. Tracy, C. Ronning, R. F. Davis, and R. J. Nemanich, "Cleaning of AlN and GaN surfaces," *Journal of Applied Physics*, vol. 84, no. 9, p. 5248, 1998.
- [59] I. Adesida, C. Youtsey, a. T. Ping, F. Khan, L. T. Romano, and G. Bulman, "Dry and Wet Etching for Group III – Nitrides," *MRS Proceedings*, vol. 537. p. G1.4, 10-Feb-1998.
- [60] J. Lee, H. Cho, and D. Hays, "Dry etching of GaN and related materials: comparison of techniques," *Selected Topics in ...*, vol. 4, no. 3, pp. 557–563, 1998.
- [61] F. a. Khan, L. Zhou, a. T. Ping, and I. Adesida, "Inductively coupled plasma reactive ion etching of Al[sub x]Ga[sub 1–x]N for application in laser facet formation," *Journal of Vacuum Science & Technology B: Microelectronics and Nanometer Structures*, vol. 17, no. 6, p. 2750, 1999.

O. Bibliography

- [62] "PHYSICAL CONSTANTS OF INORGANIC COMPOUNDS," in *CRC Handbook of Chemistry and Physics*, CRC, Boca Raton, FL, 1990.
- [63] C. B. Vartuli, J. D. MacKenzie, J. W. Lee, C. R. Abernathy, S. J. Pearton, and R. J. Shul, "Cl₂/Ar and CH₄/H₂/Ar dry etching of III–V nitrides," *Journal of Applied Physics*, vol. 80, no. 7, p. 3705, 1996.
- [64] J. Q. Liu, M. F. Zybur, Y. C. Pao, R. Westerman, and C. Constantine, "Dry etching process in InP Gunn device technology utilizing inductively coupled plasma (ICP) system," *Conference Proceedings. 1998 International Conference on Indium Phosphide and Related Materials (Cat. No.98CH36129)*, no. May, pp. 187–190, 1998.
- [65] J. Kaindl, S. Sotier, and G. Franz, "Dry Etching of III/V Semiconductors: Fine Tuning of Pattern Transfer and Process Control," *Journal of The Electrochemical Society*, vol. 142, no. 7, pp. 2418–2424, 1995.
- [66] F. Ren, "Reduction of sidewall roughness during dry etching of SiO₂," *Journal of Vacuum Science & Technology B: Microelectronics and Nanometer Structures*, vol. 10, no. 6, p. 2407, Nov. 1992.
- [67] S. Bouchoule, S. Boubanga-Tombet, L. Le Gratiet, M. Le Vassor d'Yerville, J. Torres, Y. Chen, and D. Coquillat, "Reactive ion etching of high optical quality GaN/sapphire photonic crystal slab using CH₄–H₂ chemistry," *Journal of Applied Physics*, vol. 101, no. 4, p. 043103, 2007.
- [68] J. Liu, G. L. Huppert, and H. H. Sawin, "Ion bombardment in rf plasmas," *Journal of Applied Physics*, vol. 68, no. 8, p. 3916, 1990.
- [69] D. L. Flamm, "Basic chemistry and mechanisms of plasma etching," *Journal of Vacuum Science & Technology B: Microelectronics and Nanometer Structures*, vol. 1, no. 1, p. 23, 1983.
- [70] C.-C. Yu, C.-F. Chu, J.-Y. Tsai, H. W. Huang, T.-H. Hsueh, C.-F. Lin, and S.-C. Wang, "Gallium Nitride Nanorods Fabricated by Inductively Coupled Plasma Reactive Ion Etching," *Japanese Journal of Applied Physics*, vol. 41, no. Part 2, No. 8B, pp. L910–L912, Aug. 2002.

0. Bibliography

- [71] J. K. Sheu, Y. K. Su, G. C. Chi, M. J. Jou, C. C. Liu, C. M. Chang, and W. C. Hung, "Inductively coupled plasma etching of GaN using Cl_2/Ar and Cl_2/N_2 gases," *Journal of Applied Physics*, vol. 85, no. 3, p. 1970, 1999.
- [72] R. J. Shul, G. B. McClellan, S. a. Casalnuovo, D. J. Rieger, S. J. Pearton, C. Constantine, C. Barratt, R. F. Karlicek, C. Tran, and M. Schurman, "Inductively coupled plasma etching of GaN," *Applied Physics Letters*, vol. 69, no. 8, p. 1119, 1996.
- [73] R. J. Shul, C. G. Willison, M. M. Bridges, J. Han, and S. M. Donovan, "Selective inductively coupled plasma etching of group-III nitrides in Cl_2 - and BCl_3 -based plasmas," pp. 1621–1626, 1998.
- [74] J.-M. Lee, K.-M. Chang, S.-W. Kim, C. Huh, I.-H. Lee, and S.-J. Park, "Dry etch damage in n-type GaN and its recovery by treatment with an N_2 plasma," *Journal of Applied Physics*, vol. 87, no. 11, p. 7667, 2000.
- [75] H. W. Jang and J.-L. Lee, "Effect of Cl_2 Plasma Treatment on Metal Contacts to n-Type and p-Type GaN," *Journal of The Electrochemical Society*, vol. 150, no. 9, p. G513, 2003.
- [76] X. a. Cao, H. Piao, S. F. LeBoeuf, J. Li, J. Y. Lin, and H. X. Jiang, "Effects of plasma treatment on the Ohmic characteristics of $\text{Ti}/\text{Al}/\text{Ti}/\text{Au}$ contacts to n-AlGaIn," *Applied Physics Letters*, vol. 89, no. 8, p. 082109, 2006.
- [77] X. a. Cao, S. J. Pearton, a. P. Zhang, G. T. Dang, F. Ren, R. J. Shul, L. Zhang, R. Hickman, and J. M. Van Hove, "Electrical effects of plasma damage in p-GaN," *Applied Physics Letters*, vol. 75, no. 17, p. 2569, 1999.
- [78] Y. Yang and X. a. Cao, "Removing plasma-induced sidewall damage in GaN-based light-emitting diodes by annealing and wet chemical treatments," *Journal of Vacuum Science & Technology B: Microelectronics and Nanometer Structures*, vol. 27, no. 6, p. 2337, 2009.
- [79] M. Boroditsky, I. Gontijo, M. Jackson, R. Vrijen, E. Yablonovitch, T. Krauss, C.-C. Cheng, a. Scherer, R. Bhat, and M. Krames, "Surface recombination measurements on III–V candidate materials for

O. Bibliography

- nanostructure light-emitting diodes,” *Journal of Applied Physics*, vol. 87, no. 7, p. 3497, 2000.
- [80] L. S. Mccarthy, P. Kozodoy, M. J. W. Rodwell, S. Member, S. P. Denbaars, and U. K. Mishra, “AlGaN / GaN Heterojunction Bipolar Transistor,” vol. 20, no. 6, pp. 1999–2001, 1999.
- [81] K.-P. Hsueh, Y.-M. Hsin, and J.-K. Sheu, “Low Schottky barrier to etched p-GaN using regrown AlInGaN and InGaN contact layer,” *Journal of Applied Physics*, vol. 99, no. 2, p. 026106, 2006.
- [82] J. S. Foresi and T. D. Moustakas, “Metal contacts to gallium nitride,” *Applied Physics Letters*, vol. 62, no. 22, p. 2859, 1993.
- [83] S. Miller and P. H. Holloway, “Ohmic contacts to n-type GaN,” *Journal of Electronic Materials*, vol. 25, no. 11, pp. 1709–1714, Nov. 1996.
- [84] Y. Koide, T. Maeda, T. Kawakami, S. Fujita, T. Uemura, N. Shibata, and M. Murakami, “Effects of annealing in an oxygen ambient on electrical properties of ohmic contacts to p-type GaN,” *Journal of Electronic Materials*, vol. 28, no. 3, pp. 341–346, Mar. 1999.
- [85] M.-L. Lee, J.-K. Sheu, and C. C. Hu, “Nonalloyed Cr/Au-based Ohmic contacts to n-GaN,” *Applied Physics Letters*, vol. 91, no. 18, p. 182106, 2007.
- [86] H. Gao, F. Yan, Y. Zhang, J. Li, Y. Zeng, G. Wang, and F. Yang, “Improvement of GaN-based light emitting diodes performance grown on sapphire substrates patterned by wet etching,” *Proceedings of SPIE*, vol. 6841, pp. 684107–684107–6, 2007.
- [87] J. Hwang, G. Yang, C. Lin, and S. Chang, “Nonalloyed Ti/indium tin oxide and Ti ohmic contacts to n-type GaN using plasma pre-treatment,” *Solid-State Electronics*, vol. 50, no. 2, pp. 297–299, Feb. 2006.
- [88] X. Yi, L. Wang, J. Fan, X. Wang, H. Yang, Y. Li, L. Wang, G. Wang, and F. Yang, “Research and fabrication of high power LEDs with transparent electrodes,” *Proceedings of SPIE*, vol. 6841, p. 68410B–68410B–5, 2007.

O. Bibliography

- [89] J. K. Sheu, I.-H. Hung, W. C. Lai, S. C. Shei, and M. L. Lee, "Enhancement in output power of blue gallium nitride-based light-emitting diodes with omnidirectional metal reflector under electrode pads," *Applied Physics Letters*, vol. 93, no. 10, p. 103507, 2008.
- [90] J.-S. Jang, T.-Y. Seong, and S.-R. Jeon, "Electronic Transport Mechanism for Nonalloyed Ti-Based Ohmic Contacts to Strained n-AlGaIn/GaN Heterostructure," *Electrochemical and Solid-State Letters*, vol. 10, no. 4, p. H120, 2007.
- [91] A. Motayed, M. Jah, A. Sharma, W. T. Anderson, C. W. Litton, and S. N. Mohammad, "Two-step surface treatment technique: Realization of nonalloyed low-resistance Ti/Al/Ti/Au ohmic contact to n-GaN," *Journal of Vacuum Science & Technology B: Microelectronics and Nanometer Structures*, vol. 22, no. 2, p. 663, 2004.
- [92] M. W. Cole, D. W. Eckart, W. Y. Han, R. L. Pfeffer, and T. Monahan, "Thermal stability of W ohmic contacts to n-type GaN Thermal stability of W ohmic contacts to n -type GaN," vol. 278, 1996.
- [93] L. F. Lester, J. M. Brown, J. C. Ramer, and L. Zhang, "Nonalloyed Ti/Al Ohmic contacts to n-type GaN using hightemperature premetallization anneal," vol. 2737, pp. 1–4, 1996.
- [94] B. Goldenberg, J. D. Zook, and R. J. Ulmer, "Ultraviolet and violet light-emitting GaN diodes grown by low-pressure metalorganic chemical vapor deposition," *Applied Physics Letters*, vol. 62, no. 4, p. 381, 1993.
- [95] D. Ingerly, Y. Chang, and Y. Chen, "NiIn as an ohmic contact to p-GaN," *MRS Proceedings*, 1998.
- [96] M.-S. Oh, J.-S. Jang, S.-J. Park, and T.-Y. Seong, "Electrical properties of nonalloyed Ni/Au ohmic contacts to laser-irradiated p-GaN," *Journal of Materials Science: Materials in Electronics*, vol. 17, no. 10, pp. 831–834, Oct. 2006.
- [97] F. G. Kalaitzakis, N. T. Pelekanos, P. Prystawko, M. Leszczynski, and G. Konstantinidis, "Low resistance as-deposited Cr/Au contacts on p-type GaN," *Applied Physics Letters*, vol. 91, no. 26, p. 261103, 2007.

O. Bibliography

- [98] K. Chen, *Recombination Dynamics in Silicon-doped Aluminum Gallium Nitride and Ultraviolet Light-emitting Diodes Grown on Sapphire and Bulk Aluminum Nitride*. 2008.
- [99] “RPM2000 Rapid Photoluminescence Mapper - Room Temperature PL Mapping System from Nanometrics.” [Online]. Available: <http://www.azonano.com/article.aspx?ArticleID=2308>. [Accessed: 16-Jul-2013].
- [100] J. Yguerabide, “Nanosecond fluorescence spectroscopy of macromolecules.,” *Methods in enzymology*, vol. 26. pp. 498–578, Jan-1972.
- [101] F. S. W. Meiling, “Nanosecond pulse techniques,” *Proceedings of the IEEE*, vol. 80, no. 6. Akademie-Verlag, Berlin, Jun-1963.
- [102] M. S. Minsky, S. Watanabe, and N. Yamada, “Radiative and nonradiative lifetimes in GaInN / GaN multiquantum wells Radiative and nonradiative lifetimes in GaInN/GaN multiquantum wells,” *Journal of Applied Physics*, vol. 91, no. May, pp. 5176–5181, 2002.
- [103] S.-W. Feng, Y.-C. Cheng, Y.-Y. Chung, C. C. Yang, Y.-S. Lin, C. Hsu, K.-J. Ma, and J.-I. Chyi, “Impact of localized states on the recombination dynamics in InGaN/GaN quantum well structures,” *Journal of Applied Physics*, vol. 92, no. 8, p. 4441, 2002.
- [104] P. Riblet, H. Hirayama, A. Kinoshita, A. Hirata, T. Sugano, and Y. Aoyagi, “Determination of photoluminescence mechanism in InGaN quantum wells,” *Applied Physics Letters*, vol. 75, no. 15, p. 2241, 1999.
- [105] Z. Jiang and D. F. Kelley, “Effects of Inhomogeneous Shell Thickness in the Charge Transfer Dynamics of ZnTe/CdSe Nanocrystals,” 2012.
- [106] L. Li and P. Reiss, “One-pot Synthesis of Highly Luminescent InP / ZnS Nanocrystals without,” pp. 11588–11589, 2008.
- [107] S. S. Lo, Y. Khan, M. Jones, and G. D. Scholes, “Temperature and solvent dependence of CdSe / CdTe heterostructure nanorod spectra Temperature and solvent dependence of CdSe / CdTe heterostructure nanorod spectra,” vol. 084714, 2009.

O. Bibliography

- [108] T. O. Connor, M. S. Panov, A. Mereshchenko, A. N. Tarnovsky, R. Lorek, D. Perera, G. Diederich, S. Lambright, P. Moroz, and M. Zamkov, "The Effect of the Charge-Separating Interface on Exciton Dynamics in Photocatalytic Colloidal Heteronanocrystals," no. 9, pp. 8156–8165, 2012.
- [109] K. E. Knowles, E. A. McArthur, and E. A. Weiss, "ARTICLE A Multi-Timescale Map of Radiative and Nonradiative Decay Pathways for Excitons in CdSe Quantum Dots," no. 3, pp. 2026–2035, 2011.
- [110] M. Jones and G. D. Scholes, "On the use of time-resolved photoluminescence as a probe of nanocrystal photoexcitation dynamics," *Journal of Materials Chemistry*, vol. 20, no. 18, p. 3533, 2010.
- [111] a. van Driel, I. Nikolaev, P. Vergeer, P. Lodahl, D. Vanmaekelbergh, and W. Vos, "Statistical analysis of time-resolved emission from ensembles of semiconductor quantum dots: Interpretation of exponential decay models," *Physical Review B*, vol. 75, no. 3, p. 035329, Jan. 2007.
- [112] J. Tang and R. a Marcus, "Mechanisms of fluorescence blinking in semiconductor nanocrystal quantum dots.," *The Journal of chemical physics*, vol. 123, no. 5, p. 054704, Aug. 2005.
- [113] B. R. Fisher, N. E. Stott, and M. G. Bawendi, "Emission Intensity Dependence and Single-Exponential Behavior In Single Colloidal Quantum Dot Fluorescence Lifetimes," vol. 11, pp. 143–148, 2004.
- [114] J. J. H. Pijpers, E. Hendry, M. T. W. Milder, R. Fanciulli, J. Savolainen, J. L. Herek, D. Vanmaekelbergh, S. Ruhman, D. Mocatta, D. Oron, a. Aharoni, U. Banin, and M. Bonn, "Carrier Multiplication and Its Reduction by Photodoping in Colloidal InAs Quantum Dots," *Journal of Physical Chemistry C*, vol. 111, no. 11, pp. 4146–4152, Mar. 2007.
- [115] O. I. Mic, H. M. Cheong, H. Fu, A. Zunger, J. R. Sprague, A. Mascarenhas, and A. J. Nozik, "Size-Dependent Spectroscopy of InP Quantum Dots," vol. 5647, no. 97, pp. 4904–4912, 1997.
- [116] R. Shirazi, O. Kopylov, a. Kovacs, and B. E. Kardynał, "Temperature dependent recombination dynamics in InP/ZnS colloidal

O. Bibliography

- nanocrystals,” *Applied Physics Letters*, vol. 101, no. 9, p. 091910, 2012.
- [117] T. Takeuchi, S. Sota, and M. Katsuragawa, “Quantum-confined Stark effect due to piezoelectric fields in GaInN strained quantum wells,” *Jpn. J. Appl. ...*, 1997.
- [118] S. Chichibu, T. Azuhata, T. Sota, and S. Nakamura, “Luminescences from localized states in InGaN epilayers,” *Applied Physics Letters*, vol. 70, no. 21, p. 2822, 1997.
- [119] M.-Y. Ryu, P. W. Yu, E. Shin, J. I. Lee, S. K. Yu, E. Oh, O. H. Nam, C. S. Sone, and Y. J. Park, “Effects of Si-doping in the barriers on the recombination dynamics in In_{0.15}Ga_{0.85}N/In_{0.015}Ga_{0.985}N quantum wells,” *Journal of Applied Physics*, vol. 89, no. 1, p. 634, 2001.
- [120] M. Pophristic, F. H. Long, C. Tran, I. T. Ferguson, and R. F. Karlicek, “Time-resolved photoluminescence measurements of InGaN light-emitting diodes,” *Applied Physics Letters*, vol. 73, no. 24, p. 3550, 1998.
- [121] G. Franssen, S. Grzanka, R. Czernecki, T. Suski, L. Marona, T. Riemann, J. Christen, H. Teisseyre, P. Valvin, P. Lefebvre, P. Perlin, M. Leszczyński, and I. Grzegory, “Efficient radiative recombination and potential profile fluctuations in low-dislocation InGaN/GaN multiple quantum wells on bulk GaN substrates,” *Journal of Applied Physics*, vol. 97, no. 10, p. 103507, 2005.
- [122] X. Chen, B. Henderson, and K. P. O'Donnell, “Luminescence decay in disordered low-dimensional semiconductors,” *Applied Physics Letters*, vol. 60, no. 21, p. 2672, 1992.
- [123] M.-Y. Ryu, P. W. Yu, E. Oh, C. Sone, O. Nam, and Y. Park, “Optical properties and recombination dynamics of InGaN/GaN multiple quantum wells with Si-doped barriers,” *Solid State Communications*, vol. 118, no. 11, pp. 547–551, Jun-2001.
- [124] M. Smith, J. Y. Lin, H. X. Jiang, a. Salvador, a. Botchkarev, W. Kim, and H. Morkoc, “Optical transitions in GaN/Al_xGa_{1-x}N multiple quantum wells grown by molecular beam epitaxy,” *Applied Physics Letters*, vol. 69, no. 17, p. 2453, 1996.

O. Bibliography

- [125] K. C. Zeng, J. Y. Lin, H. X. Jiang, a. Salvador, G. Popovici, H. Tang, W. Kim, and H. Morkoç, "Effects of well thickness and Si doping on the optical properties of GaN/AlGa_N multiple quantum wells," *Applied Physics Letters*, vol. 71, no. 10, p. 1368, 1997.
- [126] B. Gil, P. Lefebvre, J. Allègre, H. Mathieu, N. Grandjean, M. Leroux, J. Massies, P. Bigenwald, and P. Christol, "Observation of long-lived oblique excitons in GaN-AlGa_N multiple quantum wells," *Physical Review B*, vol. 59, no. 15, pp. 10246–10250, Apr. 1999.
- [127] L.-W. Jang, D.-W. Jeon, M. Kim, J.-W. Jeon, A. Y. Polyakov, J.-W. Ju, S.-J. Lee, J.-H. Baek, J.-K. Yang, and I.-H. Lee, "Investigation of Optical and Structural Stability of Localized Surface Plasmon Mediated Light-Emitting Diodes by Ag and Ag/SiO₂ Nanoparticles," *Advanced Functional Materials*, vol. 22, no. 13, pp. 2728–2734, Jul. 2012.
- [128] H. V. Demir, S. Nizamoglu, T. Erdem, E. Mutlugun, N. Gaponik, and A. Eychmüller, "Quantum dot integrated LEDs using photonic and excitonic color conversion," *Nano Today*, vol. 6, no. 6, pp. 632–647, Dec. 2011.
- [129] T. D. Moustakas and M. Misra, "Origin of the high photoconductive gain in AlGa_N films," in *In SPIE'07: Optoelectronic Devices: Physics, Fabrication, and Application IV. SPIE Conference: Optics & Photonics*, 2007, vol. 6766, p. 67660C–67660C–10.
- [130] S. Dhesi, C. Stagaescu, K. Smith, D. Doppalapudi, R. Singh, and T. Moustakas, "Surface and bulk electronic structure of thin-film wurtzite GaN," *Physical Review B*, vol. 56, no. 16, pp. 10271–10275, Oct. 1997.
- [131] V. Agranovich, H. Benisty, and C. Weisbuch, "Organic and inorganic quantum wells in a microcavity: Frenkel-Wannier-Mott excitons hybridization and energy transformation," *Solid state communications*, vol. 102, no. 8, pp. 631–636, 1997.
- [132] A. Othonos, G. Itskos, D. D. C. Bradley, M. D. Dawson, and I. M. Watson, "Influence of surface-related states on the carrier dynamics in (Ga,In)N/GaN single quantum wells," *Applied Physics Letters*, vol. 94, no. 20, p. 203102, 2009.

O. Bibliography

- [133] L. T. Tan, R. W. Martin, K. P. O'Donnell, and I. M. Watson, "Photoluminescence and phonon satellites of single InGaN/GaN quantum wells with varying GaN cap thickness," *Applied Physics Letters*, vol. 89, no. 10, p. 101910, 2006.
- [134] S. T. Pendlebury, P. J. Parbrook, D. J. Mowbray, D. a. Wood, and K. B. Lee, "InGaN/GaN quantum wells with low growth temperature GaN cap layers," *Journal of Crystal Growth*, vol. 307, no. 2, pp. 363–366, Sep. 2007.
- [135] O. Svensk, S. Suihkonen, S. Sintonen, O. Kopylov, R. Shirazi, H. Lipsanen, M. Sopanen, and B. E. Kardynal, "MOCVD growth and characterization of near-surface InGaN/GaN single quantum wells for non-radiative coupling of optical excitations," *Physica Status Solidi (C)*, vol. 9, no. 7, pp. 1667–1669, Jul. 2012.
- [136] R. Pecharroman-Gallego, P. R. Edwards, R. W. Martin, and I. M. Watson, "Investigations of phonon sidebands in InGaN / GaN multi-quantum well luminescence," *Materials Science and Engineering: B*, vol. 93, pp. 94–97, 2002.
- [137] L. P. I. Brener, M. Olszakier, E. Cohen, Arza Ron, "Particle localization and phonon sidebands in GaAs/Al_xGa_{1-x}As multiple quantum wells," vol. 46, no. 12, pp. 7927–7930, 1992.
- [138] J. Hopfield, "A theory of edge-emission phenomena in CdS, ZnS and ZnO," *Journal of Physics and Chemistry of Solids*, vol. 10, pp. 110–119, 1959.
- [139] K. L. Teo, J. S. Colton, P. Y. Yu, E. R. Weber, M. F. Li, W. Liu, K. Uchida, H. Tokunaga, N. Akutsu, and K. Matsumoto, "An analysis of temperature dependent photoluminescence line shapes in InGaN," *Applied Physics Letters*, vol. 73, no. 12, p. 1697, 1998.
- [140] P. G. Eliseev, P. Perlin, J. Lee, and M. Osiński, "'Blue' temperature-induced shift and band-tail emission in InGaN-based light sources," *Applied Physics Letters*, vol. 71, no. 5, p. 569, 1997.
- [141] R. Pecharromán-Gallego, R. W. Martin, and I. M. Watson, "Investigation of the unusual temperature dependence of InGaN/GaN quantum well photoluminescence over a range of emission energies," *Journal of Physics D: Applied Physics*, vol. 37, no. 21, pp. 2954–2961, Nov. 2004.

O. Bibliography

- [142] C. Adelmann, J. Simon, G. Feuillet, N. T. Pelekanos, B. Daudin, and G. Fishman, "Self-assembled InGaN quantum dots grown by molecular-beam epitaxy," *Applied Physics Letters*, vol. 76, no. 12, p. 1570, 2000.
- [143] Y. Xia, W. Hou, L. Zhao, M. Zhu, T. Detchprohm, and C. Wetzel, "Boosting Green GaInN/GaN Light-Emitting Diode Performance by a GaInN Underlying Layer," *IEEE Transactions on Electron Devices*, vol. 57, no. 10, pp. 2639–2643, Oct. 2010.
- [144] S. Chanyawadee, P. Lagoudakis, R. Harley, D. Lidzey, and M. Henini, "Nonradiative exciton energy transfer in hybrid organic-inorganic heterostructures," *Physical Review B*, vol. 77, no. 19, p. 193402, May 2008.
- [145] D. Basko, G. C. La Rocca, F. Bassani, and V. M. Agranovich, "Forster energy transfer from a semiconductor quantum well to an organic material overlayer," vol. 362, pp. 353–362, 1999.
- [146] K.-J. Byeon, E.-J. Hong, H. Park, K.-M. Yoon, H. D. Song, J. W. Lee, S.-K. Kim, H. K. Cho, H. K. Kwon, and H. Lee, "Two inch large area patterning on a vertical light-emitting diode by nano-imprinting technology," *Semiconductor Science and Technology*, vol. 25, no. 3, p. 035008, Mar. 2010.
- [147] M. Achermann, M. a Petruska, S. Kos, D. L. Smith, D. D. Koleske, and V. I. Klimov, "Energy-transfer pumping of semiconductor nanocrystals using an epitaxial quantum well.," *Nature*, vol. 429, no. 6992, pp. 642–6, Jun. 2004.
- [148] V. M. Agranovich, V. I. Rupasov, and L. Silvestri, "Hybrid resonant organic-inorganic nanostructures for novel light emitting devices and solar cells," *Physica Status Solidi (C)*, vol. 7, no. 6, pp. 1684–1687, Mar. 2010.
- [149] M. Rangus, "Control of the Crystallization Process and Structure Dimensionality of Mg – Benzene – 1,3,5-Tricarboxylates by Tuning Solvent Composition," pp. 1–10, 2013.
- [150] I. Vurgaftman and J. R. Meyer, "Band parameters for nitrogen-containing semiconductors," *Journal of Applied Physics*, vol. 94, no. 6, p. 3675, 2003.

0. Bibliography

- [151] and H. W. O. Madelung, M. Schultz, *Landolt-Börnstein, Numerical Data and Functional Relationships in Science and Technology*, vol. 46, no. 2. New series, 1982.
- [152] H. Lu, W. J. Schaff, L. F. Eastman, and C. E. Stutz, “Surface charge accumulation of InN films grown by molecular-beam epitaxy,” *Applied Physics Letters*, vol. 82, no. 11, p. 1736, 2003.